Diss. ETH No. 20450

Electronic properties of confined systems in single and bilayer graphene

A dissertation submitted to
ETH Zurich

for the degree of
Doctor of Sciences

presented by

Susanne Dröscher

M.Sc. KTH Stockholm
born April 25, 1984
citizen of Germany

accepted on the recommendation of:

Prof. Dr. Klaus Ensslin, examiner
Prof. Dr. Adrian Bachtold, co-examiner
Prof. Dr. Thomas Ihn, co-examiner

May 2012

Abstract

In this thesis, we present transport experiments on both single and bilayer graphene devices at cryogenic temperatures. Charge transport is strongly influenced by the system dimensions and we present different methods to confine carriers laterally.

Single and bilayer graphene exhibit a gapless energy spectrum, meaning that the transition from hole-like to electron-like transport is continuous and a finite conductivity is maintained at all energies. In bilayer graphene, however, the degeneracy of the valence band and the conduction band can be lifted by a potential difference between the two layers. We demonstrate, that a band gap is induced in an unpatterned double gated bilayer graphene flake, if a perpendicular electric field is applied. Thermal activation measurements yield an upper boundary of $E_{\mathrm{gap}} \approx 4$ meV for the size of the opened energy gap.

A deeper understanding of the single layer transport characteristics is gained by measurements of the quantum capacitance. This quantity is directly related to the density of states, which determines the electronic properties of a system. In contrast to theoretical predictions, we find that the density of states remains finite even at zero Fermi energy.

Quasi one-dimensional channels of single and bilayer graphene are investigated in a next step. Transport is dominated by a chain of quantum dots forming spontaneously due to disorder. Consequently the conductance is suppressed in a regime governed by Coulomb blockade. For single layer devices we show that between conductance resonances in this transport gap, cotunneling transport at the lowest temperatures turns into activated transport at higher temperatures.

As a further confined system, an etched bilayer grahene quantum dot is studied. With an additional top gate finger the island can be tuned independently from the reservoirs. Coulomb blockade resonances are observed in this system and their evolution is studied in an electric field as well as in a magnetic field. Moreover, we demonstrate first experiments with a pulsed gate, evidencing the feasibility of high frequency experiments on graphene devices.

Finally, an alternative approach for charge carrier confinement in bilayer graphene is presented. Since a band gap can be opened in this material, insulating regions can be defined below top gates. We show, that carriers are indeed directed through a narrow opening between gates and discuss possible transport mechanisms.

Zusammenfassung

In der vorliegenden Arbeit präsentieren wir Tieftemperaturexperimente, die den Ladungstransport in ein- und zweilagigem Graphen untersuchen. Allgemein werden die Transporteigenschaften eines Systems stark von dessen Dimensionen beeinflusst und wir zeigen verschiedene Möglichkeiten auf, diese für Ladungsträger zu reduzieren.

Sowohl einlagiges als auch zweilagiges Graphen besitzt keine Bandlücke und somit ist der Übergang von Löcher- zu Elektronentransport kontinuierlich. Ausserdem verbleibt die Leitfähigkeit für jede beliebige Energie bei endlichen Werten. In zweilagigem Graphen kann die Entartung des Valenz- und des Leitungsbandes jedoch durch eine Potentialdifferenz zwischen den beiden Lagen aufgehoben werden. Wir zeigen anhand eines unstrukturierten, zweilagigen Graphenflakes, das mit einem Top- und einem Bottomgate abgestimmt werden kann, dass ein senkrechtes elektrisches Feld eine Bandlücke erzeugt. Als Obergrenze für die Grösse dieser Bandlücke finden wir mittels Messungen der thermischen Aktivierung den Wert $E_{\mathrm{gap}} \approx 4$ meV.

Durch Messungen der Quantenkapazität gewinnen wir ein besseres Verständnis der Transporteigenschaften von einlagigem Graphen. Diese Grösse hängt direkt mit der Zustandsdichte zusammen, welche wiederum die elektrischen Eigenschaften eines Systems bestimmt. Im Gegensatz zu theoretischen Vorhersagen finden wir, dass die Zustandsdichten selbst bei Fermienergie gleich null, endliche Werte einnimmt.

Im nächsten Schritt untersuchen wir quasi-eindimensionale Kanäle in ein- und zweilagigem Graphen. In diesen wird der Transport wird durch eine Kette von Quantenpunkten dominiert, die sich aufgrund von Unordnung formen. Infolgedessen wird der Leitwert in diesem Regime, das sich durch Coulombblockade auszeichnet, unterdrückt. Für den Leitwert zwischen Coulombresonanzen zeigen wir anhand von einlagigem Graphen, dass Cotunnelprozesse bei tiefen Temperaturen von aktiviertem Transport bei höheren Temperaturen abgelöst werden.

In einem geätzten Quantenpunkt aus zweilagigem Graphen werden die Dimensionen weiter reduziert. Dank eines zusätzlichen Topgatefingers kann die Insel unabhängig von den Reservoiren abgestimmt werden. In diesem System sehen wir Coulombresonanzen und untersuchen deren Verhalten sowohl im elektrischen Feld als auch im Magnetfeld. Zudem zeigen wir erste Experimente mit gepulsten Gates, mit denen wir die Möglichkeit von Hochfrequenzexperimenten an Graphenproben

belegen.

Schliesslich präsentieren wir eine Alternative zu geätzten Strukturen, um Ladungsträger in zweilagigem Graphen lateral einzuschränken. Da in diesem Material eine Bandlücke geöffnet werden kann, können isolierende Flächen mittels Topgates definiert werden. Wir demonstrieren, dass Ladungsträger tatsächlich durch eine schmale Öffnung zwischen zwei Gates geleitet werden.

Contents

Lists of symbols

physical constants	explanation
-e<0	electron charge
m_{e}	electron mass
ϵ	dielectric permittivity
ϵ_0	vacuum dielectric constant
$h = 2\pi\hbar$	Planck's constant
k_{B}	Boltzmann constant

Abbreviation	Explanation
2DEG	two-dimensional electron gas
AC	alternating current
AFM	atomic force microscope
BN	hexagonal boron nitride
CB	Coulomb blockade
CNP	charge neutrality point
DC	direct current
DOS	density of states
EBL	electron beam lithography
FWHM	full width at half maximum
LL	Landau level
QD	quantum dot
QHE	quantum Hall effect
QPC	quantum point contact
RIE	reactive ion etching
SdH	Shubnikov-de Haas
SET	single electron transistor
SP	oxidation set point
UCF	universal conductance fluctuations
WR	write rate

Symbol	Explanation
L,W	system size (length, width)
B	magnetic field
E	electric field
D	displacement field
C_q	quantum capacitance
E_a	activation energy
E_c	charging energy
E_gap	energy gap
E_F	Fermi energy
α_G	gate lever arm
Δ_s	spin degenerate single particle level spacing
Q	charge
I	current
V	voltage
G	conductance
R	resistance
σ	conductivity
$\mathcal{D}$	density of states
Γ	tunneling coupling
v_F	Fermi velocity
k_F	Fermi wavenumber
λ_F	Fermi wavelength
μ	charge carrier mobility
n	charge carrier density
ν	filling factor
l_B	magnetic length
l_mfp	mean free path
ξ	localization length
d_opt	optimum hopping distance
T	temperature

Chapter 1

Introduction

1.1 Graphene

A precise definition of the term *graphene* was first introduced by H. P. Boehm in 1986 [1, 2]. He had observed very thin graphitic films already 30 years earlier [3], obtained by the reduction of a graphite-oxide suspension in adsorption measurements. Theoretically, graphene had been studied even before these experiments by P. Wallace [4], when he was exploring the band theory of graphite and started his considerations with a single sheet of graphite. Only in 2004, individual graphene layers could first be deposited onto a substrate by K. Novoselov and A. Geim [5], who received the Nobel prize in 2010 for their achievements regarding graphene.

In such a layer, carbon atoms are arranged in a two-dimensional hexagonal pattern connected to each other by covalent bonds within the plane. These strong interconnections make graphene one of the strongest materials available [6] that at the same time is highly flexible since the monoatomic layer can withstand very high strain. Its outstanding mechanical properties lead to large interest in the field of mechanical engineering.

Additional characteristics are the large surface to bulk ratio and the low optical absorption of graphene. Due to its versatile properties, a large number of applications is suggested ranging from reinforcement over DNA sensing to hydrogen storage.

1.2 Graphene electronics

Novoselov et al. were the first to electrically contact an isolated single graphene sheet. In measurements of the quantum Hall effect they could verify that indeed a single layer of graphene had been isolated [5]. Since then, graphene has been acclaimed for being a revolutionary material for electronic devices. Among the special properties, several meet the requirements of the present semiconductor technology. Monolayer graphene provides good accessibility for patterning and contacting, since all atoms are exposed at the surface. Lying only loosely on a substrate it has a

remarkable stability even when shaped into nanoscale structures [7, 8]. Additionally, the semiconductor industry is thrilled by the sub-nanometer thickness of this mono-atomic layer. The channels of current silicon field effect transistors could be thinned by a factor of one hundred if being replaced by graphene [9]. Moreover, due to its unique band structure, charge carriers do not suffer from backscattering and exhibit room temperature mobilities ten times higher than in silicon.

Besides complementing standard technologies, graphene is of substantial interest for fundamental research. With its carriers being described by the Dirac equation, it differs from standard semiconductors. Hence, physical phenomena so far only predicted theoretically may be probed in this material system. The observed unconventional quantum Hall effect [10] is one example for the finger print of the relativistic character of charge carriers in graphene.

Additionally, graphene offers the possibility to examine properties of quasi-relativistic particles in reduced dimensions. This is an appealing new field of studies within solid state physics and triggered various research projects concerned with nanoscale structures.

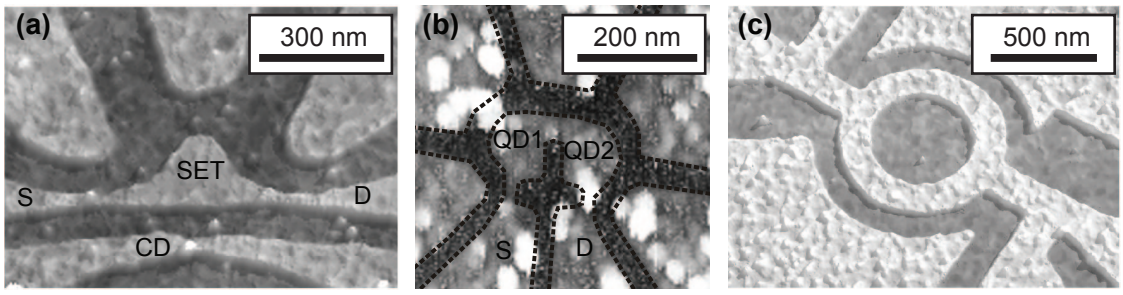

Figure 1.1: Atomic force micrographs of different graphene nanostructures: (a) Single electron transistor (SET) with a nearby charge detector (CD) [11]. Source (S) and drain (D) are connected via narrow constrictions to the SET. Several in-plane side-gates are used to tune the states on the island and inside the constrictions. (b) Double quantum dot with in-plane gates [12]. The series connection of source, left (QD1) and right quantum dot (QD2) and drain is implemented using narrow constrictions. (c) Aharonov-Bohm ring for quantum interference measurements [13].

1.3 Graphene nanostructures

Like in semiconductor devices, the charge carrier density in a graphene sheet can be tuned by gate electrodes utilizing the field effect. However, the absence of a band gap does not allow for a complete depletion of charge carriers inside the system and hence precludes electrostatic confinement. Instead, a continuous transition between hole- and electron-like transport takes place close to the charge neutrality point.

Experiments have shown however, that cutting graphene into narrow ribbons induces a suppression of electronic transport. This so-called transport gap was adopted as tunneling barriers in numerous different nano structures, where narrow constrictions are used to define the structures. Three exemplary devices are depicted in Fig. 1.1 including a single and a double quantum dot (Fig. 1.1 (a) and (b)) and a quantum interference device (Fig. 1.1 (c)). Resonances in the transport gap, which originate from disorder fluctuations in the device, prevent a monotonous tuning of the barrier thickness, however.

On the other hand, double gated bilayer graphene with low disorder may enable charge carrier confinement by electrostatics, since a band gap can be induced in this material [14]. Nanostructures may then exhibit tunability comparable to conventional semiconductor devices.

1.4 About this work

In the course of this work graphene devices exerting charge carrier confinement in one, two or three spacial dimensions will be introduced. Whereas several experiments were performed to gain understanding about the electronic transport properties of single layer graphene, the main focus lies on the investigation of the characteristics exhibited by bilayer graphene devices.

After the introduction in the present chapter, *chapter 2* recapitulates the band structure and its implications on the electronic properties of both a single layer and two coupled graphene layers. In *chapter 3* transport studies on bulk single and bilayer graphene devices are presented. Besides discussing the influence of an external magnetic field the opening of a band gap in bilayer graphene in the presence of an electric field is demonstrated.

The density of states in a material is a determining factor for its transport properties. A method to directly measure this parameter is introduced in *chapter 4*, where quantum capacitance data for a single layer graphene device is shown.

As graphene nanoribbons constitute basic building blocks for more sophisticated nanostructures, their main characteristics will be presented thereafter. Whereas *chapter 5* reviews a number of experiments that are commonly carried out to characterize these narrow ribbons, further experiments are presented in *chapter 6* that provide a more detailed understanding of the transport mechanisms involved.

Chapter 7 is concerned with data recorded on a double-gated bilayer quantum dot. The energy spectrum of this system was studied both in an external B-field and E-field and first experiments with a pulsed gate were perfomed.

Conventionally, charge carriers in graphene are confined by etching. Since bilayer graphene can exhibit a band gap, electrostatic confinement might offer an alternative to etching. The possibility of employing split gates is investigated in *chapter 8*.

Finally, *chapter 9* concludes the work and provides an outlook for further experiments.

Chapter 2

Single and bilayer graphene - theoretical aspects

In order to understand the electronic properties of a material, its band structure has to be considered. With the knowledge of the energy dispersion, predictions of the quasiparticle properties can be made. Commonly, tight-binding calculations are employed to determine the band structure and we will discuss the results obtained for graphene in the following. Further, the implications for magnetotransport are presented.

2.1 Band structure of single layer graphene

Monolayer graphene is described by a honeycomb arrangement of carbon atoms. A sketch of a lattice section is shown in Fig. 2.1 (a), where the circles indicate the position of the carbon nuclei. The primitive cell of this system is identified to be a rhombus containing the basis of two carbon atoms (here denoted by $A1$ and $B1$) and it is spanned by the vectors $\mathbf{a}_1$ and $\mathbf{a}_2$. Hence, the hexagonal lattice can be seen as the result of the interpenetration of two sublattices $A1$ and $B1$.

Each one of the C atoms is sp^2 hybridized with its three neighbors via strong covalent bonds. The corresponding σ-bands (bonding and anti-bonding) are split to high absolute energy values and can therefore be neglected, when investigating the low energy band structure. The remaining valence electron in the p_z orbital leads to the formation of another pair of bands, the so-called π-bands. Carrying out a tight-binding calculation to obtain the dispersion relation of the graphene lattice as a function of the wave vector $\mathbf{q}$, yields [4]

$$\epsilon_{\pm}(\mathbf{q}) = \pm\gamma_0 \sqrt{1 + 4\cos^2(q_{\mathrm{x}}a/2) + 4\cos(q_{\mathrm{x}}a/2)\cos(\sqrt{3}q_{\mathrm{y}}a/2)}. \tag{2.1}$$

Here, only the nearest neighbor was included, assuming the hopping parameter γ_0 between adjacent sites (see Fig. 2.1 (a)). Further, the lattice constant $a = 2.46$ Å enters this equation. The plus and minus sign describe the π^*-band and the π-band,

respectively. In Fig. 2.1 (b), the resulting band structure is plotted for the first Brillouin zone (BZ). Whereas the bands exhibit a large energy separation of ≈ 20 eV in the center of the BZ, points of intersection at $\epsilon = 0$ are obtained at the six corners of the hexagonal reciprocal unit cell. For the Fermi surface to be located at these special points, two valence electrons per primitive cell are necessary to fill the valence band completely. The points denoted by K and K' are the basis of the reciprocal primitive cell and constitute the two inequivalent *valleys*, reflecting the presence of two sublattices Q and B.

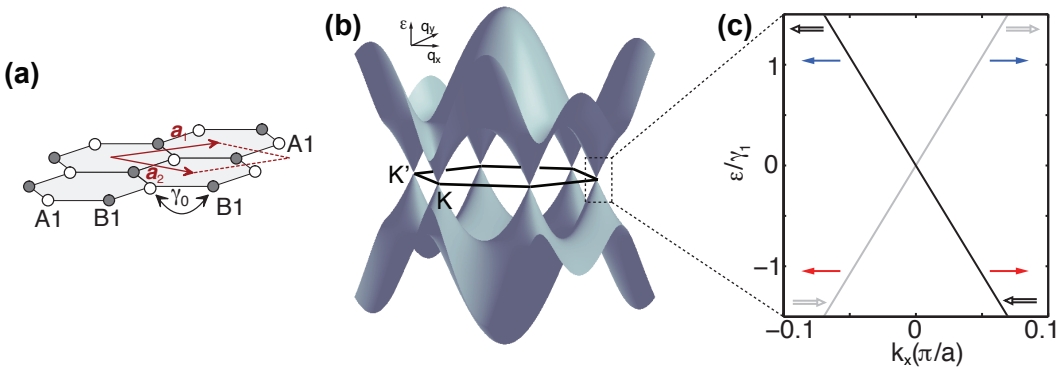

Figure 2.1: (a) Sketch of single layer lattice with sublattice atoms for $A1$ and $B1$. The unit cell with the corresponding vectors is indicated in red. Hopping between sites requires the hopping energy γ_0. (Adapted from Ref. 15) (b) Band structure according to Eq. (2.1) for the first Brillouin zone. (c) Zoom into (b) at the **K** point where the linear dispersion occurs. Blue and red arrows indicate the direction of motion for electrons and holes, respectively. Grey and black double arrows show the direction of the pseudo spin for the two parts of the spectrum. The energy axis is normalized to the interlayer hopping energy γ_1 to enable a direct comparison with Fig. 2.2 (b) and (c).

The experimentally reachable range is restricted to low energies and therefore, we focus on the dispersion around the K-points in the following. We replace the wave vector $\mathbf{q}$ by $\mathbf{k} = \mathbf{K} - \mathbf{q}$, describing the wave vector $\mathbf{k}$ with respect to the next $\mathbf{K}$ point. Expanding Eq. (2.1) around the corners of the Brillouin zone results in the linear dispersion relation for small $\mathbf{k}$

$$\epsilon_{\pm}(\mathbf{k}) = \pm\hbar \frac{\sqrt{3}\gamma_0 a}{2\hbar} |\mathbf{k}| = \pm\hbar v_{\mathrm{F}} |\mathbf{k}|, \tag{2.2}$$

with the Fermi velocity v_{F} in graphene being determined by the intralayer hopping energy γ_0. The corresponding energy eigenvalues are plotted Fig. 2.1 (c) and reveal the gapless dispersion of graphene as well as the electron-hole symmetry. One implication of the linear dispersion relation is the fact that the density of states in-

creases linearly with increasing $|\epsilon|$, namely $\mathcal{D}(\epsilon) = 2|\epsilon|/(\pi\hbar^2 v_{\mathrm{F}}^2)$ and has zero states at $\epsilon = 0$.

Besides the linear dispersion, another peculiarity of graphene is comprised in the description of its quasiparticles. Equation (2.1) gives the energy eigenvalues of the Dirac equation for massless fermions in two dimensions, which reads

$$\hbar v_{\mathrm{F}} \mathbf{k}\sigma\, \psi = \epsilon\, \psi, \tag{2.3}$$

with the Pauli matrices $\sigma = (\sigma_{\mathrm{x}}, \sigma_{\mathrm{y}})$ around $\mathbf{K}$ and $\sigma^* = (\sigma_{\mathrm{x}}, -\sigma_{\mathrm{y}})$ around $\mathbf{K}'$ and the speed of light c replaced by the Fermi velocity v_{F}. The two component state vector ψ takes the role of the spin in neutrino physics and is therefore called *pseudo spin*. The eigenvector is given by [16]

$$\psi_{\pm,\mathbf{K}}(\mathbf{k}) = \frac{1}{\sqrt{2}} \begin{pmatrix} e^{-i\theta/2} \\ \pm e^{i\theta/2} \end{pmatrix}. \tag{2.4}$$

It denotes the relative wave function amplitude on the two sublattices and includes the angle in momentum space, $\theta = \arctan(k_{\mathrm{x}}/k_{\mathrm{y}})$. Therefore, the direction of the pseudo spin is coupled to the direction of $\mathbf{k}$ and a *chirality* can be attributed to the quasiparticles. As indicated in Fig. 2.1 (c), for electrons, the pseudo spin points in the same direction as the momentum, whereas for holes they are aligned anti-parallel. According to the formal definition of the chirality being the projection of the pseudo spin onto the direction of motion, electron-like states have positive chirality whereas holes exhibit negative chirality.

This property has an important implication for transport. Since the direction of the pseudo-spin is maintained in scattering processes in the absence of a short range scattering potential, the only allowed transitions are from e.g. a right-moving electron to a right-moving electron or to a left-moving hole (see Fig. 2.1 (c)). The latter process is known from neutrino physic and is called Klein tunneling and poses a challenge for the confinement of charge carriers in graphene [17]. Nevertheless, the suppression of back scattering due to the fact that e.g. a right-moving electron cannot be scattered into a left-moving electron, is expected to allow for charge carrier mobilities of up to 200 000 $\mathrm{cm}^2/\mathrm{Vs}$ even at room temperature [18].

2.2 Band structure of bilayer graphene

As for single layer graphene, the band structure of bilayer graphene can be derived employing the tight-binding model [19–22]. Here, we consider two graphene layers being Bernal stacked as shown in Fig. 2.2 (a). Both layers consist of two sublattices, labeled $A1$, $B1$, $A2$ and $B2$ and the primitive cell consequently contains four atoms. Whereas each $B1$ site in the lower layer is located directly below an $A2$ atom of the upper layer, the $A1$ site does not have a direct neighbor in the upper layer and neither has the $B2$ atom in the lower layer. Besides the intralayer hopping energy γ_0, the interlayer hopping term γ_1 is taken into account, describing the (strong)

coupling between the $B1$ and $A2$ orbital. As a consequence of the pairing of lattice sites ($A2$-$B1$ and $A1$-$B2$), the two component spinors contain the wave function of two sublattices on different layers.

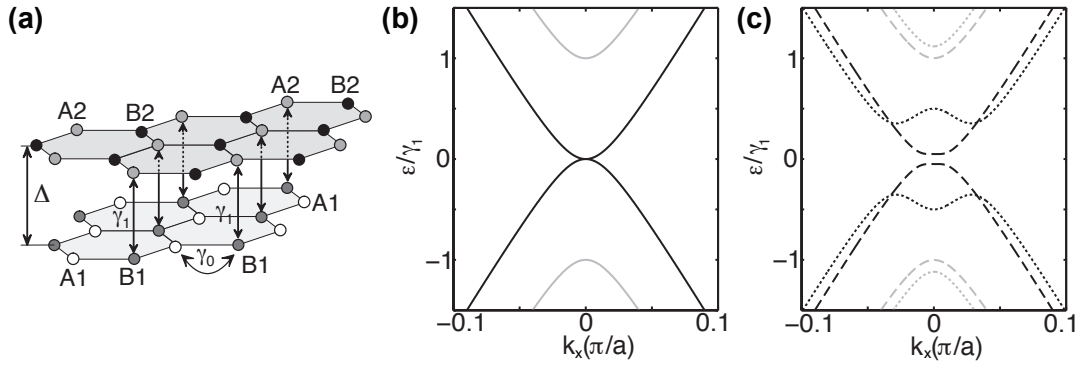

Figure 2.2: (a) Sketch of Bernal stacked bilayer lattice with sublattice atoms for $A1$, $B1$, $A2$ and $B2$. Hopping between sites requires the hopping energy γ_0 and/or γ_1. (Adapted from Ref. 15) (b) Energy dispersion around $\mathbf{K}$ for zero potential difference between the layers. High energy bands (plus sign in Eq. (2.5)) are plotted in grey and low energy bands (minus sign in Eq. (2.5)) in black. (c) Same as (b) but with finite asymmetry. $\Delta = 0.1\,\gamma_1$ (dashed line) and $\Delta = \gamma_1$ (dotted line).

The resulting energy dispersion near the $\mathbf{K}$ point is of the form

$$\epsilon_{\pm}^2(p) = v_{\mathrm{F}}^2\, p^2 + \gamma_1^2/2 + \Delta^2/4 \pm \sqrt{\gamma_1^4/4 + (\gamma_1^2 + \Delta^2)\, v_{\mathrm{F}}^2\, p^2}, \tag{2.5}$$

where p is the magnitude of the momentum near $\mathbf{K}$, v_{F} is the Fermi velocity as defined above and Δ is the difference between the on-site potentials in the two layers. Due to the strong coupling between $B1$ and $A2$, the two corresponding energy bands are split by $\gamma_1 = 0.39$ eV [23]. They are given by the plus sign in Eq. (2.5). Lower lying energy bands are formed, however, by interlinking the $A1$ and $B2$ site through hopping via the $A2$-$B1$ dimer. This part of the spectrum is described by Eq. (2.5) using the minus sign.

Figure 2.2 (b) shows the band energies of bilayer graphene for zero asymmetry ($\Delta = 0$) as a function of $k_{\mathrm{x}} = p_{\mathrm{x}}/\hbar$. The linear dispersion of single layer graphene is replaced by a parabolic spectrum around $\mathbf{K}$, indicating a finite mass of the quasiparticles. This mass is gained by the energy γ_1 needed for the transition from $A1$ to $B2$ according to $m = \gamma_1/2v_{\mathrm{F}}^2 \approx 0.03 \cdot m_{\mathrm{e}}$ [22]. As a consequence of the parabolic spectrum, the density of states is independent of energy for bilayer graphene. In the limit of large momenta, the linear spectrum is recovered. Further, the energy dispersion is gapless at the $\mathbf{K}$ point. It is important to realize, however, that the electron and hole band in bilayer graphene effectively just touch each other in this point,

whereas they are the natural prolongation of one another in single layer graphene [24].

This condition facilitates the opening of a band gap. As a potential difference is introduced to the system, the bands are shifted to higher $|\epsilon|$. This is shown in Fig. 2.2 (c) for $\Delta = 0.1\,\gamma_1$ (dashed line) and $\Delta = \gamma_1$ (dotted line). At the **K** point, the splitting is given by $|\epsilon_\pm(p=0)| = \sqrt{\gamma_1^2 + \Delta^2/4}$ for the high energy bands and by $|\epsilon_\pm(p=0)| = |\Delta|/2$ for the lower ones. For large asymmetries, the spectrum adopts a "mexican hat" shape. This implies that the true energy gap of the system occurs at finite momentum $\mathbf{k} = 0$, where it takes the values $E_{\mathrm{gap}} = |\Delta|\gamma_1/\sqrt{\gamma_1^2 + \Delta^2}$. Theoretically, band gap values of up to $E_{\mathrm{gap}} \approx 200$ meV should be achievable in the experimentally available range.

2.3 Graphene in a perpendicular magnetic field

The trajectory of a charged particle in a perpendicular magnetic field follows an orbit due to the Lorentz force acting on it. Since the wave character of electrons leads to interference effects along such orbits, only discrete energies exist for which constructive interference occurs. These are referred to as Landau levels and allow for the observation of the quantum Hall effect [25].

The density of states in conventional semiconductor 2DEG condenses into a sequence of Landau levels at energies $E_\pm^{\mathrm{N}} = \pm\hbar\omega_{\mathrm{c}}(N + \frac{1}{2})$, where N is an integer numbering the Landau levels. Each filled Landau level contributes with ge^2/h to the Hall conductivity, resulting in steps at $\sigma_{\mathrm{xy}} = i\,ge^2/h$, where g is the LL-degeneracy and i an integer. In Fig. 2.3 (a), the position of the LLs as well as the ladder for the Hall conductivity are shown as a function of charge carrier density. The factor eB/h describes the Landau level degeneracy n_{L} of the system.

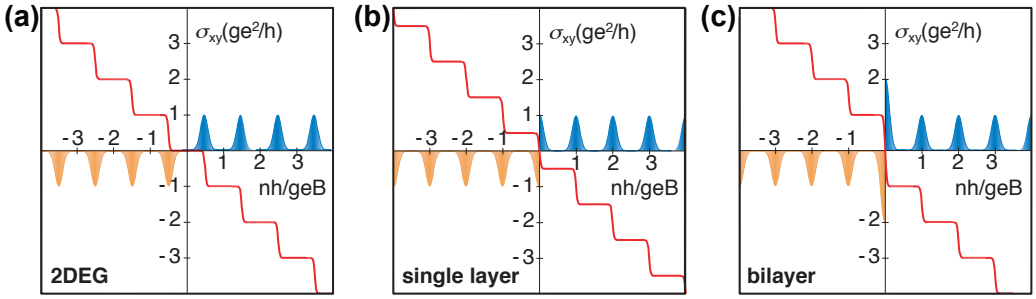

Figure 2.3: QHE for different materials. The position of the LLs is marked by the peaks and the dependence of σ_{xy} on the charge carrier density is plotted as the red trace. (a) Conventional 2DEG, (b) single layer graphene and (c) bilayer graphene. (Figure reprinted from Ref. 10)

We now compare the spectra of graphene shown in Fig. 2.3 (b) and (c) to the standard 2DEG displayed in Fig. 2.3 (a). An obvious difference between the conventional semiconductor and the case of graphene is the position of the plateaus in σ_{xy}. For single layer graphene the plateaus are located at $\sigma_{xy} = \pm g e^2/h\,(i - \frac{1}{2})$, meaning that they are shifted by $\frac{1}{2}\,ge^2/h$. Nevertheless, the step height is given by ge^2/h, with $g = 4$ accounting for both spin and valley degeneracy. Bilayer graphene on the other hand follows the conventional quantization of $\sigma_{xy} = \pm i\,ge^2/h$ for $i \geq 1$ ($g = 4$). The plateau at zero energy is absent and the conductance increases by of $8e^2/h$ for the step around zero.

A way of understanding the observed shift in the conductivity spectrum is provided by the pseudo spin of graphene, which leads to the accumulation of a Berry phase. As a quasiparticle adiabatically rotates its pseudo spin by $\theta = 2\pi$, meaning it moves between the two sublattices, it picks up a phase shift of $j\pi$ ($j = 1$ for SL and $j = 2$ for BL) and its wave functions change sign (see Eq. (2.4)). This Berry phase contributes to the total phase, which a particle acquires while encircling a cyclotron orbit. In single layer graphene it induces a phase shift of π to the Shubnikov- de Haas oscillations and in turn an offset of $2e^2/h$ to the Hall conductivity. For bilayer graphene it is not straight forward to see, how the Berry phase of 2π influences the spectrum [10]. We will therefore use another argument to explain the observed behavior.

Whereas single layer graphene shows a linear density of states, the number of states in bilayer is constant with energy. Since the states have to condense into the discrete Landau levels, the spacing between energy levels is expected to differ for single and bilayer. Indeed, the sequences are given by [22, 26]

$$E_{\pm}^{\mathrm{N}} = \pm\sqrt{2e\hbar v_{\mathrm{F}}^2 BN} \quad \text{(SL) and} \qquad E_{\pm}^{\mathrm{N}} = \pm\hbar\omega_{\mathrm{c}}\sqrt{N(N-1)} \quad \text{(BL)},$$

where B is the magnetic field and ω_{c} is the cyclotron frequency. The bilayer spectrum equals the one for conventional semiconductors except for an additional level at zero energy, which contains both the $N = 0$ and the $N = 1$ LL. Instead of the four-fold degeneracy due to spins and valleys, it is hence eight-fold degenerate and leads to a doubled step height in σ_{xy}. Single layer graphene exhibits an $N = 0$ Landau level at $\epsilon = 0$ as well, which is only four-fold degenerate, however. It is shared by electrons and holes and hence can accommodate only $2\,n_{\mathrm{L}}$ instead of $4\,n_{\mathrm{L}}$ of each carrier type. Since σ_{xy} features a plateau if the energy is lying in-between two LLs, the $N = 0$ LL induces a shift of the conductivity ladder by $2e^2/h$.

For biased bilayer graphene, a band gap opens at zero energy and the $N = 0$ Landau level splits. As a consequence, a conductance plateau evolves at $\sigma_{xy} = 0$ and the energy spectrum of a conventional gapped semiconductor is recovered [27].

Chapter 3

Electronic transport properties of bulk graphene

Studying electronic transport of a material gives insight into the properties of the particles contributing to transport and the dynamics involved (e.g. scattering events). Before investigating nanostructured devices, it is therefore instructive to get a feeling for the characteristic parameters used to describe electronic properties of bulk samples. These include for instance the doping level, the charge carrier mobility, the mean free path and, in a double gated bilayer graphene device, the size of the band gap.

In this chapter, we will introduce the basic measurements commonly carried out to determine the material quality and analyze them accordingly by means of a single layer device and two bilayer graphene structures.

3.1 Sample fabrication and measurement setup

Mechanical exfoliation of natural graphite flakes is commonly used to extract thin graphene flakes and deposit them on Si/SiO_2 substrate [5]. The thickness of the SiO_2 is chosen in such a way, that the difference between the reflected intensity of light impinging on the wafer in the presence and absence of graphene is maximized [28]. A 285 nm thick oxide layer indeed allows to identify single and bilayer flakes using an optical microscope. Subsequent atomic force microscope (AFM) measurements as well as Raman spectroscopy [29, 30] were performed to verify their single or bilayer nature.

In order to electrically contact the graphene flakes, electron beam lithography (EBL) is carried out in a clean room. For this purpose, the chip is covered with a thin layer of PMMA (poly methyl methacrylate). Since the chains of this polymer dissociate if high-energy electrons impinge, EBL can be used to modify the resist in certain areas. After the writing step, the short polymer chains are soluble in a developer and hence the irradiated areas are no longer covered by resist. Next, a metal stack of 2 nm Cr and 40 nm Au is deposited by electron beam evaporation

followed by a lift-off process.

Subsequently, the chip is glued into a ceramic chip carrier with silver epoxy and the metal contacts are connected to the chip carrier via Au bond wires.

For the sample presented in Sec. 3.3, additional process steps are necessary to define the top gate. As a dielectric material, hexagonal boron nitride (BN) was used. Since this material is mechanically exfoliated as well and extracted in micrometer size flakes only, a mechanical transfer technique was developed by Dean et al. [31] to place a BN flake at a desired position on a chip (see more details in Appendix C). After covering the contacted graphene flake with $\approx$ 10 nm thick BN, top gate electrodes are defined by EBL. Finally, metal is evaporated (0.5 nm Cr and 45 nm Au) and the structure is revealed after the subsequent lift-off.

The measurements presented here were all carried out in variable temperature inserts with a base temperature of $T \approx 1.7$ K. Since bulk structures exhibit low impedance, a constant AC current bias was applied via a series resistance (typically 10 MΩ or 100 MΩ) connected to the output of a lock-in amplifier. If possible, four-point measurements were performed to exclude the contact resistance of the voltage probes from the measured signal.

3.2 Comparison of single layer and bilayer graphene

3.2.1 Electric field effect in graphene

As discussed in the previous section, graphene devices are conventionally fabricated on a Si substrate which is covered by a SiO_2 layer. Utilizing the field effect, the highly doped silicon serves as a global back gate (BG), meaning that by changing the applied gate voltage the charge carrier density in the graphene structure is tuned. According to the plate capacitor model, the density in the graphene sheet is changed like $n = (\epsilon_0 \epsilon_{SiO_2}/e d_{SiO_2}) \cdot \Delta V_{BG}$, where $\epsilon_{SiO_2} = 3.9$ is the dielectric constant of SiO_2, ϵ_0 is the vacuum permittivity and $d_{SiO_2} \approx 285$ nm is the thickness of the SiO_2 oxide. Measuring the resistance R of a graphene flake as a function of applied back gate voltage gives information about the carrier mobility μ according to Drude's model of diffusive transport $\sigma = n\mu e$, which relates the conductivity σ and the charge carrier density n by the proportionality factor μ.

Two representative graphene flakes are characterized in this section - a single layer and a bilayer device. As displayed in Fig. 3.1 (a) and (d), the metallic contacts are arranged in conventional Hall bar configuration. The flakes are however not etched into Hall bar geometry to avoid disorder, which is possibly induced by additional processing steps.

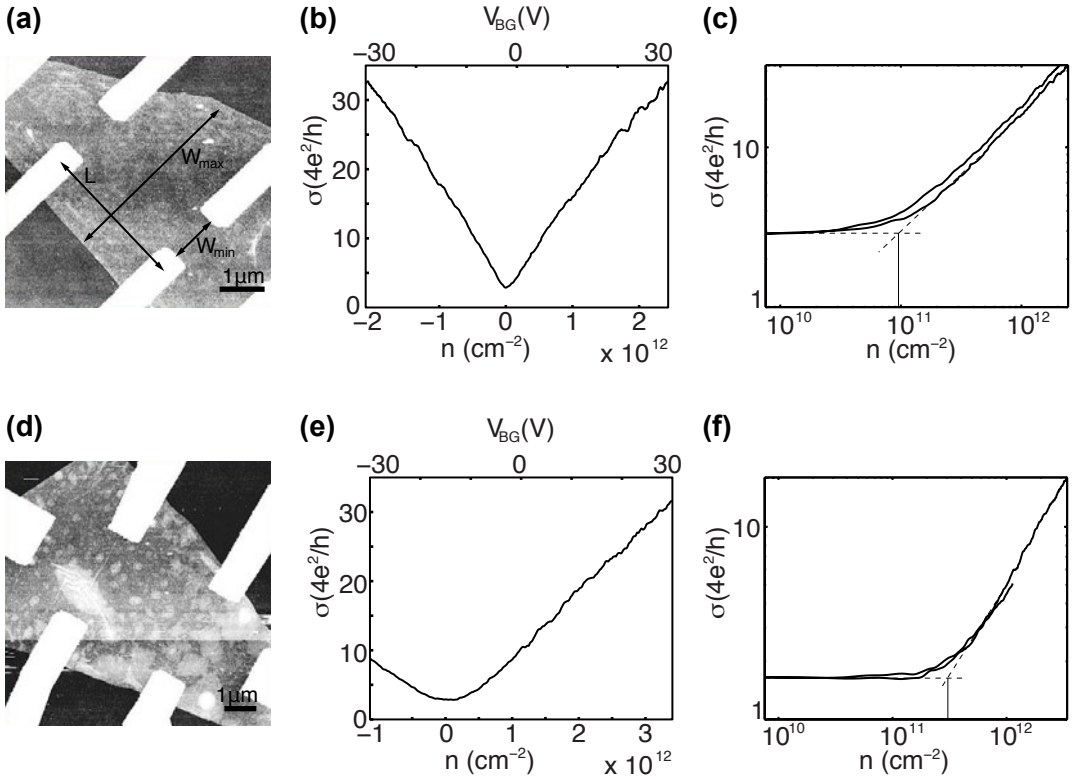

Figure 3.1: Comparison of single layer (panels in upper row) and bilayer characteristics (panels in lower row). (a) and (d) Atomic force micrograph of unpatterned flakes used for the Hall measurements. The white regions are the gold electrodes and the light grey areas are the graphene. Indicated are the dimensions used to determine the conductivity. For (a) these are $W_{\min} = 1.1$ μm, $W_{\max} = 3.45$ μm and $L = 3.25$ μm and for (d) $W_{\min} = 2.8$ μm, $W_{\max} = 4.5$ μm and $L = 3.5$ μm. (b) and (e) Back gate characteristics measured at $T = 1.7$ K with constant current bias of 100 nA. Conductivity σ as a function of V_{BG} (upper x-axis) and the charge carrier density n determined from the plate capacitor model. (c) and (f) Double logarithmic plot of σ vs n to determine the saturation density (indicated by the vertical line).

Single layer graphene

The back gate characteristics obtained for the single layer device is displayed in Fig. 3.1 (b). The measured resistance R and the conductivity σ are related via the device length L and width W by $\sigma = 1/R \cdot L/W$. Since the width of the flakes is not well defined here, we take the largest value ($W_{\max}$ in Fig. 3.1 (a)) to obtain the lower bound for the charge carrier mobility μ. Whereas the upper x-axis displays the measurement parameter V_{BG}, the charge carrier density n is given by the bottom axis.

Clearly, a minimum in the conductivity is visible as the BG is tuned from negative to positive voltages. This is expected for single layer graphene since the density of states decreases linearly as the absolute value of the Fermi energy $|E_F|$ is reduced. Ideally, the graphene sheet exhibits no density of states and hence zero conductivity at the charge neutrality point (CNP). In experimental data, a finite value of the order of $4e^2/h$ is obtained, however. Whether this value is universal and the origin of it are still under dispute [16, 32–37]. As an explanation, the formation of electron-hole puddles due to potential fluctuations is put forward. Within these puddles, a finite density of states is present and due to Klein tunneling, charge carriers can be transferred through the graphene sheet, leading to an increased conductance. As an enhanced disorder amplitude is induced by impurities residing on the graphene surface, scattering of charge carriers will reduce the conductivity on the other hand. It is indeed observed that clean samples (e.g. supported by BN or suspended) exhibit an increased minimum conductivity [31, 38, 39] as compared to devices with a high charge carrier inhomogeneity.

The shift of the charge neutrality point away from zero gate voltage indicates the doping asymmetry. In the back gate dependence shown in Fig. 3.1 (b), the minimum of σ is located at a slightly negative voltage, indicating that an excess of positive dopants is present. When determining the density n, this shift was compensated for.

Since the position of the charge neutrality point only provides information about the relative doping of positive and negative impurities, a closer look at the curvature of the conductivity trace at its minimum is instructive [39]. In the double logarithmic plot of Fig. 3.1 (b) two regimes are observed for the conductivity. Below a threshold density (indicated by the vertical line), the conductivity is independent of the number of charge carriers in the system. Here, the transport is dominated by potential fluctuations and the Drude model is not valid anymore. We can extract a saturation density of $n_{sat} \approx 9.5{\cdot}10^{10}$ cm^{-2} for the single layer device. Following Ref. 39, we can determine the Fermi energy at which the saturation sets in to be $E_{F,sat} = \hbar v_F \sqrt{\pi n_{sat}} \approx 35$ meV. Such a low value is achieved only rarely in graphene flakes supported by SiO_2 [40] and indicates the high quality of the present flake.

By fits to the linear part of the conductivity curve, we can estimate the charge carrier mobility. The curve is symmetric indicating that electrons and holes exhibit the same carrier mobility. As a lower limit, assuming the whole width of the flake contributing to transport, we obtain $\mu_{min} \approx 14\,400$ cm^2/Vs. Supposed that only the inner part, defined by the distance W_{min} between the contacts, carries current, the upper limit for the mobility $\mu_{max} \approx 45\,200$ cm^2/Vs is found. In agreement with the extraordinarily low disorder density n_{sat}, the mobility values are among the highest reported so far for non-suspended graphene on SiO_2. This finding demonstrates, that the fabrication process does not necessarily affect the transport characteristics.

From these values, the minimum mean free path for $n = 2{\cdot}10^{12}$ cm^{-2} is determined to be $l_{mfp} = (\hbar\mu_{min}/e)\sqrt{\pi n} \approx 238$ nm. A comparison to the system size hence justifies the application of the Drude model for diffusive transport a posteriori.

Bilayer graphene

We now discuss the data recorded for the bilayer device (see Fig. 3.1 (e)). As it is apparent from the large shift of the charge neutrality point to the negative side ΔV_{CNP} = -15 V, the relative level of positive dopants is comparably high. The conductivity curve nevertheless exhibits similar slopes for the hole transport regime on the left hand side of the CNP and for the electron regime on the right hand side.

Comparing the curves in Fig. 3.1 (b) and (e) the region of non-linear $\sigma(n)$ is much broader for the bilayer flake. This finding is resembled in Fig. 3.1 (f), where σ is constant for charge carrier densities up to $n_{\mathrm{sat}} \approx 2{\cdot}10^{11}$ cm^{-2}. For bilayer graphene, the Fermi energy is related to the density as $E_{\mathrm{F,sat}} = (\hbar^2 \pi n_{\mathrm{sat}})/2m^*$ and hence the saturation energy is $E_{\mathrm{F,sat}} \approx 80$ meV. Although this value is more than twice the one for the single layer device above, the obtained disorder amplitude is comparable to average single layer flakes [41].

For the mobilities, we extract $\mu_{\mathrm{min}} \approx 5\ 500$ cm^2/Vs and $\mu_{\mathrm{max}} \approx 9\ 000$ cm^2/Vs, which corresponds to a mean free path $l_{\mathrm{mfp}} \approx 90$ nm at a density of $n = 2{\cdot}10^{12}$ cm^{-2}.

Hence, the parameters extracted from the back gate characteristics provide a consistent picture of the device quality for both devices.

3.2.2 Magnetotransport in graphene

The smoking gun of a single layer of graphene is its quantum Hall effect since the chirality of the massless fermions present in graphene leads to conductance quantization at half-integer multiples of $4e^2/h$ in a finite magnetic field. For bilayer graphene, the coupling between the two graphene sheets imposes a finite mass to the charge carriers. Nevertheless, they remain chiral particles and accumulate a Berry's phase of 2π along cyclotron orbits (instead of π for single layer graphene). The resulting conductance ladder exhibits plateaus at integer multiples of $4e^2/h$ except for the one at zero, which is absent due to the presence of a combined Landau level (LL) consisting of the lowest electron and hole LL.

Magnetotransport was investigated in the devices introduced in the previous section. Throughout the measurements the magnetic field was oriented perpendicular to the graphene plane.

Single layer graphene

Figure 3.2 (a) shows the back gate curve recorded at $B = 7$ T for the single layer flake. Both the Hall conductivity $\sigma_{\mathrm{xy}} = \rho_{\mathrm{xy}}/(\rho_{\mathrm{xx}}^2 + \rho_{\mathrm{xy}}^2)$ and the longitudinal resistance R_{xx} are displayed in the blue and green trace, respectively.

As predicted, the transverse conductivity shows pronounced plateaus at half-integer values. This characteristic ladder of conductance steps is well developed for the complete back gate range.

The longitudinal resistance is expected to take finite values if the Fermi energy

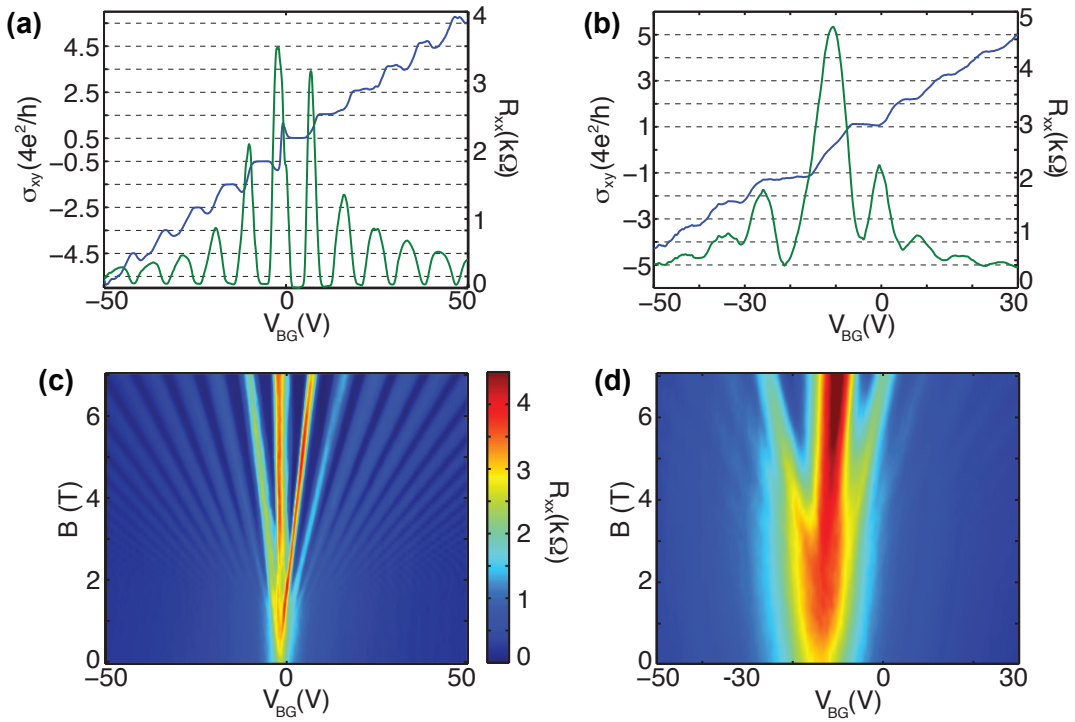

Figure 3.2: (a) Back gate dependence at $B = 7$ T for single layer. Displayed are the Hall conductivity σ_{xy} (blue trace) and the longitudinal resistance R_{xx} (green trace). (b) Same as (a) but for bilayer graphene. (c) R_{xx} as a function of V_{BG} and B-field for single layer graphene. (d) Quantum Hall effect of bilayer graphene (color bar of (c) is valid for (d) as well). All measurements were recorded at $T = 1.7$ K with a current bias of 100 nA on the flakes displayed in Fig. 3.1 (a) and (d).

lies in a Landau level. If E_F is located in between two LLs however, no back scattering between edge channels takes place and the resistance drops to zero. This effect is observed in Fig. 3.2 (a), where the resistance peaks indicate the position of the LLs. The maximum at $V_{BG} \approx$ -2 V corresponds to the $N = 0$ LL, which is shared by electrons and holes. The system takes constant filling factor ν at the resistance minima. Starting from zero BG the values are $\nu = \pm 2, \pm 6, \pm 10...$ where the factor 4 results from the four-fold energy degeneracy in graphene caused by the two-fold sublattice and spin degeneracy.

The remarkable quality of the flake is visible in Fig. 3.2 (c), where R_{xx} is plotted as a function of the applied back gate voltage for varying magnetic fields. Since the LLs are unveiled by the resistance maxima (Shubnikov-de Haas maxima), such a plot enables to follow how the density position of the quantized energy levels (LLs) is changed by an external field. Lines of constant filling factor are located at the density values expected from the relation $\nu = nh/B|e|$. In the present measurement,

the lowest Landau levels (N = 0, -1 and 1) can be followed down to almost B = 0 where they merge into the resistance peak characteristic for the charge neutrality point. The next higher energy levels fade away only at B = 2 T and filling factors up to $\nu = \pm 62$ can be distinguished at the highest densities studies here.

Bilayer graphene

Looking at the corresponding measurements for the bilayer flake, the differing behavior of charge carriers in two coupled graphene layers is verified.

In Fig. 3.2 (b), the Hall conductivity is quantized at integer multiples of $4e^2/h$ and shows no plateau at zero. The sample therefore exhibits the characteristics of bilayer graphene.

For the longitudinal resistance a broad peak is present, where σ_{xy} exhibits the enlarged step height indicating the position of the CNP. Whereas the resistance minima at higher densities are equally spaced, a doubled spacing in V_{BG} is observed between the minima lying lowest in density. This is a result of the eight-fold degenerated $N = 0$ LL developing at the CNP and the associated sequence of constant filling factors is $\nu = \pm 4, \pm 8, \pm 12...$ The fact that R_{xx} does not fall to zero in-between Landau levels, implies that charge carriers in the edge channels still experience scattering. As discussed in the previous section, the disorder is comparably high in the present flake and hence it is well conceivable that impurities lead to an enhanced number of scattering events.

Nevertheless, a Landau fan is clearly visible if the applied B-field is changed (see Fig. 3.2 (d)). Shubnikov-de Haas oscillations emerge at B = 3 T and are shifted linearly to higher densities as the magnetic field is increased. The positions of their minima agree with the ones predicted by $\nu = nh/B|e|$ using the density n determined from the plate capacitor model.

In summary, both samples exhibit the magnetotransport characteristics anticipated for the respective number of layers. The finding that all features are more pronounced for the single layer flake as compared to the bilayer device, reflects the significant influence of potential fluctuations on transport properties of the system.

3.3 Top gated bilayer graphene

In order to split the valence and conduction band in bilayer graphene, breaking of the layer symmetry is required. Applying a potential difference between the upper and the lower graphene layer hence induces a band gap in the energy spectrum. Such an asymmetry is imposed by an electric field oriented perpendicularly to the bilayer graphene plane. To reach high E-field values and at the same time enable charge carrier density tunability, a double-gated device configuration was developed [42–44].

An optical microscope image of the sample characterized here is shown in Fig.

3.3 (a). The graphene flake (outlined by the black dashed line) is covered by a 8 nm thick BN flake. The top gate electrode (marked red) is spanning across the complete width of the flake and is 8 μm wide and 900 nm long. The Ohmic contacts used as voltage probes in the four-point measurements carried out here are marked by the blue lines.

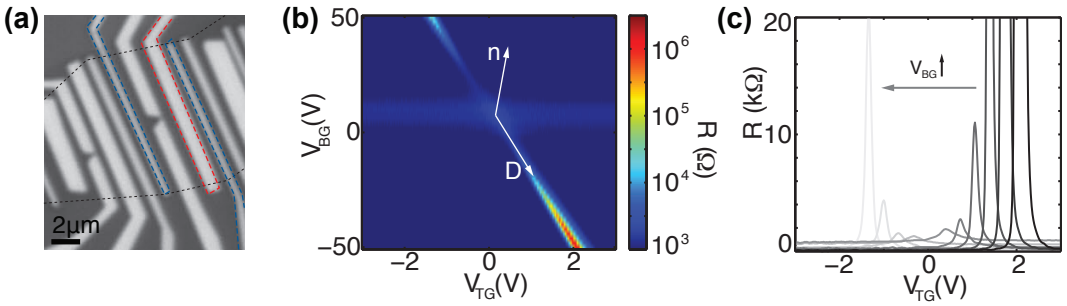

Figure 3.3: (a) Optical microscope image of the top gated device. The top gate tuned in the measurements discussed here is marked by the red line and the electrodes used as voltage probes are indicated by blue lines. The graphene flake is outlined with a black dashed line. (b) Four point resistance as a function of top gate and back gate. (c) $R(V_{\mathrm{TG}})$ at constant V_{BG} between -50 V and +50 V. The back gate was changed in steps of 10 V. All measurements were taken at $T = 1.6$ K with $I_{\mathrm{bias}} = 1$ nA.

3.3.1 Tunable band gap

Figure 3.3 (b) displays the resistance through the device as a function of back gate and top gate voltage. The arrows shown in the plot indicate the axes along which the density n in the graphene and the displacement field D across the layers are tuned. These two parameters are defined by the applied gate voltages via the field effect. The charge carrier density is changed according to

$$n = \frac{\epsilon_0 \epsilon_{\mathrm{SiO_2}}}{e d_{\mathrm{SiO_2}}}((V_{\mathrm{BG}} - V_{\mathrm{D,BG}}) + \alpha_{\mathrm{TG/BG}}(V_{\mathrm{TG}} - V_{\mathrm{D,TG}})), \tag{3.1}$$

where $V_{\mathrm{D,BG}}$ and $V_{\mathrm{D,TG}}$ are the position of the charge neutrality point at effectively zero E-field for the back gate and top gate, respectively, and $\alpha_{\mathrm{TG/BG}}$ is the ratio between the top gate and the back gate capacitance. For the displacement field, the relation reads

$$D = \frac{\epsilon_{\mathrm{SiO_2}}}{d_{\mathrm{SiO_2}}}((V_{\mathrm{BG}} - V_{\mathrm{D,BG}}) - \alpha_{\mathrm{TG/BG}}(V_{\mathrm{TG}} - V_{\mathrm{D,TG}})). \tag{3.2}$$

Moving along the displacement axis at zero density, the maximal achievable values are D = -1.64 V/nm for the negative V_{BG} regime and D = 1.05 V/nm for positive value of V_{BG}. According to self consistent tight-binding calculations [21],

relating the applied displacement field to the splitting between the valence and conduction band, a band gap of up to $E_{\mathrm{gap}} \approx 200$ meV should be opened in the present device.

For each TG trace at constant V_{BG} in Fig. 3.3 (b), a resistance maximum R_{max} is observed at the cross-over from hole-like to electron-like transport. Since the position of the charge neutrality point is shifted in gate space due to the capacitive coupling of the two gates, the slope of R_{max} gives the relative lever arm $\alpha_{\mathrm{TG/BG}}$ between top gate and back gate. From the extracted value $\alpha_{\mathrm{TG/BG}} \approx 28.5$, the thickness of the BN flake can be determined assuming the dielectric constant of BN to be $\epsilon_{\mathrm{BN}} = 3.5$ [44]. The obtained value of $d_{\mathrm{BN}} \approx 9$ nm agrees well with the one measured in an atomic force micrograph.

A horizontal stripe of increased resistance around $V_{\mathrm{BG}} = 10$ V is observed in Fig. 3.3 (b). This originates from the area of the graphene flake which is not covered by a top gate and contributes as a back gate dependent series resistance to transport. The enhanced resistance hence marks the electron hole cross-over in the graphene section which is tuned only by one gate.

Looking at cuts in the two-dimensional plot illustrates the opening of a band gap. In Fig. 3.3 (c) the back gate is stepped by 10 V for each consecutive top gate curve. Starting from V_{BG} = -50 V each step induces a shift to more negative top gate voltages. At the same time the amplitude of the resistance peak monotonously decreases as the displacement is reduced and increases again after passing the back gate value at which the D-field is effectively zero. Within the range covered here the maximum resistance takes values between $R_{\mathrm{max}} \approx 1$ kΩ and 1.5 MΩ indicating that the flake is getting more and more insulating as $|D|$ increases.

3.3.2 Temperature dependence

From the previously discussed transport experiments alone, the size of the band gap cannot be determined. We therefore discuss the temperature dependence of R_{max} in the following. In order to avoid thermal activation of charge carriers by dissipation, we changed the setup to measure with constant voltage bias of $V_{\mathrm{bias}} = 50$ μV.

Top gate traces at V_{BG} = -50 V (maximum achievable D-field) were taken at temperatures between 1.7 K and 16.5 K (see Fig. 3.4 (a)). As the temperature is increased, the peak height falls meaning that transport gets facilitated by the thermal energy provided to the system. Extracting the amplitude of the resistance peak as a function of temperature should give information about the character of the thermally activated transport.

Assuming an ideal band gap without subgap states, the resistance is expected to increase exponentially with increased temperature. From the relation $R \propto \exp(-E_{\mathrm{gap}}/2k_{\mathrm{B}}T)$ one can hence extract the size of the band gap E_{gap}. In Fig. 3.4 (b) the maximum values of R are plotted as a function of $1/T$ in a logarithmic plot. The dependence between the two plotted parameters is sublinear, meaning that the conductance is less strongly suppressed than predicted for an ideal system.

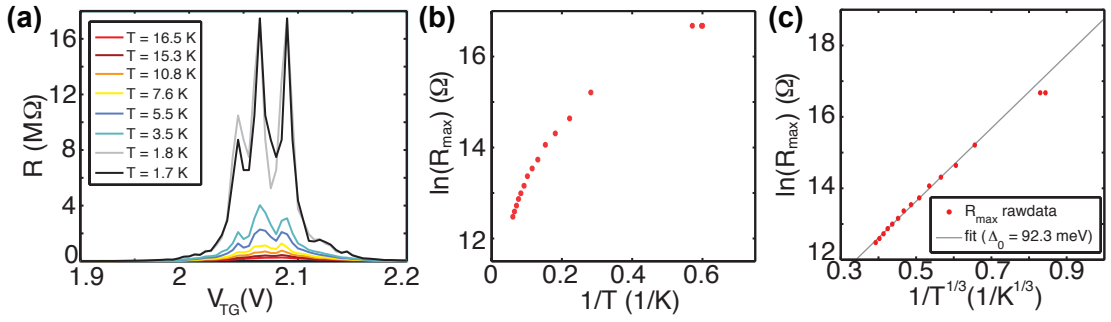

Figure 3.4: (a) Temperature dependence of $R(V_{\mathrm{TG}})$ at V_{BG} = -50 V. Conductance data was recorded with lock-in technique at $V_{\mathrm{bias}} = 50\ \mu$V and converted into resistance data afterwards. (b) Extracted resistance maxima of traces in (a) as a function of $1/T$. (c) Data of (b) as a function of $1/T^{1/3}$ to determine characteristic energy scale of hopping transport by a linear fit (grey line).

Since the minimum disorder amplitude achieved on SiO_2 supported flakes is on the order of several 10 meV (see discussion of $E_{\mathrm{F,sat}}$ above), energy levels inside the gap are most likely available for charge carriers leading to a reduction of R_{max}. To derive an upper limit for the band gap, we include only the data obtained for the seven highest temperatures into a linear fit in Fig. 3.4 (b). A value of $E_{\mathrm{gap}} \approx 4$ meV is yielded, which is much smaller than the theoretically expected one.

Similar behavior was observed in other transport experiments [42, 43]. In these studies, the values for $\ln(R_{\mathrm{max}})$ were found to depend linearly on $1/T^{1/3}$ and interpreted to be indicative for variable range hopping due to the finite density of states inside the band gap. Replotting the data as a function of $1/T^{1/3}$ indeed reveals a linear slope as shown in Fig. 3.4 (c). From the theory developed by Mott, describing variable range hopping in two dimensions [45, 46], we can extract the characteristic energy Δ_0 from the slope of a linear fit to the data. As shown in Appendix A, we can determine the localization length ξ and the optimum hopping distance d_{opt} in the system being $\xi \approx 18$ nm and $d_{\mathrm{opt}}(1.7\ \mathrm{K}) \approx 52$ nm. These estimates illustrate that indeed a large number of localized states are present in the system and charge carriers need to complete a series of hops to be transferred through the system.

In conclusion, we have observed the opening of a band gap in dual-gated bilayer graphene in transport experiments. Our analysis of the temperature dependence exhibited by transport properties shows, that subgap states are present and lead to an enhanced conductance as compared to an exponential decay at the lowest temperatures. The model of variable range hopping in two dimensions, on the other hand, can well describe the data and is hence a possible microscopic mechanism behind transport.

3.4 Conclusion

In summary, we have investigated unpatterned graphene flakes consisting of one and two layers. All devices showed the respective characteristic properties in transport measurements. Additionally, we have demonstrated, that a band gap can be opened in a bilayer graphene flake by a perpendicular electric field, which breaks the symmetry between the layers.

The transport properties observed in this chapter originate from the exceptional density of states of graphene. We will therefore focus on this quantity and present measurements on a single layer device.

Chapter 4

Quantum capacitance and density of states of single layer graphene

The number of available electronic states at the Fermi level determines the transport characteristics of electronic devices. A solid understanding of the density of states is hence crucial for the interpretation of the electronic properties a given system exhibits. In two-dimensional electron gases in semiconductor heterostructures, experiments have been accomplished mapping the density of states directly via the quantum capacitance already in the 1980s [47, 48] and are nowadays standard characterization tools for these structures. More recently, the energy level spectrum of carbon nanotubes was experimentally observed in measurements of the quantum capacitance [49].

An infinite single-layer graphene sheet is expected to show a linear density of states that vanishes at the charge neutrality point [4]. The experimental findings of conductance measurements, however, contrast this theoretical prediction by showing a minimum conductivity of the order of $4e^2/h$ which indicates a finite charge carrier density [40, 50]. Since the quantum term in the capacitance gives insight to the density of states, both theoretical [51, 52] and experimental [18, 53, 54] studies of the quantum capacitance have been carried out for graphene within the last years. All measurements show a non-zero value of the density of states at the Dirac point which is commonly interpreted as originating from potential fluctuations in the graphene sheet. Here we discuss experiments on a top gated single-layer graphene ribbon and analyze the data in a self-consistent manner not making any theoretical assumptions about the density of states.

4.1 Theoretical background

A classical plate capacitor consists of two well conducting plates arranged in parallel to each other and separated by a dielectric layer of a certain thickness. Its capacitance can be calculated considering material and geometric parameters of the system. If the density of states on one of the plates is finite, however, adding a

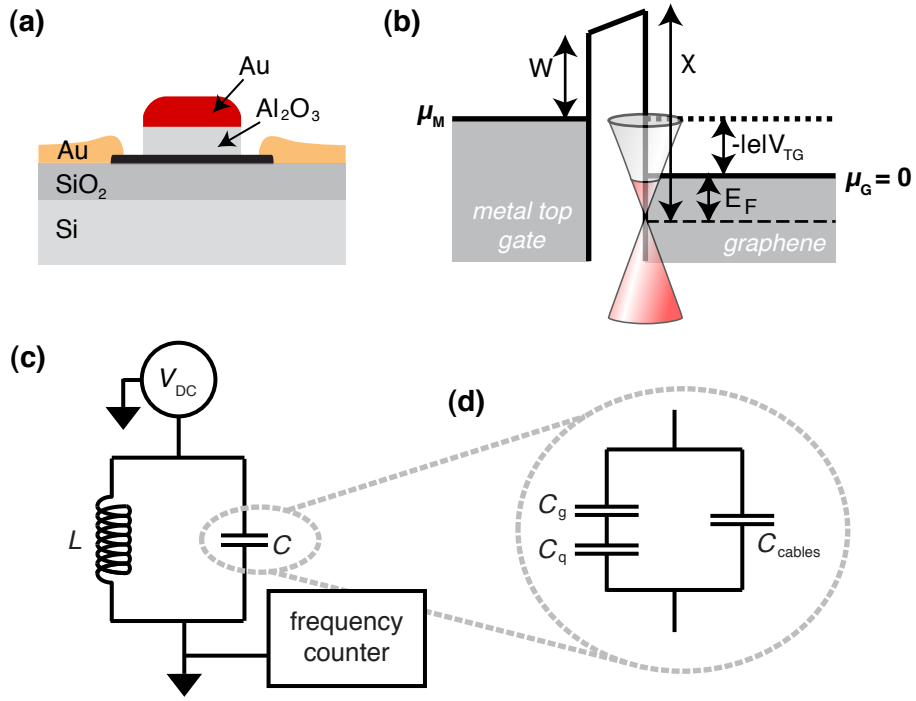

Figure 4.1: (a) Schematic cross section of a top gated graphene sample. The graphene flake (black) is contacted with gold electrodes (orange) and covered partly by an alumina/gold top gate (grey/red). (b) Schematic of the electrostatics of the structure showing the change in electrochemical potential between the top gate electrode and the graphene sheet. (c) Circuit scheme of the measured system.

charge carrier costs kinetic energy due to the shift of the Fermi level. Since this required extra energy reduces the total capacitance of the system the density of states is directly reflected in an additional capacitance term. As visualized in the cross section in Fig. 4.1 (a) a locally gated graphene device can be viewed as a plate capacitor with one plate being the top gate electrode and the other being the graphene sheet.

The total capacitance between the gate and the electron gas can be derived from the electrostatics describing the system [55–57]. A finite applied bias $-|e|V_{\mathrm{TG}}$ introduces a difference in the electrochemical potentials of the metal top gate electrode, μ_{M}, and of the graphene, μ_{G}. As sketched in Fig. 4.1 (b) it consists of the Fermi energy E_{F} in graphene, the electrostatic potential across the dielectric as obtained from solving Poisson's equation and the two work functions χ and W of graphene and the metal, respectively. The effective potential difference is therefore given by

$$\mu_{\mathrm{G}} - \mu_{\mathrm{M}} = |e|V_{\mathrm{TG}} = E_{\mathrm{F}} + \frac{|e|^2 n_{\mathrm{s}}}{\epsilon\epsilon_0} d + \text{const.}, \tag{4.1}$$

where n_s is the charge carrier density in the graphene layer, d is the thickness of the dielectric layer and the constant term includes the work function difference of the two materials, which can be neglected for the analysis provided that it is gate voltage-independent. Differentiating Eq. (4.1) with respect to n_s gives an expression for the capacitance per unit area

$$\frac{1}{C/A} = \frac{d(|e|V_{TG})}{e^2 dn_s} = \frac{dE_F(n_s)}{e^2 dn_s} + \frac{d}{\epsilon\epsilon_0}, \tag{4.2}$$

where the second term on the right hand side can be identified as the inverse of the geometric capacitance per unit area C_g/A. The other term has the dimensions of a capacitance and is inversely proportional to the density of states $\mathcal{D}(E_F) = dn_s/dE_F$. The quantity $e^2\mathcal{D}(E_F)$ is the so-called quantum capacitance per unit area C_q/A [55] which describes an effective decrease of the total sample capacitance. Since it is connected in series to C_g the quantum capacitance will dominate the total capacitance if it takes values smaller than C_g.

4.2 Measurement setup

The temperature for all measurements was 1.7 K achieved in a variable temperature insert ^{4}He cryostat. For basic characterization of the device transport measurements using standard lock-in techniques were carried out in addition to the quantum capacitance measurements. For the latter the size of the expected signal was of the order of several fF and hence a high measurement resolution was required. Since frequencies can be measured with high accuracy we used an LC-circuit and recorded changes in its resonance frequency f_{res}. Fig. 4.1(c) shows the circuit model of our setup with the oscillator consisting of an inductor (L=100 μH) placed at room temperature in parallel to the setup capacitance C. The main contribution to C comes from the wiring of the cryostat with a capacitance $C_{cables} \approx 340$ pF for the coaxial cables. In parallel to this the series connection of C_g and C_q form the sample capacitance C_s.

During the measurements an oscillation amplitude of 20 mV was maintained in the resonator by an external drive. The resulting self-resonant frequencies were 850-900 kHz and the relative sensitivity for frequency changes was $\Delta f \approx 2.5\times10^{-7}$. Converted to capacitance changes an accuracy of the order of 170 aF was achievable with this setup.

4.3 Sample fabrication

Single layer graphene flakes were characterized and contacted with Cr/Au (2 nm/40 nm) as described in chapter 3.1. In contrast to the other experiments described in this thesis, the Si substrate was undoped however. Care was taken about this fact to exclude stray capacitances from the back gate which would falsify the measurements.

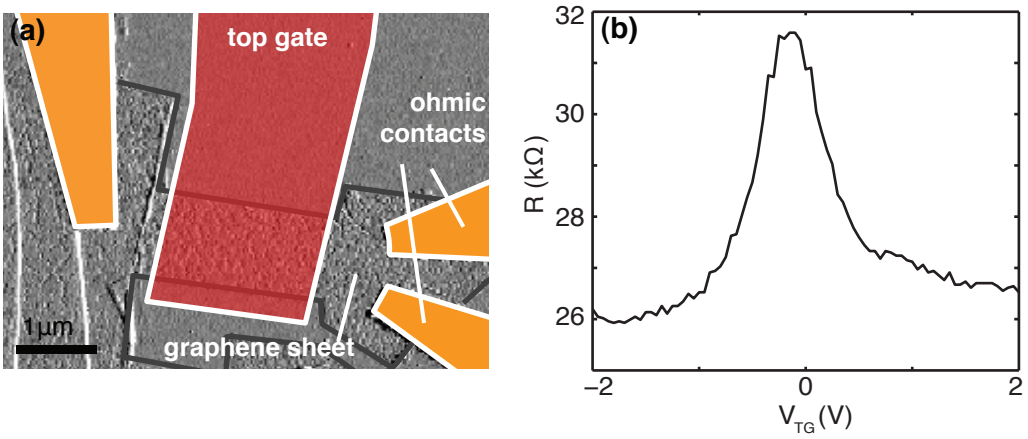

Figure 4.2: (a) Atomic force microscope (AFM) image of the device studied here. The electrodes are colored corresponding to the scheme in Fig. 4.1 (a). (b) Two-point resistance obtained in transport measurements with a constant current of $I = 1$ nA at a temperature of $T = 1.7$ K.

The graphene sheets were structured by the commonly applied dry etching technique called reactive ion etching (RIE). In this method a directed oxygen-argon plasma in the RIE chamber removes the graphene in the regions laid open in another EBL step. After removal of the remaining resist, the desired structure is left behind in the graphene sheet.

A patterned top gate was deposited after a third electron beam lithography step. As a dielectric for the top gate we used dense Al_2O_3 thin film, which was obtained in cycles of depositing 1 nm of aluminum followed by a 3 min period of increased oxygen pressure in the deposition chamber leading to the complete oxidation of the thin Al-film. The resulting oxide thickness after four such cycles was approximately 12 nm. Deposition of Ti/Au (5 nm/50 nm) in the same evaporation chamber formed the top gate electrode. Fig. 4.2 (a) displays an AFM image of the device measured for this work.

4.4 Experimental observations and discussion

Figure 4.2 (b) shows a two-terminal transport measurement taken with a current bias of 1 nA. The Dirac point is visible as a resistance maximum and only slightly shifted away from zero top gate voltage. Since we do not know the precise thickness and the dielectric constant of the aluminum oxide we can only estimate the geometric capacitance of the top gate to be $C_g \approx 6$ fF/μm^2. Using this estimate a mobility of 2000-3000 cm^2/Vs is extracted for the device.

The change in resonance frequency f_{res} as a function of applied top gate voltage

V_{TG} is displayed in Fig. 4.3 (a). A maximum is observed close to zero gate voltage which coincides with the maximum in the transport curve (Fig. 4.2 (b)) and therefore marks the Dirac point. At high charge carrier densities, the resonance frequency reaches a constant value indicating the dominant influence of the cable capacitance. We are interested in the relative change of f_{res} and therefore define the magnitude $\delta_{\mathrm{m}} \equiv \Delta f(V_{\mathrm{TG}})/f_0$ with f_0 being the voltage independent background frequency (see right scale in Fig. 4.3 (a)).

To determine the changes in quantum capacitance from the frequency measurement the circuit diagram has to be considered. Far away from the Dirac point we expect C_{q} to be too large to affect the total capacitance which is hence given by $C_{\mathrm{cables}} + C_{\mathrm{g}}$ in this limit. The total capacitance of the equivalent circuit in Fig. 4.1 (d) can be written as

$$C(V_{\mathrm{TG}}) = C_{\mathrm{cables}} + C_{\mathrm{g}} - \left[C_{\mathrm{g}} - \left(\frac{1}{C_{\mathrm{g}}} + \frac{1}{C_{\mathrm{q}}} \right)^{-1} \right], \tag{4.3}$$

where the term outside the square brackets is constant at all top gate voltages and only the term inside is varying causing the change in capacitance $\Delta C(V_{\mathrm{TG}})$. This expression describing ΔC can be simplified to $C_{\mathrm{g}}^2/(C_{\mathrm{g}} + C_{\mathrm{q}})$.

The resonance condition of an LC-circuit $f_{\mathrm{res}} = 1/(2\pi\sqrt{LC(V_{\mathrm{TG}})})$ can be expanded for small variations ΔC of the capacitance yielding $\Delta C = -2(C_{\mathrm{cables}} + C_{\mathrm{g}})\Delta f/f_0$. Applying this relation to the frequency data yields the curve displayed in Fig. 4.3 (b). A minimum is visible at the charge neutrality point and an increase of ΔC with increasing density is observed. In this regime the quantum capacitance is dominating the signal. The transition to a constant capacitance value at large top gate voltages indicates that C_{q} is negligible beyond $\pm$ 1 V.

Combining the two expressions for ΔC relates the quantum capacitance to the cable capacitance, the geometric capacitance and the measured frequency

$$C_{\mathrm{q}} = C_{\mathrm{g}} \frac{\alpha - \delta_{\mathrm{m}}}{\delta_{\mathrm{m}}}, \tag{4.4}$$

where $\alpha = C_{\mathrm{g}}/2C_{\mathrm{cables}}$. This equation contains only experimental parameters and will later be used to deduce the density of states $\mathcal{D}(E) = C_{\mathrm{q}}(V_{\mathrm{TG}})/|e|^2$.

In order to extract the density of states as a function of the Fermi energy, the top gate voltage axis has to be transformed into energy. To avoid any a priori assumptions about the density of states we do not use the linear dispersion but start with the electrostatic configuration described by Eq. (4.1). The charge carrier density n_{s} is obtained from integrating the density of states $\mathcal{D}(E)$ over all energies between the Dirac point and the Fermi energy E_{F} and can be substituted to give

$$|e|V_{\mathrm{TG}} = E_{\mathrm{F}} + \frac{|e|^2}{\epsilon\epsilon_0} d \int_0^{E_{\mathrm{F}}} \mathcal{D}(E) dE. \tag{4.5}$$

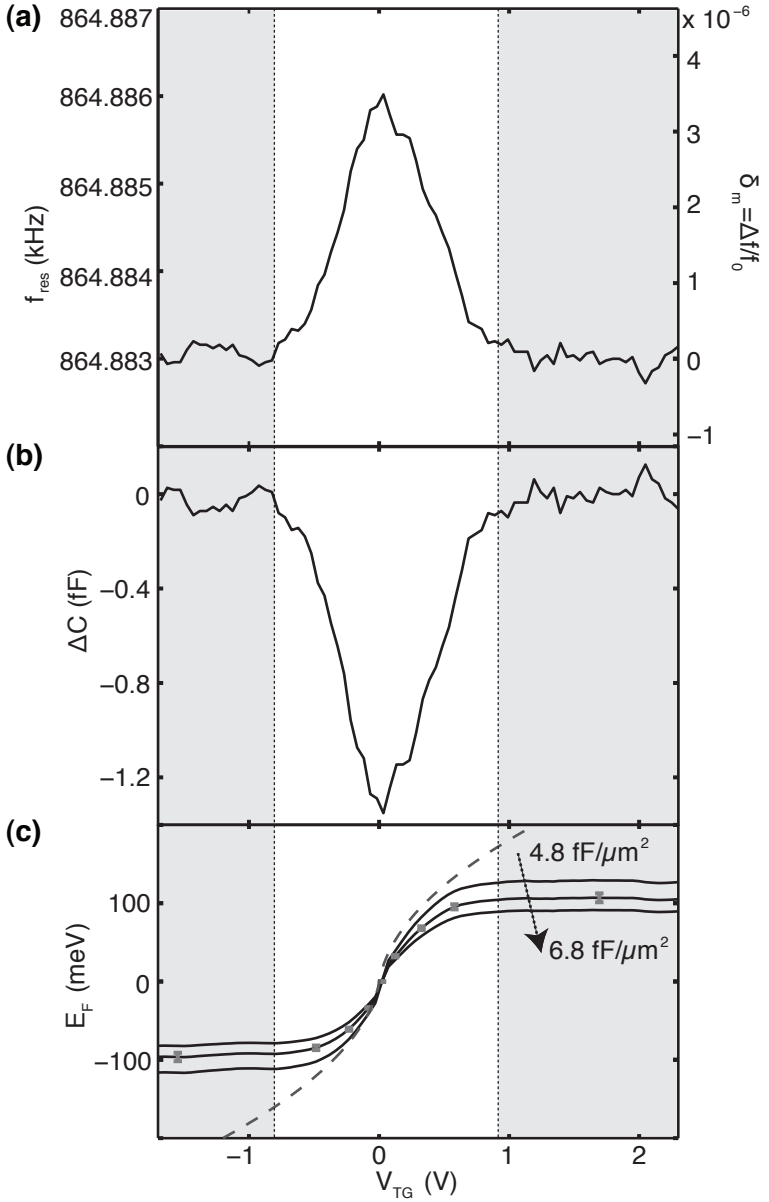

Figure 4.3: (a) Resonance frequency as a function of applied top gate voltage V_{TG}. (b) Determined change in total capacitance from frequency measurements. (c) Relation between Fermi energy and top gate voltage as deduced from eq. (4.7). The different curves (black lines) are obtained for varying values of C_{g} (from outermost to innermost curve: 4.8 fF/μm^2, 5.8 fF/μm^2, 6.8 fF/μm^2). The dashed curve shows the theoretically expected dependence for a perfectly clean graphene sheet. To compensate for the shift of the Dirac point towards negative voltages the horizontal axis in (a), (b) and (c) is offset by 0.3 V.

As shown above both the geometric capacitance C_g and the quantum capacitance C_q enter this expression. The change in Fermi energy for a given change in top gate voltage can hence be written as

$$\frac{\partial E_F}{\partial V_{TG}} = |e| \left[1 + \frac{C_q(V_{TG})}{C_g} \right]^{-1}. \tag{4.6}$$

The relation between the capacitances involved and the measured frequency identified before can be included into Eq. (4.6). An expression for the Fermi energy which depends on the applied top gate voltage is gained by integration over V_{TG}

$$E_F(V_{TG}) = \frac{|e|}{\alpha} \int_{V_D}^{V_{TG}} \delta_m(V'_{TG}) dV'_{TG}, \tag{4.7}$$

where V_D is the gate voltage at the Dirac point. Here the geometric capacitance is the only parameter our device does not allow us to determine from the data directly. We can however estimate it from the parallel plate capacitor geometry (as it has been done above to deduce the charge carrier mobility) to be $C_g \approx 6$ fF/μm^2. In addition to the ribbon device a bilayer Hall bar located on the same chip was used to determine the charge carrier density from Hall measurements. A geometric capacitance of $C_g \approx 5.8$ fF/μm^2 was obtained from this method. Since the two values are comparable the estimate for the free parameter C_g seems reasonable.

Eq. (4.7) can now be applied to the data assuming a specific C_g. In Fig. 4.3 (c) the obtained Fermi energy is plotted as a function of top gate voltage for three different values of C_g as well as for an ideal graphene sheet (dashed curve). As expected an increase of $|E_F|$ with increasing $|V_{TG}|$ is observed. This effect is strong at small voltages. The (unphysical) saturation at $|V_{TG}| > 1$ V indicated in Fig. 4.3 is due to the dominating cable capacitance. For all experimental curves the Fermi energy at a certain top gate voltage is below the theoretically expected value. As the noise in the frequency measurement leads to an error in the $E_F(V_{TG})$ relationship extracted from the measurement an error analysis is done. The accuracy is estimated assuming a Gaussian probability density distribution for the relative frequency change $\Delta f/f_0$. Its width is given by the variance of the noise in δ_m yielding σ=2.5×10^{-7}. The resulting error bars indicated in Fig. 4.3 (c) are small in comparison to the uncertainty given by the parameter C_g.

Equations (4.4) and (4.7) now allow us to convert the data in Fig. 4.3 (b) into a $\mathcal{D}(E_F)$ plot. The result is shown in Fig. 4.4 for different C_g between 4.8 fF/μm^2 and 6.8 fF/μm^2. For comparison the dashed line in Fig. 4.4 displays the theoretical density of states of perfectly clean graphene given by $\mathcal{D}(E_F) = 2E_F/\pi(v_F\hbar)^2$ [4]. Especially at low energies a large discrepancy is observed between experiment and theory. Instead of the linear increase starting at zero a nearly constant value of $\mathcal{D}(E_F) \approx 1\times10^{17}$ m^{-2}eV^{-1} is maintained in the interval between $E_F = \pm 50$ meV. An increase of the number of states towards higher energies is observed. However,

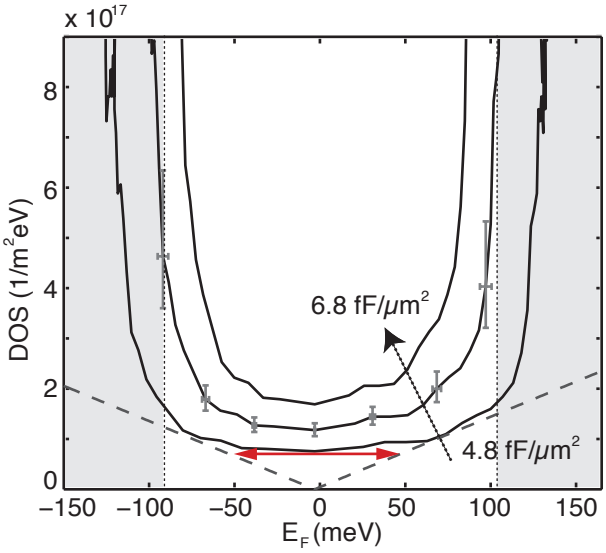

Figure 4.4: Density of states as a function of Fermi energy. The black solid lines show the experimental data assuming different geometric capacitance C_g (from outermost to innermost curve: 4.8 fF/μm^2, 5.8 fF/μm^2, 6.8 fF/μm^2). Error bars are indicated and the theoretically expected density of states for a perfectly clean graphene sheet is drawn as the dashed line. The bias window defined in Fig. 4.3 for the range in which C_g is dominating the total capacitance is plotted with dotted lines.

since the signal to noise ratio decreases rapidly as the measurement value is constant at high charge carrier densities, the errors in the extracted $\mathcal{D}(E_F)$ are getting very large outside the interval limited by the grey areas in Fig. 4.4. The full width at half maximum of the probability density function of $\mathcal{D}(E_F)$ was used to determine the error bars shown in the graph.

The observed non-zero density of states around the charge neutrality point indicates a finite number of states. This is conceivable in the presence of local potential fluctuations in the graphene sheet. From the flat portion of the density of states in Fig. 4.4 we can estimate a characteristic amplitude of the fluctuations of 100 meV. Comparing our results to transport measurements on graphene nanoribbons [58–62] and scanning tunneling electron transistor experiments [41] we find good agreement. As these samples were not covered with any dielectric unlike the sample used in our experiment we can infer that the gate oxide did not induce a large amount of additional disorder in our graphene device.

4.5 Conclusion

We have performed transport and capacitance measurements on a locally gated single-layer graphene sheet. With our measurement setup using a resonant circuit we could measure the capacitance with very high sensitivity. The density of states as a function of Fermi energy was determined from experimental data. As the main results we extracted a constant density of states $\mathcal{D}(E_F) \approx 1\times10^{17}$ m^{-2}eV^{-1} around the Dirac point and determined the size of the disorder potential to be ≈ 100 meV, which is comparable to other studies.

It has been shown recently that the reduction of the disorder fluctuations (e.g. by using different substrates [31, 63]) improves the quantum capacitance signal dramatically and even allows for the investigation of Landau level formation in capacitance measurements [44, 64, 65].

Chapter 5

Graphene nanoribbons - basic characterization

Narrow graphene constrictions are commonly used as tunneling barriers in nanoscale graphene devices. The transport properties of such graphene ribbons and constrictions on a SiO_2 substrate have been one of the puzzles for the understanding of graphene nanostructures. Theoretical predictions of an energy gap in ribbons [66–69] have triggered intense experimental [58–62, 70–75] and theoretical research [68, 76–87]. It has become evident experimentally, that localized states originating from edge and bulk disorder, suppress the conduction and lead to a transport gap [58–60] rather than a true band gap. In addition, experiments indicate the formation of an interaction driven Coulomb gap [58–62]. A wealth of theoretical ideas ranging from Anderson localization [79–83] to Coulomb blockade [77, 84] try to explain the phenomenology.

5.1 Theoretical background

5.1.1 Constrictions in conventional semiconductors

Nanostructures have been studied in semiconductors for the last decades. Often, heterostructures that contain a two-dimensional electron gas (2DEG) buried underneath the surface are used as the starting material. In order to confine charge carriers to even lower dimensions, metal electrodes are placed on the surface. By applying a negative voltage to these so-called split gates, the 2DEG below the gate area is depleted of charge carriers and hence becomes electrically insulating.

As displayed in Fig. 5.1 (a), a constriction is formed if only a small opening remains between two electrodes such that electrons have to pass this channel when crossing from one large reservoir to the other. Low-temperature transport measurements on such a gate geometry on top of a GaAs/AlGaAs heterostructure have been carried out in 1988 for the first time by two groups independently [88, 89]. The resistance recorded in these measurements was transformed into a conductance G,

which is shown in Fig. 5.1 (b) as a function of the applied split gate voltage V_G. Here, as an over-all tendency, the conductance increases as the gate voltage is made less negative. The intuitive explanation for this effect is that the depleted area is reduced as V_G is tuned to more positive voltages and the channel gets effectively wider, allowing more charge carriers to pass.

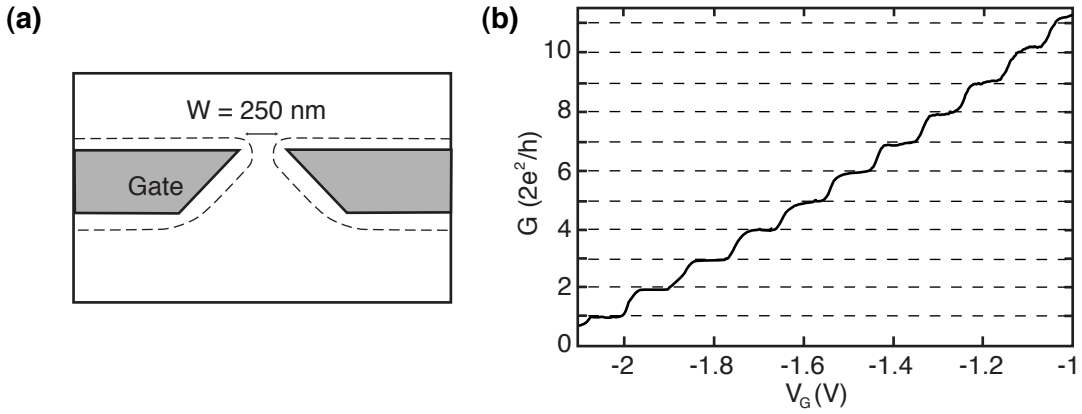

Figure 5.1: (a) Schematic of a split gate defined constriction in a semiconductor heterostructure as measured in Refs. 88 and 89. The 2DEG is depleted underneath the gates and the region above the gates is connected only via a narrow opening with the lower part. (b) Conductance G as a function of gate voltage V_G for a quantum point contact of width $W = 250$ nm. Conductance is obtained from inversion of measured resistance signal and the subtraction of a gate independent background resistance. (Figure reprinted from Ref. 88)

The more striking observation, however, is the appearance of conductance steps of equal height along the gate voltage axis. With each step the conductance increases by $\Delta G = 2e^2/h$ which equals twice the conductance quantum $G_0 = e^2/h$. The picture behind this experimental finding is that of discrete quantized states, called modes, propagating along the channel axis [90]. These are formed as a consequence of the lateral confinement normal to the direction of motion. Both the Fermi energies in the reservoirs and the width of the constriction determine the number of occupied modes. If a small bias voltage V_{bias} is applied between the two reservoirs the current carried by the modes traveling to the left and to the right, respectively, differs and a net current flows. Each of the occupied quantum states contributes a net current of $I = (e^2/h) \cdot V_{\text{bias}}$, meaning one conductance quantum G_0. In zero magnetic field, electron spin degeneracy leads to a conductance contribution of $2e^2/h$ per mode as seen in Fig. 5.1 (b).

The phenomenon discussed above is observed in experiment under the condition that the thermal energy $k_B T$ of charge carriers is smaller than the energy spacing between the transverse modes to resolve the discrete values of G. Additionally, the

channel width and the length have to be much smaller than the mean free path (ballistic regime) of the electrons and the Fermi wavelength has to be comparable to the channel width. In semiconductor heterostructures these requirements are typically met with the present sample quality. The device introduced in this section is usually referred to as a quantum point contact (QPC) since its transport properties are a result of the quantum mechanical wave character of the charge carriers.

5.1.2 Conductance in single layer graphene constrictions

The absence of a band gap in bulk graphene does not allow for the adaptation of the split gate technique in graphene, which is commonly used in semiconductors. In order to form a quasi one-dimensional transport channel in graphene, the material has to be cut into the desired geometry instead. In experiments, the propagation of electrons along the channel is very sensitive to edge disorder due to the absence of depletion effects near the edges. In this section a number of theoretical studies will be discussed which have carried out calculations considering different possible edge orientations and edge disorder in such ribbons.

Nanoribbons with ideal edges

Like for bulk graphene, tight-binding calculations were performed [66, 91–93] to determine the band structure for both clean armchair termination and zigzag termination of the ribbon edges as sketched in Fig. 5.2 (a) and (b). Fundamentally different characteristics were found depending on the edge type and the width of the ribbon. In Fig. 5.2 (c)-(f) the energy bands of the three distinct cases are shown. Armchair nanoribbons result in either a gapped band structure (Fig. 5.2 (c) and (e)) or a gapless metallic bandstructure (Fig. 5.2 (d)) depending on the number of dimer lines N across the ribbon width. The latter is found only under the condition that $N = 3m - 1$, with m being an integer, and leads to a degenerate zero energy state at $k = 0$. The size of the direct bandgap ΔE_c in semiconducting armchair ribbons decreases with $1/W$ as the ribbon is made wider [93]. For zigzag nanoribbons the dispersion exhibits a degeneracy of valence and conduction band at $k = \pi$ (Fig. 5.2 (f)). As the wave vector is diminished towards the center of the Brillouin zone these two bands continue to lie close to the Fermi level within the wave vector interval $\pi \geq |k| \geq 2\pi/3$ and show almost no dispersion.

The fact that in the armchair case neighboring atoms at the edges belong to different sublattices, whereas all edge atoms belong to the same sublattice in the zigzag case, is responsible for the observed difference in the band structure. Armchair edges include both A- and B-type atoms and hence the wave function needs to vanish on both sublattices at the edges to fulfill the boundary conditions. A zigzag edge on the other hand consists of only one sublattice, e.g. A-type on the top edge of Fig. 5.2 (b), allowing for a non-vanishing wave function on sublattice B. However, at the opposite side of the ribbon the wave function is required to be zero

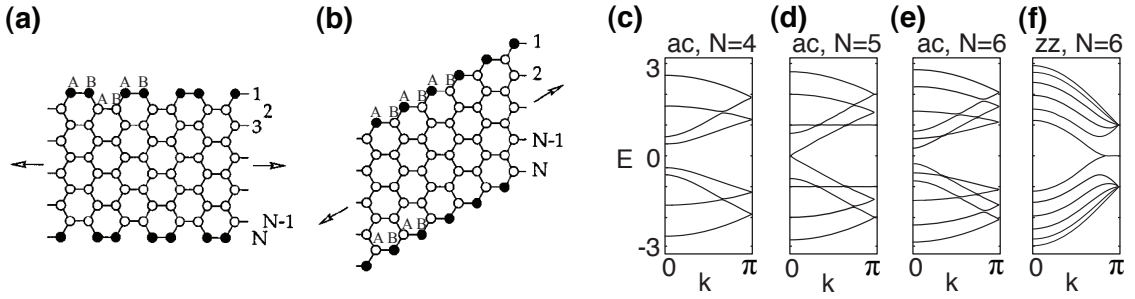

Figure 5.2: Lattice structure of (a) an armchair nanoribbon with $N = 10$ and (b) a zigzag nanoribbon $N = 5$. Definition of dimer number N is indicated and the sublattice assignment is marked. (c)-(f) Tight binding calculations of nanoribbon subbands for (c) $N = 3m - 2$ armchair, (d) $N = 3m - 1$ armchair, (d) $N = 3m$ armchair and (f) zigzag with $N = 6$. (Figure reprinted from Ref. 66)

on the B sublattice. The two dispersionless states at finite k-values originate from this asymmetry between the sublattices and appear as strongly localized electronic states at the edges of the zigzag ribbon.

In analogy to the one-dimensional wires formed in semiconductor heterostructures, a quantization of the transverse modes is present in ideal graphene nanoribbons as well. A fundamental variation of the phenomenology is however the symmetry of the quantized spectrum around the Fermi energy. According to the differing subband structure, the edge configuration results in characteristic quantization sequences for the three different cases [67, 94, 95]. For semiconducting armchair ribbons a quantization in steps of even multiples of G_0, namely 0, 2, 4, 6....$\times e^2/h$, is predicted. In the metallic case, the mode at zero energy is already two-fold degenerate and hence the conductance at zero energy is $2e^2/h$ and increases in steps of $2{\cdot}G_0$ as the energy is tuned away from the charge neutrality point. Here, only a factor of two for the spins is considered for the quantization since the ideal armchair edge leads to a lifting of the valley degeneracy [67, 94, 95]. For perfect zigzag edges in contrast, the valley degeneracy is expected to be maintained and a sequence of 2, 6, 10, 14....$\times e^2/h$ is obtained for the conductance.

Extension to disordered edges

So far, only nearest neighbor hopping was considered within a tight-binding band structure model, and any disorder was excluded from the discussion. Taking disorder effects into account, however, induces distinct changes to the results obtained above.

Armchair ribbons, which have a metallic band structure for certain widths in the ideal picture, are found to exhibit a bandgap of several 10 meV. This is obtained by the inclusion of next nearest neighbor hopping and a contraction of the bonds between the edge atoms by 3.5% [96]. Similarly, a bandgap is opened in zigzag

nanoribbons. Here, the reason is a magnetic ordering at the edges with opposite spin polarization on the two sublattices, which originates from on-site repulsion between the states at the Fermi level. This exchange potential difference on the two sublattices moves the previously flat bands, that were lying close to the Fermi level, away from each other. Hence, a small but finite band gap is predicted for all nanoribbons with pure armchair [93, 96] or zigzag [66, 92, 96] edge termination. For 20 nm wide ribbons, band gap values of 10 meV $\leq E_c \leq$ 70 meV should hence be achievable according to these calculations.

In order to resemble realistic devices more closely, ribbons consisting of both armchair and zigzag sections have been investigated [66]. Remarkably, the flat bands of the zigzag termination are extremely robust to the inclusion of armchair sites meaning that edge states are present even in ribbons having only few zigzag sites incorporated in the edges. While these electronic states are delocalized along the edge in pure zigzag ribbons, they get more and more localized as armchair fragments interrupt the zigzag termination.

As a consequence of disorder (at the edges) and the accompanying change in the density of states the formation of subbands is getting less pronounced. Conductance quantization is therefore no longer expected to be observable.

All theoretical studies show a significant deviation of the electronic properties from the ideal case if the edges are assumed to be slightly imperfect. In to date realistic devices, however, disorder is expected to be present both at the edges and in the bulk of the system. How this affects the transport properties is going to be subject of the following sections.

5.2 Sample fabrication and measurement setup

In order to get close to the device dimensions investigated in theoretical studies, two-dimensional graphene sheets have to be patterned into narrow ribbons, which then act as transport channels for the charge carriers. After the standard mechanical exfoliation and subsequent identification of single layer graphene flakes by atomic force microscopy and Raman spectroscopy [29, 97], the flake is electrically contacted as described in chapter 3.1. The created metallic fingers are needed as contacts for all electronic transport measurements discussed in this chapter. As a last step, the nanoribbons were defined in a resist mask during an EBL step. Subsequent RIE-etching (see chapter 4.3 for more details) and removal of the PMMA left behind the desired nanostructures. Atomic force micrographs of the single layer graphene nanoribbons measured in this chapter are displayed in Fig. 5.3.

All data was recorded in a variable temperature insert (VTI) at temperature between 1.25 K and 1.7 K. For all conductance measurements standard lock-in techniques were applied at frequencies well below 100 Hz.

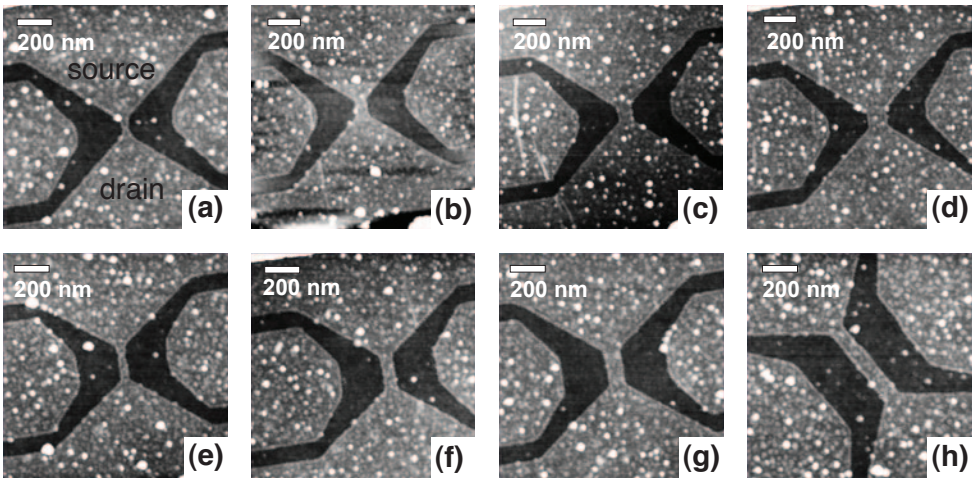

Figure 5.3: AFM images of the single layer graphene constrictions measured in this chapter. Graphene remained in the light grey areas whereas in the dark areas the substrate is visible. The channel is formed between the source and drain reservoir. The dimensions of the nanoribbons are given in the following by length × width: (a) 100 nm × 45 nm, (b) 100 nm × 80 nm, (c) 100 nm × 100 nm, (d) 100 nm × 122 nm, (e) 200 nm × 55 nm, (f) 200 nm × 75 nm, (g) 200 nm × 98 nm and (h) 500 nm × 98 nm.

5.3 Experimental observations and microscopic pictures

5.3.1 Dependence of transport on the charge carrier density

In order to change the charge carrier density in the graphene sheet, a voltage is applied to the highly doped Si substrate, which acts as a global back gate. Fig. 5.4 shows a typical low-temperature ($T \approx 1.25$ K) gate voltage dependence of the conductance through a graphene nanoribbon with a width of 75 nm and a length of 200 nm. By sweeping the back gate voltage V_{BG} from negative to positive values, the Fermi energy is tuned from the valence band through the charge neutrality point into the conduction band as is visualized by the sketched Dirac cones in Fig. 5.4. In these two regimes, transport can therefore be described as being hole-like and electron-like, respectively.

In contrast to transport data taken for bulk graphene, here, a region of strongly suppressed conductance is observed in the vicinity of the charge neutrality point around $V_{\mathrm{BG}} = -2$ V. In this regime, the measured conductance values drop considerably below e^2/h (dashed line in Fig. 5.4) indicating that the system is strongly localized [98]. However, the formation of a band gap cannot explain this feature.

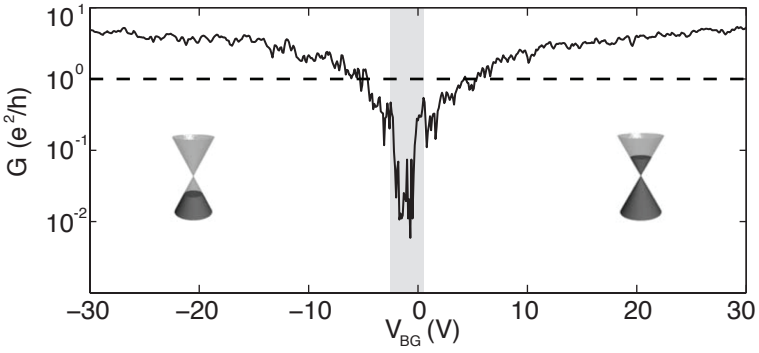

Figure 5.4: Conductance G as a function of applied back gate voltage V_{BG}. The data shown was measured for a constriction with length $L = 200$ nm and width $W = 75$ nm at a temperature of $T = 1.25$ K. A DC bias voltage $V_{\mathrm{bias}} = 500$ μV was applied and the conductance was recorded using standard lock-in techniques at a frequency of 13 Hz and an AC bias modulation of $V_{\mathrm{mod}} = 50$ μV. The shaded region indicates the range of the transport gap ΔV_{BG} and the dotted curve marks the value of the conductance quantum e^2/h.

The expected size of a band gap E_{c} for an ideal ribbon of the given dimensions is much smaller than the large change of Fermi energy ΔE_{F} necessary to overcome the region of conductance suppression ΔV_{BG} in the present measurement. Since current flow is strongly inhibited throughout ΔV_{BG}, it is commonly called the "transport gap" in the literature.

Additionally, the curve exhibits strong conductance fluctuations at low charge carrier densities that get smaller as the charge carrier density is increased. Similar features have been observed in measurements of narrow disordered channels in Si-inversion layers [99] where they were explained by hopping transport between strongly localized states caused by the structure of the underlying density of states.

A comparison of the gate voltage dependence for a narrow channel formed in a two-dimensional electron gas as plotted in Fig. 5.1 (b), and the corresponding measurement of a graphene nanoribbon in Fig. 5.4, illustrates the absence of conductance quantization in the latter. This observation does not come as a surprise since, as discussed in Sec. 5.1.2, the presence of disorder at the edges results in the disappearance of discrete plateaus in the conductance trace. Due to the top-down fabrication applied here, it is not possible to control the edge termination on the atomic scale as would be necessary to observe the theoretical predictions of quantized conductance.

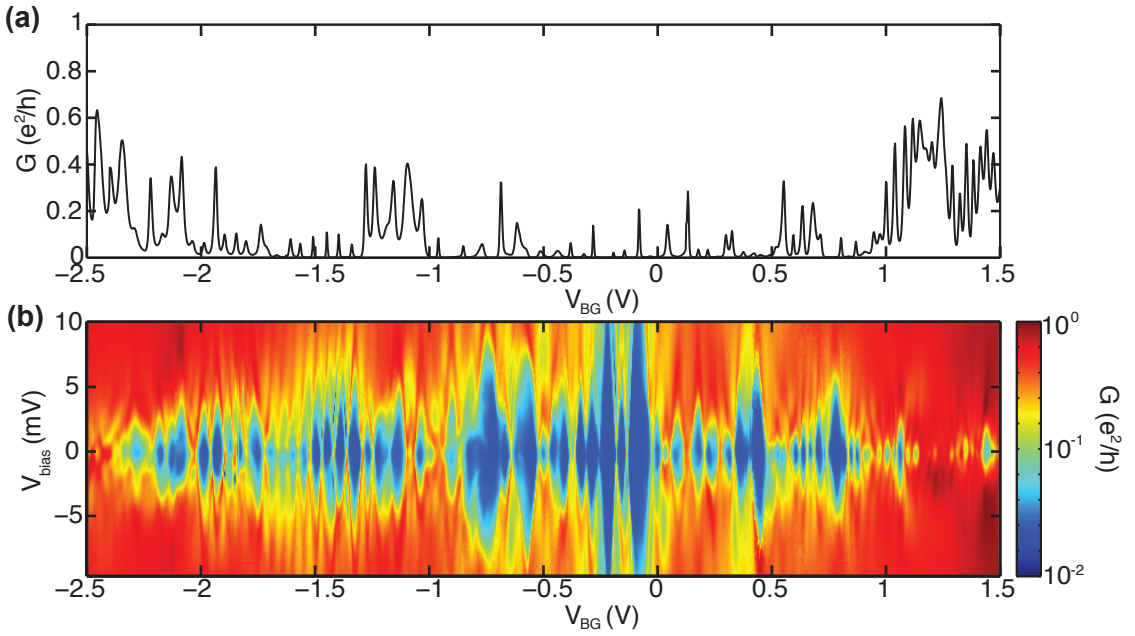

Figure 5.5: (a) Close-up of conductance spectrum as a function of back gate voltage inside transport gap (grey shaded region in Fig. 5.4) taken with an applied voltage bias $V_{\text{bias}} = 100\ \mu$V. (b) Finite bias measurement of same back gate range as in (a) showing Coulomb blockade diamonds. Both measurements were obtained with the nanoribbon shown in Fig. 5.3 (f) with $L = 200$ nm and $W = 75$ nm at a temperature of $T = 1.25$ K with lock-in techniques.

5.3.2 Dependence of transport on the applied voltage bias

It proves helpful to look into the transport characteristics around the charge neutrality point in more detail. A zoom into the transport gap is shown in Fig. 5.5 (a) where a large number of conductance resonances show up as a function of back gate voltage. In between these peaks the conductance is close to zero. If we associate with each conductance resonance the addition of a single electron to the system, the transport gap corresponds to a density of states of $\approx 5\times10^{16}$ m^{-2}eV^{-1}. This value is in good agreement with the result of chapter 4, where the density of states was determined from the quantum capacitance of a top gated large-area device. A similar behavior is known from systems in the Coulomb blockade regime as e.g. a single electron transistor (SET) or a single quantum dot (QD) [57].

In such devices a chargeable island is coupled to a source and a drain contact via two tunneling barriers. Due to the size confinement of this island and the Coulomb interaction, the available additional energy levels take discrete values with spacing E_{add}. Figure 5.6 (a)-(c) shows a sketch of the arrangement. Additionally, a finite bias can be applied across the structure inducing a difference in the electrochemical

potentials of the source and drain. If an energy level of the island lies within this window, as visualized in Fig. 5.6 (a), transport is possible and a peak in the conductance is observed. If, on the other hand, no level is located inside the bias window (see Fig. 5.6 (b) and (c)), current flow is not allowed, resulting in zero conductance - the Coulomb blockade. In order to tune the system into or out of the blockaded regime, one can either shift the discrete energy levels by applying a gate voltage or change the size of the bias window. In a measurement where both the applied bias and gate voltage are changed, diamond-like features of suppressed conductance are observable which are commonly referred to as Coulomb blockade diamonds. As indicated in Fig. 5.6 (d), the size of these diamonds in the bias direction directly resembles the energy $E_{\mathrm{add}} = |e|V_{\mathrm{bias}}$ needed to add one more electron to the island. The addition energy E_{add} is composed of the charging energy $E_{\mathrm{c}} = e^2/C$, where C is the capacitance of the island, and the single-particle level spacing Δ_{s}. For large islands, the contribution of Δ_{s} is negligible and hence $E_{\mathrm{add}} \approx E_{\mathrm{c}}$. Since the charging energy is related to the capacitance of the island, it is possible to extract information about the size of the SET.

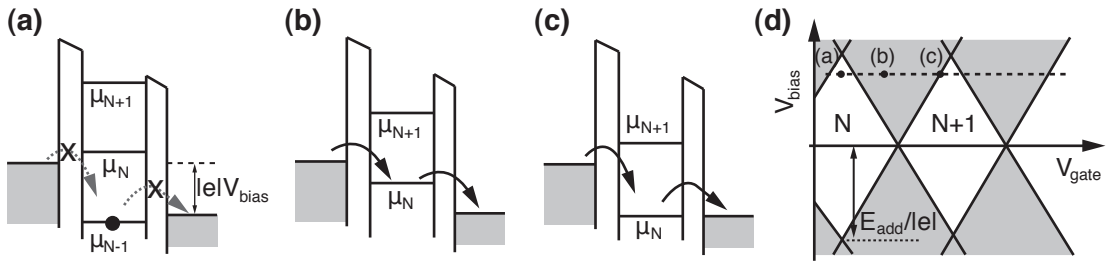

Figure 5.6: (a)-(c) Energy diagram of a single electron transistor or single quantum dot. Tunneling barriers separate the island from the leads. The island contains discrete energy levels at electrochemical potential μ_N and μ_{N+1} that can be shifted to lower energies by increasing an applied gate voltage V_{gate} as done from (a) to (c). The electrochemical potentials of source and drain reservoir are offset by the bias voltage V_{bias}. (d) Charge stability diagram (V_{bias} vs. V_{gate}) showing regions of suppressed transport in white and regions where transport is allowed in grey. (Figure adapted from Ref. 8)

Figure 5.5 (b) depicts the result of finite-bias spectroscopy for the graphene nanoribbon introduced in this section. Strikingly, a large number of Coulomb diamonds is obtained similar to the ones expected for an SET. However, in contrast to the rhombi sketched in Fig. 5.6 (d), which touch each other in discrete points along the gate-axis and are equal in size, in some regions the measured diamonds overlap with each other and show a large variance of their extent in the bias direction. Such characteristics have been observed in devices consisting of several islands, which all contribute to transport [100]. Due to the random gate dependence of charge carrier

transfer through such a system as well as the randomly varying magnitude of the charging energy E_c, this phenomenology is called stochastic Coulomb blockade.

The described observations evoke the assumption that several localized islands are formed inside the narrow ribbon. For some back gate voltage ranges, only one of these dominates charge transfer and the characteristics of transport through a single island is obtained (e.g. around -1.5 V in Fig. 5.5 (b)). In other voltage ranges multiple islands contribute to the measured conductance. It is important to notice that in the devices studied so far [58–62, 70–74, 101, 102] no self averaging is present, meaning that the number of localized sites is rather small. As a consequence the charging of individual islands is detectable in a finite-bias measurement by resolving Coulomb diamonds.

5.3.3 Microscopic pictures

Differing models have been put forward to explain the origin of the transport gap and the observed conductance resonances - a model based on Anderson localization and another based on Coulomb blockade effects in a series of charged islands along the ribbon. Both assume a considerable influence of disorder at the edges and/or in the bulk. While the former originates from the etching process, which results in rough edges, the latter is induced by surface or trapped charges in the substrate or by organic residues of the fabrication lying on top of the graphene sheet. Both types of disorder are hence inherent for the devices discussed here. It should be mentioned that in recent studies on large graphene flakes [31, 63] the SiO_2 substrate has been replaced by hexagonal boron nitride (BN). Due to its crystal structure, BN induces considerably less bulk disorder to the graphene sheets and hence reduces the influence of the substrate. In nanostructures, however, the edge-bulk ratio is significantly increased compared to that of large flakes. To date, experiments on nanostructures fabricated on BN substrate remain to be carried out. These will show how strongly the edge disorder induced by etching influences the transmission through graphene nanostructures and possibly clarify the microscopic picture behind electronic transport in these systems. In this section we discuss models that are suggested to explain the experimental findings made in nanostructures supported by SiO_2.

The picture of Anderson localization is generally used to describe the influence of disorder on electronic transport. In graphene nanoribbons non-perfect edge termination results in the formation of strongly localized low energy edge states as argued in Sec. 5.1.2, resulting in the suppression of current flow. The localization length is increased, however, as the absolute value of the Fermi energy is raised from zero [78]. When the localization length exceeds the system length, transport is no longer hindered and the transport gap ΔV_{BG} is overcome. In the language of Anderson localization, this transition is termed "mobility edge". Additionally, the localized states lead to an enhanced density of states (DOS) around the charge neutrality point. Calculations have shown that correlated with the large local DOS

at the boundaries there is a reduced DOS in the bulk of the nanoribbon [78, 81]. This may - for large edge defect concentrations - span the complete ribbon width and induce a barrier for charge transport [81] leaving localized islands behind. The diameter of such an island is expected to be comparable to the ribbon width [84], in agreement with size estimates from Coulomb diamonds. Hence, the origin of the two identified energy scales ΔV_{BG} and E_{c} can be accounted for using the Anderson model.

A competing explanation involves the formation of localized islands as a consequence of bulk disorder combined with a small energy gap. Due to the disorder potential a two-dimensional graphene sheet consists of electron-hole puddles [41] close to the charge neutrality point. In large area samples charge carriers can be transferred from one puddle to another without energy expense via Klein tunneling. If a ribbon of only some nanometers width is considered, on the other hand, the confinement is predicted to open a small band gap [66, 92, 93, 96] and electron-electron interaction may additionally induce a Coulomb gap. The borders between adjacent puddles are hence no longer transparent but display real tunneling barriers. Much like in an SET, the particles have to pay a certain charging energy E_{c} to enter the puddle and Coulomb blockade is expected to occur in such a system. The size of the puddles depends on the spatial variation of the potential landscape. In this picture, the size of the transport gap ΔV_{BG} is given by the sum of the amplitude of the disorder potential and the size of the energy gap since transport is constricted as long as the Fermi level lies between the global minimum of the valence band and the global maximum of the conduction band.

Besides these two pictures, another model assumes electronic transport in disordered graphene to happen along percolating paths of constant energy [80]. Considering the presence of an energy gap in such a nanoribbon, the system is expected to undergo a two-dimensional metal-insulator transition [80].

The so far presented experimental transport data can be understood in all these frameworks relatively well leaving the exact microscopic mechanisms behind transport a question yet to be answered. To shine further light on this open issue, more experiments have been carried out which will be subject of discussion in chapter 6.

5.3.4 Geometry dependence

To get a better feeling for the meaning of the energy scales observed in transport spectroscopy, a large number of experiments were conducted on ribbons of varying geometries [59, 60, 62, 70–74, 101]. From these measurements, several empirical scaling laws could be extracted.

The first quantitative characterization of the transport gap was done by Han et al. [70]. By investigating the extent of the region of suppressed conductance ΔV_{BG} in the bias direction, they extracted a value for the size of the energy gap E_{c}. Figure 5.7 (a) displays finite-bias measurements for a nanoribbon of width $W \approx 100$ nm and length $L = 500$ nm and the dashed line indicates how E_{c} is commonly extracted

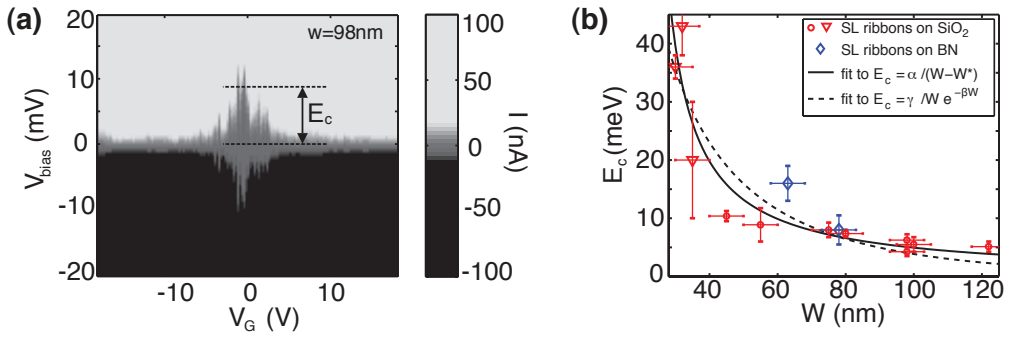

Figure 5.7: (a) Finite-bias spectroscopy for a 98 nm wide and 500 nm long nanoribbon. A region of suppressed current is visible. The characteristic energy E_c was extracted from the size in bias direction as indicated by the dashed line. (b) E_c as a function of ribbon width W. Three data points shown by red diamond markers, are taken from Ref. 59 to illustrate the trend for small widths. Fits according to the equations indicated in the graph were carried out to compare the experimental data with theoretical predictions. The error bars stem from the uncertainty in the AFM measurement when determining the diamater ($\Delta d = \pm$ 5 nm) and the variation in size of the Coulomb diamonds.

from such a conductance map. In the work presented here, eight nanoribbons on standard SiO_2 substrate (red circles in Fig. 5.7 (b)) and two constrictions lying on hexagonal BN (blue diamond markers in the figure) were investigated to find the width dependence of E_c. Plotting the determined values E_c as a function of width W yields the graph shown in Fig. 5.7 (b). It clearly shows that the two quantities are inversely proportional to each other. The data can be fitted well with the relation $E_c = \alpha/(W - W^*)$ with α being a scaling factor and W^* being the width of an inactive region at the edge of the ribbon. These two fitting parameters were found to take the values $\alpha = 0.40$ eV nm, in agreement with theoretical predictions [77] and experimental results [103], and $W^* = 20$ nm. Besides this empirical law, Sols et al. [77] explained the energy gap in their theory as a renormalized charging energy and derived the expression $E_c = \gamma/W e^{-\beta W}$, where γ and β are free parameters. Fitting the data with this relation leads to values of $\gamma = 1.65$ eV nm and $\beta = 0.015$ nm^{-1}. Both models describe the data well within the experimental precision and quantify how the transport gap can be tuned by the ribbon width in a remarkably wide range.

The data points for E_c in Fig. 5.7 (b) originate from nanoribbons of different lengths. Still they all follow the introduced scaling laws. This suggests that the length of the structures does not have a large influence on the size of the energy gap. However, the variety of lengths among the nanoribbons analyzed here (100 nm $\leq W \leq$ 500 nm) was not large enough to make a strong statement on the

correlation between system length and the characteristic energy scale E_c. To support the above supposition two works that carried out extensive experiments on the length-dependence will be mentioned shortly in the following.

A study investigating the size of the energy gap as a function of ribbon length L [74] obtained an almost constant E_c-value as the length of the constriction is changed. However, the minimum value of the averaged back gate dependent conductance G_{min} exhibits a strong length dependence. With increasing L the conductance value drops exponentially. This finding is consistent with the microscopic picture of transport being dominated by tunneling processes between localized charged islands.

Surprisingly, even for very short constrictions ($L \leq 60$ nm) localization takes place [60, 74]. Charge stability maps taken on such devices look very similar to those of intentionally designed quantum dots. Inside the Coulomb diamonds a number of co-tunneling lines are visible suggesting a rather strong coupling to the leads [74]. These systems might therefore be suitable to investigate the Kondo-effect in graphene and to observe Fano-resonances. Additionally, the limit of short constrictions is very interesting for the fabrication of more sophisticated devices since the occurrence of localization allows for their use as tunneling barriers in graphene nanostructures.

5.3.5 Bilayer graphene nanoribbons

Besides the study on single layer constrictions, six bilayer ribbons on SiO_2 substrate were investigated covering lengths L between 100 nm and 500 nm. As for single layer nanoribbons, for bilayer ribbons a transport gap is opened around the charge neutrality point. Within this gate voltage range, overlapping Coulomb diamonds appear in the finite-bias spectroscopy, thus exhibiting the finger print of stochastic Coulomb blockade. Since the over-all behavior is qualitatively similar to that of single layer graphene, a comparison of the characteristic energy scales may reveal differences.

Figure 5.8 displays the gap size E_c determined from the size of the Coulomb diamonds in bias direction using the method described in Fig. 5.7 (a). Indicated in grey are the single layer data points introduced in the previous section and the black traces show the previously carried out fits to this latter data set. The bilayer data is plotted in green.

As a general trend, a decay of the charging energy is observable as the structures get wider. The inverse dependence of the charging energy on the ribbon width is however not as pronounced as for the single layer ribbons. Additionally, the values of E_c are mostly larger than those determined for a single layer constriction of comparable width.

Applying the same technique as has been done for single layer constrictions in Ref. 59, we extract the extent of the transport gap in back gate voltage ΔV_{BG} as a function of width W for the single and bilayer ribbons investigated here. As is shown in Fig. 5.8 (b), the energy scale ΔV_{BG} is larger for narrower ribbons as well. Within

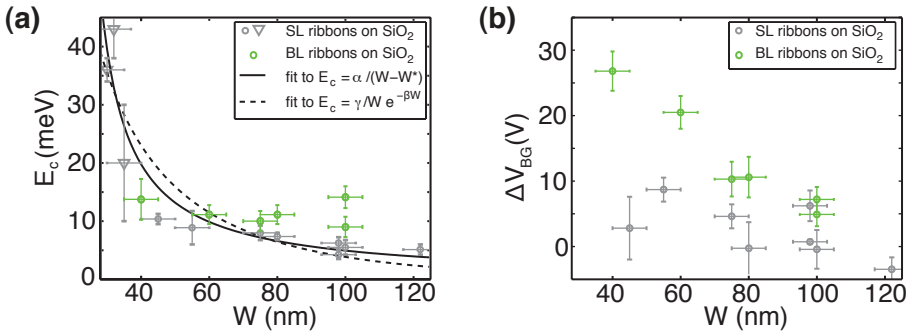

Figure 5.8: (a) E_c as a function of ribbon width W. The grey data points and the fits are the ones obtained from the single layer constriction (see Fig. 5.7 (b)). Green data is extracted for bilayer nanoribbons from Coulomb blockade diamonds. (b) Transport gap in back gate ΔV_{BG} as a function of W for single layer (grey dots) and bilayer (green dots) nanoribbons.

the investigated range of ribbon widths the dependence appears to be approximately linear. Like for the charging energy, the values of ΔV_{BG} are again higher for the bilayer constrictions than the ones determined for single layer ribbons.

According to the model introduced in the previous section, $E_c \propto 1/(W - W^*)$, the transport gap scales inversely with the ribbon width W. This width is corrected by a term W^* describing an area along the edges, which does not make a contribution to the measured conductance. An increased E_c may hence be the result of a wider inactive edge region for bilayer graphene. An explanation for such an increase of W^* may be provided by tight-binding calculations done for zigzag nanoribbons formed in bilayer graphene [104]. In this study the wave functions are found to get localized at the edges in zero energy states that extend over both layers. Since these states penetrate deeper into the bulk than edge states living on only one layer the conducting channel of the nanoribbon is effectively reduced.

On the other hand, both energy scales, E_c and ΔV_{BG}, characterize the potential fluctuations inside the graphene constriction and the fact that transport is blocked more efficiently for the bilayer graphene sample investigated here may indicated that the flake simply exhibits a stronger disorder potential than the single layer flakes studied earlier.

The bilayer constrictions measured here did not cover a large variety of aspect ratio and were all located on the same flake. A larger number of bilayer nanoribbons needs to be measured to further elucidate the influence of the number of layers on electronic transport in these narrow channels. From the data discussed here, no fundamental difference between single layer and bilayer graphene is apparent, however.

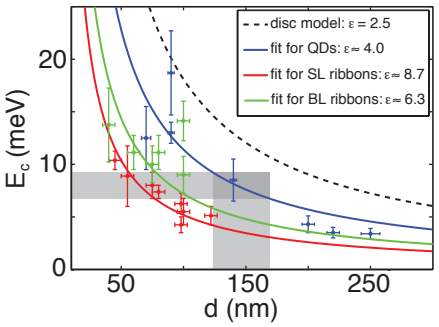

Figure 5.9: E_c vs. d for single QDs (blue dots) [11, 12, 105–108] and nanoribbons (red dots for SL, green dots for BL). Dashed line: Self capacitance of disc surrounded by SiO_2 and air. Solid lines: Fit to $E_c \propto 1/d$ of the respective data set to determine the effective dielectric constant ϵ.

5.3.6 Comparison of energy scales between nanoribbons and quantum dots

A rough estimate of the average size of the localized sites can be obtained from the charging energy extracted from the Coulomb diamonds utilizing a self capacitance model for a disc [57]. In Fig. 5.9 data from single quantum dots as well as from nanoribbons are presented.

For the QDs (blue data points in Fig. 5.9) the charging energy was received from the largest Coulomb blockade diamond. The size of the island could be determined from AFM measurements with an accuracy of $\pm$ 5 nm. The resulting plot of E_c vs. the dot diameter d suggests an inverse proportionality between these two parameters. An estimate of the energy needed to add an extra electron to such a disc is given by the capacitive charging energy $E_c = e^2/C_\Sigma$. Since the island can be described as a metallic disc of diameter d which is surrounded by a dielectric material with relative permittivity ϵ, the self capacitance $C_{\text{disc}} = 4\epsilon\epsilon_0 d$ is providing the lower limit for the total capacitance C_Σ.

As a first assumption for the dielectric constant $\epsilon = 2.5$, an average between the value for SiO_2 and air is taken (dashed line in Fig. 5.9). This value, however, gives a clear overestimation of the measured energy values and a fit to $E_c = e^2/4\epsilon\epsilon_0 d$ results in a considerably higher relative permittivity $\epsilon_{\text{QD}} \approx 4.0$. The observed discrepancy can be explained by the enhanced effective capacitance of the island due to the nearby graphene leads, surrounding gates and metallic contacts.

Next we apply this model to the nanoribbon device introduced in Sec. 5.3 (grey shaded area in Fig. 5.9). The size of the Coulomb diamonds in Fig. 5.5 indicate charging energies E_c between 7 meV and 9 meV. Hence, a diameter of 125 nm $\leq d \leq$ 170 nm would be expected for the localizations in the nanoribbon. Since the device is only 75 nm wide this seems unphysical and we assume the ribbon's width to set the upper boundary for the localization diameter. Other devices yielded similar results [58–62, 70–74, 101, 102].

The red data points in Fig. 5.9 display the extracted E_c for the single layer nanoribbons measured in this work plotted as a function of the ribbon diameter. The observed E_c-d-dependence can still be described well within the disc model if the relative permittivity is increased to $\epsilon_{\text{SL-ribbon}} \approx 8.7$. Since the capacitive

coupling to neighboring localized islands is assumed to be large, this enhancement can be well explained.

For the bilayer nanoribbons (green data points in Fig. 5.9), the charging energy tends to be larger than for the single layer structures, as discussed in the previous section. This fact indicates a less strongly coupled environment and indeed the fitting to the $1/d$-model yields $\epsilon_{\mathrm{BL-ribbon}} \approx 6.3$, a value just in-between the obtained ϵ_{QD} and $\epsilon_{\mathrm{SL-ribbon}}$. Since the design (arrangement of metallic contacts and adjacent graphene areas) of the single layer and the bilayer nanoribbon devices is the same, the capacitive coupling to the surrounding should be comparable. The exhibited behavior may hence be due to a smaller intrinsic screening for bilayer manifesting itself in a lower self capacitance than found in single layer graphene.

This observation is compatible with the picture of zero energy states spanning across the ribbon introduced in Sec. 5.3.3. These originate from the boundaries and lead to a reduced DOS in the bulk. Since the penetration of such states is expected to be enhanced for bilayer graphene [104], puddles may be capacitively decoupled from each other more efficiently already for wider ribbons as compared to single layer devices.

Even though the self capacitance for these bilayer devices is lower than the one of single layer constrictions, a comparison to the QD-data shows that the width of the ribbon displays the upper boundary for the size of the localized islands as well.

5.4 Conclusion

In this chapter we have given a general review of the transport properties of etched graphene nanoribbons, which was found to be governed by Coulomb blockade effects. Several scaling laws for the different energy scales involved were presented. These lead to an estimate for the number of localized islands inside constrictions with relatively small aspect ratios ($L/W \lesssim 5$). In the present devices, the islands were found to extend across the total width of the ribbon and other devices yielded similar results [58–62, 70–74, 101, 102]. An arrangement of the islands in a quasi one-dimensional chain is hence likely and as a rule of thumb the number of charge puddles p can be approximated by the ratio between length and width $p \approx L/W$.

Chapter 6

Graphene nanoribbons - further experiments for more detailed understanding

6.1 Temperature dependence

The measurements covered in the previous chapter indicated that a number of localized charge puddles form spontaneously in graphene nanoribbons around the charge neutrality point. However, the mechanism behind transport in those devices was not yet discussed. Studying the temperature dependence of the conductance reveals activation processes for electronic transport inside the transport gap. [62, 73, 102]

In Fig. 6.1 (a) the conductance inside the transport gap is plotted for various temperatures between 1.25 K and 45 K. To obtain this temperature dependence of G, the investigated back gate voltage range was split into intervals of about 1 V as indicated in Fig. 6.1 (a) by the vertical dashed lines. In these sections G was measured at stepwise increasing temperatures between 1.25 and 45 K. In all sections it was verified that the low-temperature Coulomb peak spectra were identical before and after the thermal cycle.

The sharp conductance peak spectrum at the lowest temperatures gets washed out more and more as the temperature is increased. This is due to a large increase of the conductance in the Coulomb blockaded regions in-between resonances. For the conductance peaks, two distinct behaviors are observable. A number of peaks decrease in height as the temperature is raised, whereas the majority exhibit an ever larger amplitude as T is raised and get broadened at the same time. Hence, a rather smooth conductance curve is obtained for the highest temperature approaching a conductance value of e^2/h. the fact that even at the highest temperatures the conductance approaches but does not exceed one conductance quantum means that the system remains in the strongly localized regime.

Figure 6.1 (b) shows a close-up for Coulomb resonances with distinctly different behaviors. The amplitude of the left peak grows with T and the peak broadens

at the same time until it is finally swamped away by the rising background. The signature of the right peak is a maximum peak value of G at the lowest temperature which drops to a local minimum at intermediate temperatures and recovers as T is increased further. Such a behavior is found only for those ≈10 % of the resonances in the investigated back gate window, which are particularly sharp at low temperatures.

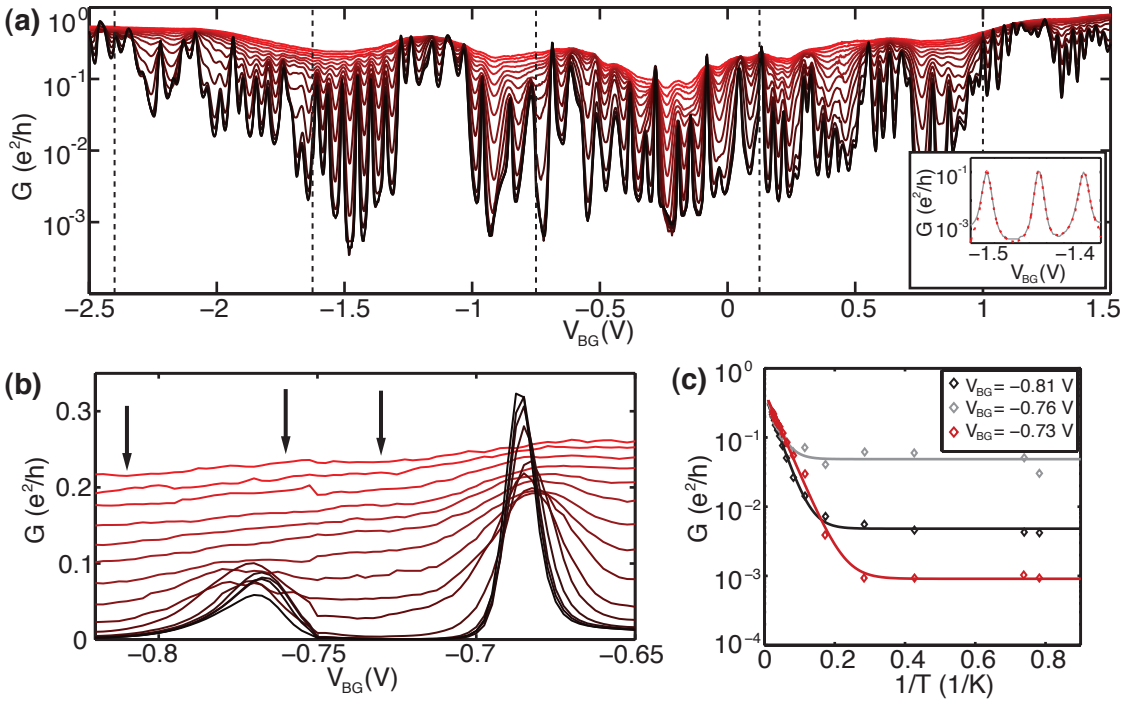

Figure 6.1: (a) T-dependence of G inside the transport gap at $V_{\mathrm{bias}} = 100\ \mu$V. Different curves are taken at T = 1.25 K to 45 K (black to red lines). Inset: Coulomb resonances (grey line) reconstructed by a convolution of three Lorentzians with the derivative of the Fermi distribution (red dotted line). (b) Zoom into two representative peaks of (a). The left peak is broadened and grows with increasing T and the amplitude of the right peak exhibits an overall decrease with temperature. (c) G as a function of $1/T$ at three positions in V_{BG} indicated by arrows in (b). Solid lines are fits to the data according to Eq. (6.1).

For single quantum dots, the evolution of the peak shape was explained by the contributions of temperature, single-particle level spacing Δ_{s} and coupling of the energy levels to the leads [109]. A $1/T$-dependence is expected for a strongly coupled ground state, as observed in Fig. 6.1 (a) (and for the right peak in Fig. 6.1 (b)) for peaks that are particularly sharp at the lowest temperatures. If, however, an excited state exhibits a stronger coupling to the leads than its ground state, a temperature increase will facilitate transport until, at $\Delta_{\mathrm{s}} \lesssim k_{\mathrm{B}}T$, both levels contribute to transport. The latter leads to the recorded amplitude increase and

the broadening of conductance peaks in Fig. 6.1 (a) (and for the left peak in Fig. 6.1 (b)).

The thermal activation of G in the conductance valleys gives insight into the transport mechanisms. Figure 6.1 (c) displays the conductance as a function of $1/T$ for three representative back gate values (marked with black arrows in Fig. 6.1 (b)). In this Arrhenius-type plot, the curves show a branch with a linear slope for the higher temperatures ($T \gtrsim 3\mathrm{K}$) and a branch with almost constant value of G at lower T. The activation above the threshold temperature is linked to the energy needed to induce transport through the system. Empirically, the data can be fitted to

$$G(T) = G_0 \exp\left(-\frac{E_\mathrm{a}}{k_\mathrm{B}T}\right) + G_\mathrm{off} \tag{6.1}$$

with the free parameters G_0 being a prefactor quantifying the high-T limit of G, E_a being the activation energy and G_off being a constant offset whose meaning will be discussed below. The solid lines in Fig. 6.1 (c) are the resulting fits and show that the data (diamond shaped markers in Fig. 6.1 (c)) can be reproduced very well with this empirical law.

A physical motivation for Eq. (6.1) is found by reproducing the peak shape of the Coulomb blockade resonances considering both thermal and coupling broadening as depicted in the inset of Fig. 6.1 (a). The width of the peaks is resembled well by the derivative of the Fermi function at a given temperature. A large discrepancy is found, however, for the tails of the peak where the thermal broadening underestimates the conductance considerably. In order to obtain higher values for the conductance away from the resonances, the Fermi function is convoluted with a Lorentzian distribution function. With this additional contribution the coupling of the energy levels to the leads is taken into account. The tail of the Lorentzian, and hence the constant G_off in Eq. (6.1) can be interpreted as describing cotunneling processes in the system at the lowest temperatures.

To motivate equation (6.1), the low-temperature limit of the Fermi distribution, $E_\mathrm{c} = 2E_\mathrm{a} \gg k_\mathrm{B}T$, has to be considered, which reads

$$\begin{aligned} \frac{df(E)}{dE} \propto G(T) &\propto \cosh^{-2}\left(\frac{E_\mathrm{a}}{2k_\mathrm{B}T}\right) \\ \Rightarrow \quad G(T) &\propto \exp\left(-\frac{E_\mathrm{a}}{k_\mathrm{B}T}\right). \end{aligned} \tag{6.2}$$

Note that the maximum activation energy E_a for transport is half the charging energy E_c describing the spacing between two energy levels of a localized island. The pre-factor, G_0, specifies the conductance value at high temperatures where the exponential term in Eq. (6.2) approaches unity. It contains contributions of various transport mechanisms which cannot be quantified easily. Finally, cotunneling of charge carriers results in a constant background, G_off, which has to be added to Eq. (6.2). Hence, the application of Eq. (6.1) for fitting the experimental data is well motivated.

The three fitting parameters E_a, G_0 and G_{off} can be determined for each back gate voltage to obtain their specific energy dependence. Meaningful values are obtained for those back gate values where G covers more than one order of magnitude as a function of T. The results are shown in Figs. 6.2 (a) and (b). Due to the given criterion for the analysis an evaluation at the edge of the transport gap as well as around V_{BG} = -1.25 V was not possible.

We start with discussing the high-temperature activated behavior found in the data. The activation energies $E_a(V_{BG})$ peak in the middle between neighboring conductance resonances (Fig. 6.2 (a)). On the other hand, pronounced dips in the activation energies arise which coincide with conductance peaks. In-between, a linear dependence on gate voltage is observed as is characteristic for Coulomb blockade diamonds. Additionally, the largest $2E_a$ values are 10 to 20 meV. This energy scale is of the order of typical charging energies E_c of this device determined from the finite-bias spectroscopy in Fig. 5.5. As visualized in Fig. 6.2 (c), a more careful comparison shows that the activation energy resembles the measured Coulomb diamond boundaries remarkably well. Due to thermal cycling in-between the diamond and the temperature measurement, some shifts are visible in the spectra if the two energy scales are plotted on top of each other over a large gate voltage range. The finding that the peak values of $2E_a$ in the valleys between conductance resonances are identical to the charging energy E_c extracted from Coulomb diamonds is a central result of this experiment.

We can reconstruct Coulomb diamonds from the activation energy by mirroring $E_a(V_{BG})$ at the voltage axis and inserting lines along the linear slopes in E_a. The insets of Fig. 6.2 (a) displays two qualitatively different regions in back gate voltage. In the left graph adjacent diamonds touch each other in one point at zero bias. Their size is similar and the flanks have the same slopes. For this back gate voltage range the same observations are made for the boundaries of Coulomb blockade diamonds measured in finite-bias spectroscopy. Such a behavior is characteristic for a single quantum dot where levels are filled sequently. In the region under discussion, transport is therefore dominated by only one localized island. Since the charging happens from the (temperature broadened) leads, that are coupled to the island, the corresponding maximum $2E_a$ and E_c have to be interpreted as the on-site charging energy of this localized site. Its diameter corresponds roughly to the ribbon width when estimating the size of the puddle from E_c by a comparison to data taken on quantum dots.

The temperature dependence of the conductance resonances between these diamonds exhibits a monotonic increase (see Fig. 6.1 (a)). As discussed before, this is expected for multilevel transport [109].

As a second regime we chose a back gate voltage in Fig. 5.5 around which the regions of suppressed current are connected to each other. The right inset in Fig. 6.2 (a) shows the corresponding reconstruction of Coulomb diamonds from E_a, where diamonds overlap and the size as well as the back gate dependence of E_a vary strongly in neighboring diamonds. Taking this behavior as an indication for the

participation of several dots in transport, we now have to attribute $2E_a$ and E_c to both on-site and inter-site charging energies. Stochastic Coulomb blockade describes such a phenomenon, where transmission through a small number of quantum dots is considered.

Next we proceed with a discussion of the low-temperature conductance represented by G_{off} in Eq. (6.1). As shown in the derivation of Eq. (6.2) we attribute G_{off} to cotunneling processes that determine the conductance value before thermal activation sets in. We can do a refined analysis of the low-temperature background by fitting the low-T data between resonances to the expression $G_{low} \propto \beta(T^2+T_0^2)$ [110]. We find that the data can be well described by this expression. Fig. 6.2 (b) shows that the conductance spectrum taken at the lowest temperature is indeed reflected by the extracted cotunneling background. The finding of cotunneling transport supports the previous statement that only few islands are involved in transport since cotunneling becomes suppressed as the number of localized states increases.

We now discuss the behavior of the prefactor G_0 in Eq. (6.1). It extrapolates the conductance for $k_BT \gg E_a$ and hence represents the high-temperature conductance. The order of magnitude of G_0 is between 0.1 and 1 in units of e^2/h. Similar to E_a it is strongly anti-correlated with the conductance at the lowest temperature as illustrated in Fig. 6.2 (b). The correlation between E_a and G_0 in conductance valleys is visualized in Fig. 6.2 (d). Clearly, the $G_0(E_a)$ plot consists of discrete branches with varying curvature/slope. Each color-coded branch corresponds to a peak of E_a in the back gate spectrum. The ratio of G_0 to E_a decreases as the pair originates from a back gate value closer to the center of the transport gap.

The picture of transport we present here does not require but does not exclude either the contribution of phonons inside the system. Activation may take place in the leads from which the localized puddles get charged via smearing of the Fermi function. It is unclear whether phonons in the ribbon get important for transport at elevated temperatures. The origin of the correlation between E_a and G_0 remains to be understood but may be linked to the role of phonons.

In summary, the interpretation of the finite-bias measurements presented in chapter 5.3.2 and the analysis of the thermal activation measurements arrive at the same conclusions: Charge transport in graphene nanoribbons is dominated by mainly one or a few puddles arranged in series. Although the details depend on the mesoscopic arrangements within the system, carrier transmission can be understood in a single-particle picture including Coulomb blockade effects.

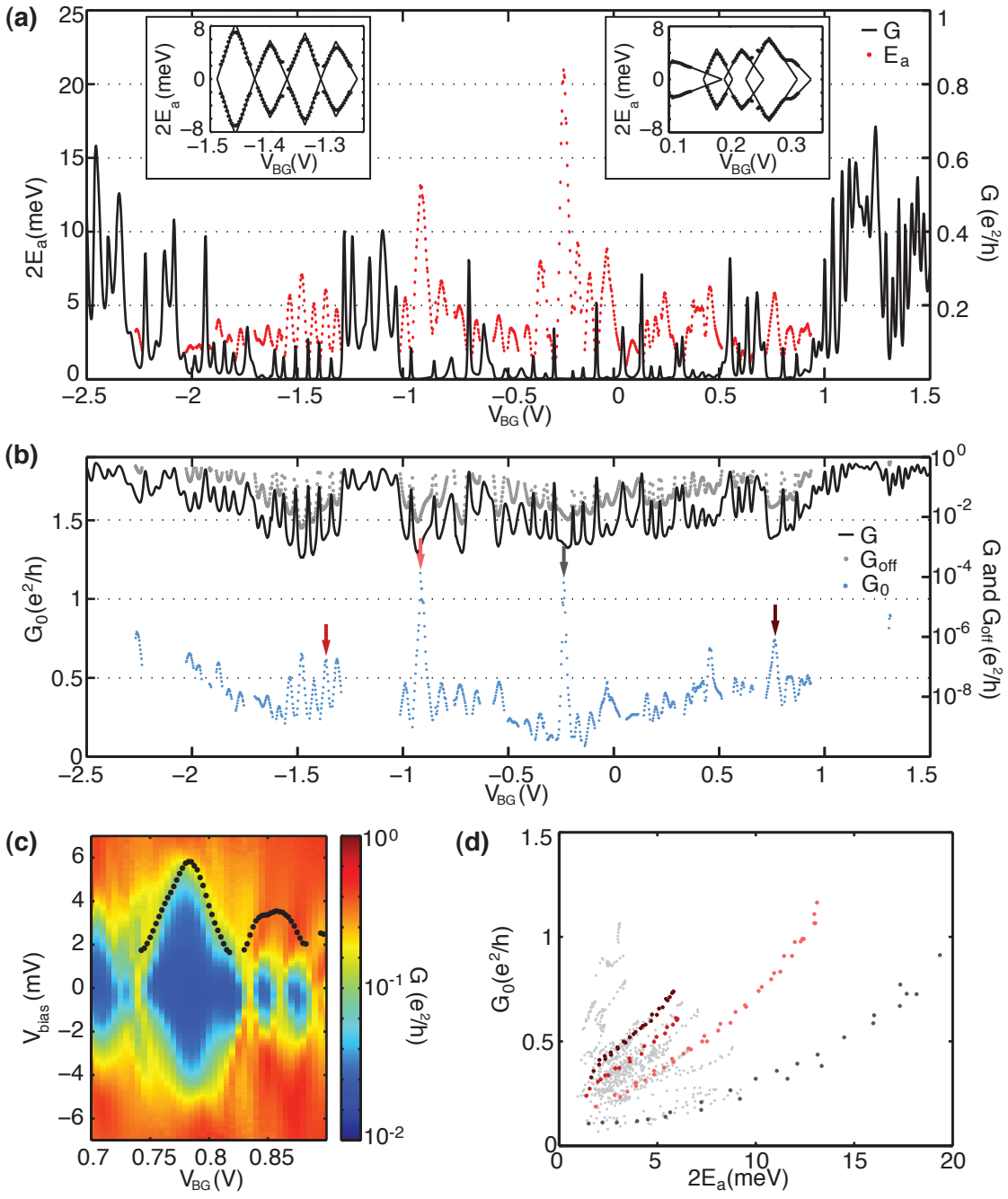

Figure 6.2: Back gate dependence of fitting parameters: (a) E_a, (b) G_{off} and G_0. In (a) and (b) the black solid curve shows G at base temperature. Insets: Coulomb diamonds reconstructed from E_a for two regimes. (c) Comparison of a Coulomb diamond (representing $E_c(V_{BG})$) and $2E_a$ determined for this V_{BG}-interval. (d) $G_0(E_a)$ for the transport gap. Colored branches indicate G_0/E_a pairs that originate from the same conductance valleys (arrows in (b)).

6.2 Magnetic field dependence

Studying an electronic system in the presence of a perpendicular magnetic field allows for the detailed understanding of its properties since the spatial extent of the electron wave function is changed as an external B-field is tuned. In a semi-classical picture, this is due to the propagation of charge carriers on cyclotron orbits of radius r_{cycl} if a Lorentz force acts on them. As a consequence, transport is mainly sensitive to potential fluctuations of certain length scales in the different regimes. Magneto transport in graphene nanoribbons was investigated to probe the effect of a magnetic field on the localized states inside the channel [73, 101].

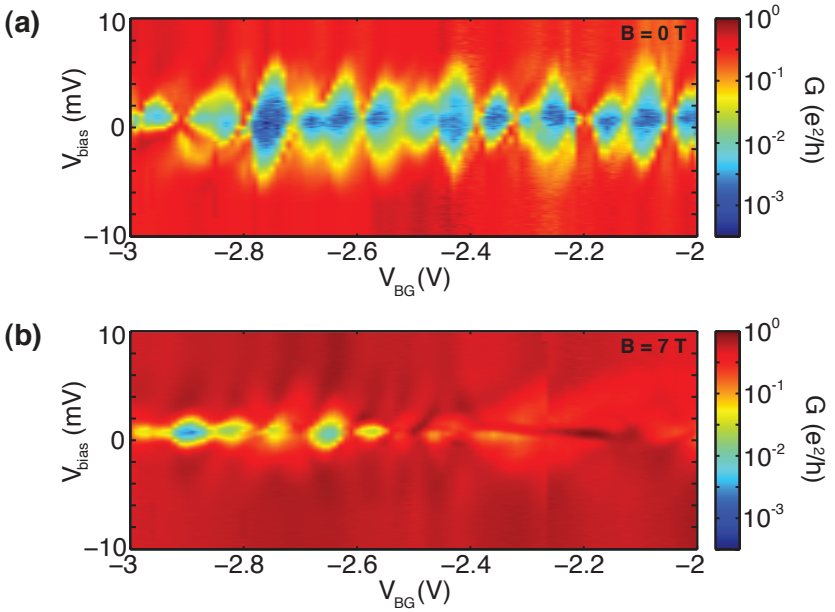

Figure 6.3: Differential conductance measurements as a function of source-drain bias and gate voltage at 0 T (a) and 7 T (b) showing the evolution of the diamonds of suppressed conductance with increasing magnetic field. The device had a width of 55 nm and a length of 200 nm and was measured at $T = 1.7$ K.

Figure 6.3 (a) and (b) show finite-bias measurements of a graphene nanoribbon of dimensions $W = 55$ nm and $L = 200$ nm at magnetic fields $B = 0$ T and 7 T. Coulomb blockade diamonds are visible, indicating the formation of charged islands inside the ribbon. As the magnetic field is ramped up, the size of these regions of suppressed conductance shrinks considerably and the over all conductance is enhanced.

Smaller Coulomb diamonds indicate a decrease of the charging energy E_c and therefore an increase in island size. In agreement with these findings, temperature dependent measurements [73, 102] in finite magnetic fields indicated that the energy

scale relevant for transport, namely E_a, shrinks as well if a finite magnetic field is applied. Furthermore, the transport gap is diminished since ΔV_{BG} is smaller at non-zero B-field.

To explain these observations, we compare the dimensions of the nanoribbon with the magnetic length $l_B = \sqrt{\hbar/eB}$. If the ribbon width is smaller than the cyclotron length $W \ll l_B$, the electron wave function extends across the whole width and hence transport is influenced by both edge and bulk disorder. For narrow channels this condition is fulfilled for low magnetic fields. As B gets larger the magnetic length falls below the system dimensions and the effect of both the quantum confinement and the edges becomes less relevant for transport [101]. Here, the magnetic length exceeds the ribbon size $W = 55$ nm by approximately 10 nm for a magnetic field of 1 T since $l_B \approx 65$ nm. In contrast, at the maximum field of $B = 7$ T the cyclotron length is $l_B \approx 25$ nm, meaning the orbit fits well inside the ribbon.

A contrary effect of the applied magnetic field is that the localization of the wave function leads to smaller wave function overlap and hence smaller tunneling coupling between neighboring puddles. As a consequence, the conductance is reduced as the magnetic field is increased.

The two contributions are therefore expected to compete in nanoribbons. In the data presented here in Fig. 6.3, the reduced backscattering appears to be dominating causing the increase of conductance. Following this observation, it is suggested [111–113], that such a system eventually undergoes a semiconductor-metal transition at high magnetic fields. The data presented in Fig. 6.3 are in good agreement with this explanation and imply that the ribbon width is a good estimate for the size of the localized states.

Following the reasoning of Ref. 73, the enhanced conductance originates from time reversal symmetry breaking in a finite magnetic field [114, 115]. The magnetic flux through the area occupied by a localized state has to be comparable to a flux quantum h/e in order to break time reversal symmetry. Measurements of the B-field dependent conductance allow one to extract a size estimate for the localized sites. The obtained value for the size of the localized states is again comparable to the ribbon width [73] and hence, magnetic field spectroscopy is providing yet more evidence for the spatial extent of the charged islands in graphene nanoribbons.

However, as noted in Ref. 73, Landau level quantization should be observable at high magnetic fields where $W \gg l_B$. Under these conditions, edge channels are expected to be formed each contributing to transport with e^2/h. Measurements on wide channels ($W \gtrsim 75$ nm) have indeed shown indications of conductance quantization (see Fig. 6.4). Conductance data for narrower ribbons, on the other hand, did not exhibit this feature. Possibly, scattering events between transport channels located at opposite edges, inhibit the transmission for narrow ribbons. As the edge channels are separated further for wider nanoribbons, scattering is less likely and Landau level formation may be recorded in conductance measurements.

An example for a device in which the required conditions are fulfilled is presented in the following. The nanoribbon was fabricated in a single layer graphene flake and

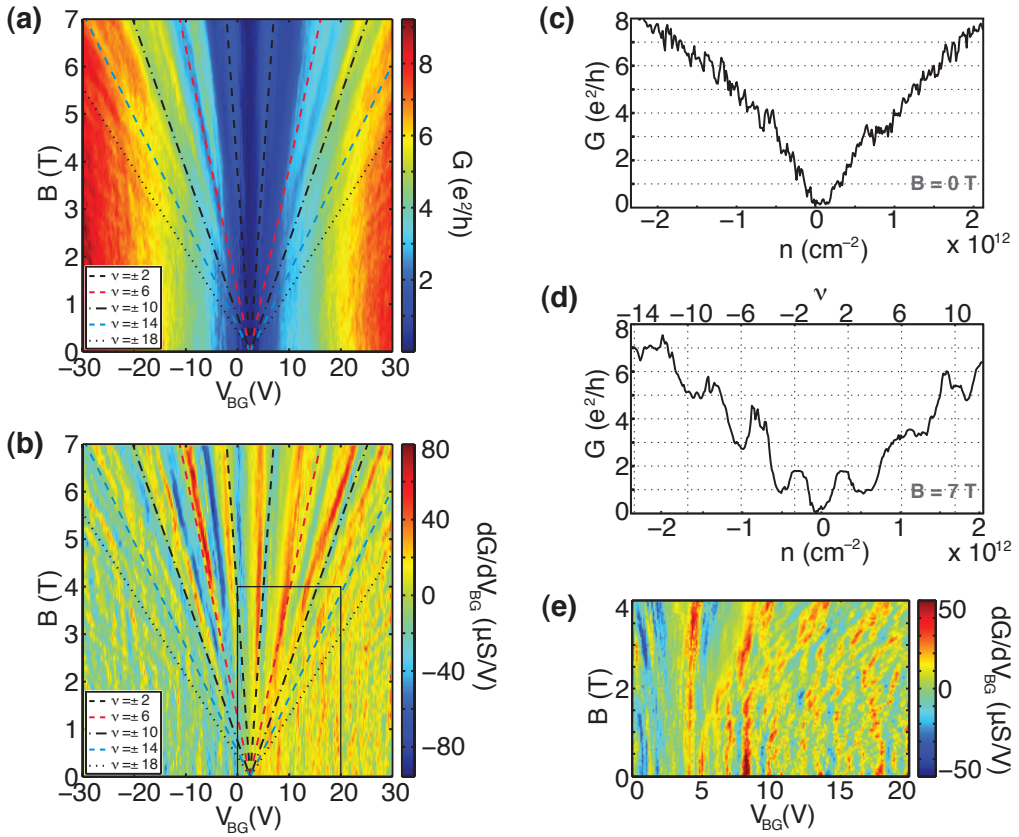

Figure 6.4: (a) Differential conductance measurements as a function of back gate voltage and applied magnetic field showing the development of quantized conductance plateaus with increasing magnetic field. (a) Numerical derivative of the data in (a) with respect to V_{BG}. For both (a) and (b) the expected position of the filling factors for single layer graphene is indicated by the fan-like lines. (c) Differential conductance G versus charge carrier density at $B = 0$ T. (d) Quantized differential conductance G versus charge carrier density at $B = 7$ T. The y-grid gives the position of the filling factors ν for this B-field. (e) Zoom into the region indicated by a black box in (b). The device has a width of 122 nm and length of 100 nm and was measured at $T = 1.6$ K.

was 100 nm long and 122 nm wide. In Fig. 6.4 (a) the evolution of the conductance in B-field is plotted as a function of applied back gate voltage V_{BG}. To get a better feeling for the magnitudes plotted in this two-dimensional graph, we first look at two cuts at a constant magnetic field.

For zero magnetic field (see Fig. 6.4 (c)), the conductance is suppressed between 0 and 3 V. Outside the transport gap it increases monotonously to values of up to $8e^2/h$ as the density is increased to $n \approx 2 \cdot 10^{12}$ cm^{-2}. The curve changes drastically, though, when the same trace is recorded at the maximum magnetic field of $B = 7$

T, as is visible in Fig. 6.4 (d). Here, the conductance rises in an oscillatory manner away from the charge neutrality point. Local minima at $G = e^2/h$, $3e^2/h$ and $5e^2/h$ are observed, which are connected to the adjacent one by a local maximum in the conductance. A periodicity is apparent in the density dependence of G, pointing towards the presence of quantized energy levels. The vertical dashed lines in the plot mark the density values for the filling factors ν as they are expected for single layer graphene according to the plate capacitor model. Indeed, close to each of those filling factors, a local minimum is reached. This evidences that the DOS condenses into Landau levels and the minima can be interpreted as being the conductance plateaus expected for the quantum Hall effect.

In Fig. 6.4 (a) we now understand the fan-like pattern appearing for $B > 2.5$ T as the evolution of Landau levels. Following in B-field the point at which a conductance steps is occurring in this graph, should therefore be equivalent to moving along lines with constant filling factor ν. The overlaid lines in Fig. 6.4 (a) resemble the position of Landau levels as a function of magnetic field determined from the plate capacitor model. Although this model is probably not accurate for the present device geometry (the lateral extent of the capacitor plate represented by the ribbon is much smaller than the distance between the two plates), the indicated Landau levels and the measurement are in good agreement. This is seen even better in Fig. 6.4 (b) where the derivative of the conductance with respect to the back gate voltage is plotted. Filling factors up to $\nu \pm 18$ are well resolved.

As mentioned, the fan-like pattern is established for $B > 2.5$ T only. To look into the transition more closely, a higher resolution measurement of the range marked in Fig. 6.4 (b) was taken and is displayed in panel (e) of the same figure. A number of states (mainly in the left part of the graph) are observable that do not show a dispersion in B-field. Other states (mostly away from the charge neutrality point) wiggle around as the magnetic field is ramped up, merge with others and/or split. Therefore it is difficult to follow one particular state all the way from low magnetic fields to the quantum Hall regime. We attribute the B-field dependence for $B < 2.5$ T to the fact that transport is governed by localized states that are hardly influenced by the flux penetrating the graphene layer. Only at high fields when well separated Landau levels develop, the conductance of the nanoribbon is dominated by transmission through edge channels.

We now comment on the fact that the conductance values are lower than the ones obtained in measurements on a Hall bar. Instead of being located at half integer multiples of $4e^2/h$, the plateaus in Fig. 6.4 (d) take values that are only half of the ones expected for the respective Landau level. Since all measurements were taken in a two-probe configuration a contribution of the leads has to be taken into account for the interpretation of the data. Like for a wide Hall bar, clean edge channels should be present in the bulk leads. These channels propagate into the constrictions as well. However, due to the size confinement, charge carriers occupying the higher Landau levels experience back scattering. Hence the total conductance through the system drops as is observed in the measurements.

Altogether, conductance quantization in high magnetic fields was observed in several nanoribbons with $W \gtrsim 75$ nm fabricated both from single- and bilayer graphene. In the latter ones, however, only the first quantization step was developed clearly. For single layer, although the effect is getting less pronounced, quantization was still recorded for the ribbon with $W = 75$ nm and $L = 200$ nm introduced earlier in this chapter. The fact that the plateaus get smeared out indicates that the formed transport channels extend approximately $W/2$ from the edge into the bulk of the ribbon and scatter into each other. Detailed width dependent studies of the visibility of the QHE in nanoribbons may therefore provide a method of probing the spatial extent of edge channels in the quantum Hall regime.

6.3 Side gate influence

Changing the potential landscape locally helps us to understand the spatial arrangement of localized islands inside the narrow channels. Transport studies on graphene nanoribbons with two nearby in-plane side gates were carried out. While one of the side gates (SG1) affected the drain side of the ribbon preferentially, the other (SG2) acted more on the source side. By tuning the side gate voltage with respect to the back gate voltage, the conductance resonances inside the transport gap are shifted in energy according to the coupling of the side gate to the respective localized state. Assuming that mainly the distance between the gate and the charged puddle determines the coupling, Coulomb blockade resonances evolving with similar slopes should originate from the same localized sites.

Typical gate-gate maps are shown in Fig. 6.5 (a) and (b), where SG1 and SG2 were used, respectively, to tune the conductance resonances in the back gate voltage range 9 V $\leq V_{\mathrm{BG}} \leq$ 10 V. In each graph, two different slopes for the evolution of the Coulomb blockade resonances are distinguishable. This finding indicates that only two localized islands dominate the transmission through the nanoribbon in the investigated gate regime. The measured device has a length of $L = 200$ nm and a width of $W = 80$ nm. Applying the rule of thumb for the number of puddles ($p \approx L/W$) as introduced in chapter 5.3.6 for a ribbon of these dimension, yields two to three localized islands and hence agrees well with the result of this measurement.

Relative lever arms α can be extracted from the slopes in Fig. 6.5 (a) and (b) which characterize the strength of the capacitive coupling of the side gate with respect to the back gate. The values determined from Fig. 6.5 (a) and (b) are $\alpha_{\mathrm{SG1}} \approx 0.74$ and 0.31 for SG1 and $\alpha_{\mathrm{SG2}} \approx 0.78$ and 1.94 for SG2. A rough estimate for the position of the respective localized state is possible with these numbers. As the lever arm ≈ 0.75 appears in both plots, the corresponding puddle is likely sitting in between the two side gates or in other words in the center of the ribbon. The other resonance is tuned only weakly by SG1 ($\alpha_{\mathrm{SG1}} \approx 0.31$) but strongly by SG2 ($\alpha_{\mathrm{SG2}} \approx 1.94$), which suggests that the corresponding localized state is located much closer to SG2 than to SG1. Additionally, it couples better to the side gate than to

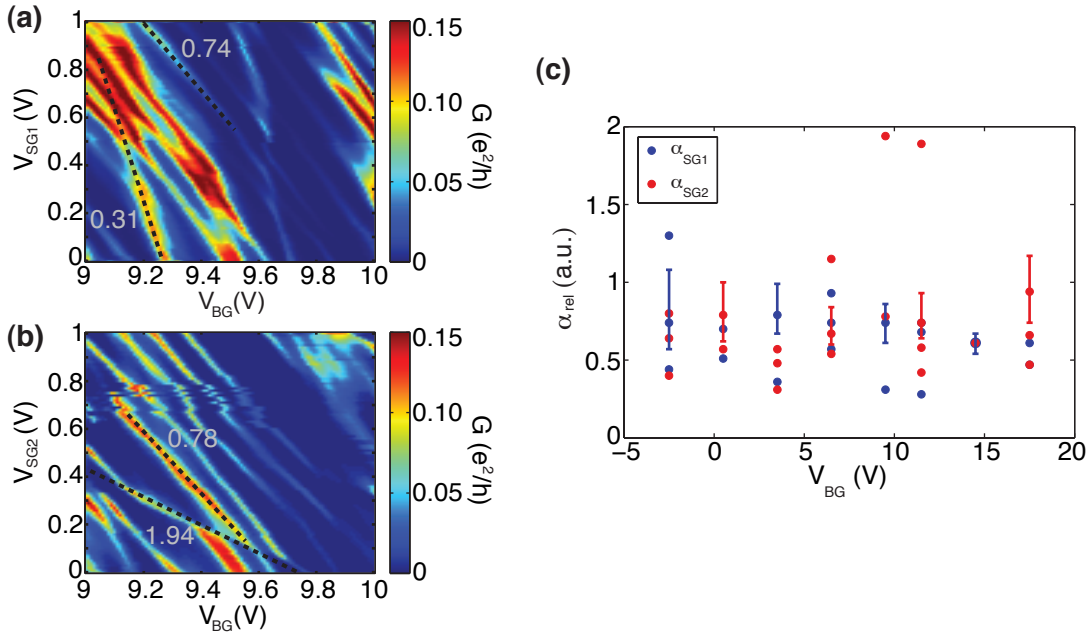

Figure 6.5: Conductance G as a function of side gate voltage V_{G1} in (a) and V_{G2} in (b) for the back gate voltage 9 V $\leq V_{\mathrm{BG}} \leq$ 10 V inside the transport gap. Black lines indicate the evolution of Coulomb blockade resonances and are labeled with the corresponding relative lever arms. (c) Relative lever arms α for different back gate configurations inside the transport gap extracted from maps similar to (a) and (b). The exemplary error bars arise from the fitting imprecision.

the back gate indicating that the back gate influence is screened relative to the side gate influence.

Measurements like those shown in Fig. 6.5 (a) and (b) were performed for several back gate ranges inside the transport gap and the corresponding lever arms were extracted (see Fig. 6.5 (c)). Generally, several slopes were recorded in all regimes, however never more than four different ones. Furthermore, the discussed anti-correlation of the relative lever arms originating from different side gates is observed in most back gate voltage ranges as well. For the analysis, several Coulomb resonances with similar slopes were fitted to extract the relative lever arms. Since the evolution of such resonances in the gate map is not perfectly linear, a dispersion around a mean value is obtained. This error is relatively large, as it can be seen from the indicated error bars in Fig. 6.5 (c). Nevertheless, the varying values for α inside the transport gap illustrate the modulation of the coupling of distinct states to the gates. This effect may be explained by puddles rearranging themselves inside the constriction. Along with the tuning of the back gate voltage comes a change in the potential landscape and hence in puddle size and position - some get larger and

even merge with neighboring ones, others fall into smaller islands.

In conclusion, a small number of puddles along the nanoribbon influences the transmission. The exact number and arrangement of these islands is changed as a function of Fermi energy as reasoned from the lever arm modulation. Hence, the experiments on side gated graphene nanoribbons support statements about the mesoscopic character of the system made earlier in this chapter.

6.4 Thermal cycling

In the previous sections transport properties were interpreted as the finger print of disorder in the graphene nanoribbons that were investigated. However, the microscopic origin of this disorder based on experimental results was not discussed so far. Two contributions - edge and bulk disorder - were identified in chapter 5.3.3 but not further specified.

In order to shine light on the character of these influences, conductance spectra of a nanoribbon were measured at $T = 1.25$ K before and after warming it up to room temperature. The recorded data is shown in Fig. 6.6 where the conductance inside the transport gap is plotted as a function of applied back gate voltage.

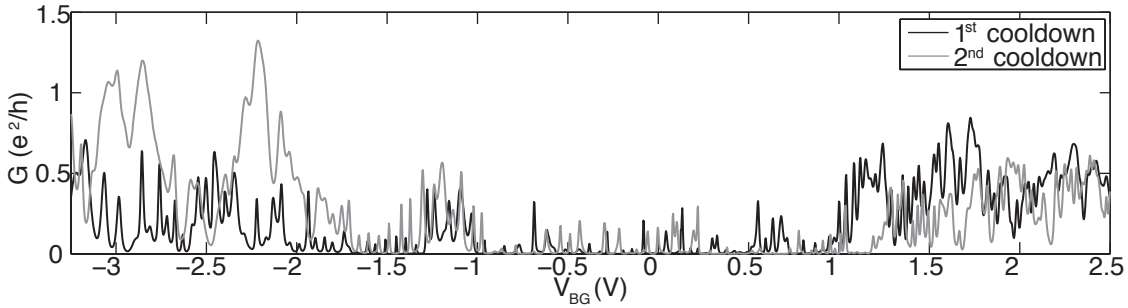

Figure 6.6: Conductance G as a function of applied back gate voltage V_{BG} before and after warming the sample to room temperature. The data shown was measured for a nanoribbon with length $L = 200$ nm and width $W = 75$ nm at a temperature of $T = 1.25$ K. A DC bias voltage $V_{\mathrm{bias}} = 500$ μV was applied and the conductance was recorded using standard lock-in techniques at a frequency of 13 Hz and an AC bias modulation of $V_{\mathrm{mod}} = 50$ μV.

Both measurements exhibit a region of suppressed current in the gate voltage interval -1.5 V $\leq V_{\mathrm{BG}} \leq$ 1 V and the conductance resonances show the same order of magnitude in this regime. Some Coulomb blockade resonances even fall on top of each other. As the gate voltage is moved away from the center of the gap, the conductance spectra differ more. In contrast, some main features like the small peak spacing at positive gate voltages and the larger spacing for negative V_{BG} are preserved.

These observations indicate that the potential landscape that causes the conductance fluctuations at low temperatures undergoes a significant change at $T \approx 300$ K. The thermal energy associated with room temperature is low compared to energies necessary to reconstruct the graphene lattice or to break covalent bonds. Hence, disorder is not only caused by the disordered edge structure of the graphene lattice, nor is it only some bulk disorder due to lattice imperfections, rippling, or other structural properties. Imperfections that can rearrange at room temperature, on the other hand, are charge traps in the SiO_2, adsorbates and debris on the surface, etc. The here discussed measurements therefore show that the environment (e.g. substrate, processing residues) has an important influence on the transport characteristics in graphene nanoribbons.

6.5 Conclusion and outlook

All structures presented in the last two chapters were fabricated on Si/SiO_2 substrate and carved into a graphene sheet by means of dry etching. The main conclusion of these chapters is, that the mesoscopic character of transport through graphene nanoribbons originates from disorder at both the edges and in the bulk. As discussed earlier, environmental effects like those coming from the substrate or adsorbates on the graphene surface are likely to have a large impact on the potential landscape. As a consequence of the strong disorder, the transmission tunability can be strongly non-monotonic due to conductance resonances in the constriction. Since narrow and short constrictions serve as tunneling barriers in nanoscale devices, the reduction of bulk disorder and the construction of well controlled edges are desirable. Several approaches have been realized recently to improve on these issues, namely (i) the bottom-up growth of graphene nanoribbons from precursors containing benzene rings [116] and (ii) the fabrication of suspended nanoribbons showing quantized conductance at zero magnetic field [75].

The results of these very recent studies give hope for graphene electronics since the influence of bulk and edge disorder is potentially negligible in these systems. However, both the bottom-up growth as well as the suspended graphene come along with some drawbacks as well. The bottom-up ribbons are grown on a conductive substrate and need to be transferred to an insulator, and the suspended ribbons are extremely fragile (in addition they are very small so far, so processing, contacting etc. is not trivial).

Substrate supported nanostructures are preferable due to their better stability. It was shown [31], that hexagonal boron nitride (BN) as a supporting material maintains high electronic quality of graphene sheets and is hence a promising substrate for devices. However, it remains to be investigated how the etched edges influence transport in nanoribbons built on a BN substrate.

Another alternative is the use of bilayer instead of single layer graphene and will be discussed in chapter 8. Since a real band gap can be opened in this system as a

perpendicular electric field is applied, electrostatic confinement may be possible like in GaAs devices. The apparent advantage of this method would be the smooth confinement potential in contrast to rough edges in to date devices. The parabolic band structure of bilayer graphene may change the over all properties of the bulk material as well as compared to the linear dispersion of single layer graphene. For nanostructures, in which the confinement induces quantized energy levels, the concept of energy bands is not valid however and therefore poses no limitation.

In conclusion, a graphene nanostructure with low disorder and high tunability is most likely achieved by using a crystalline substrate, which matches the graphene lattice structure well (e.g. BN), and avoiding edge disorder induced in the patterning process.

Chapter 7

Bilayer graphene quantum dots

In the previous chapters charge transport was restricted to one dimension in narrow channels. The main result of the studies carried out on graphene nanoribbons was that they consist of a chain of charged islands along which charge carriers are transported. Whereas those localized states develop randomly due to underlying potential, we will discuss measurements on an intentionally formed island in this chapter. Such a structure, that leads to the confinement of charge carriers in all three dimensions, is termed quantum dot (QD), since quantum mechanical effects are getting more relevant as the electronic wave function is localized.

Individual charge carriers that are trapped inside the QD are well shielded from environmental perturbations and hence their properties can be investigated separately. In graphene a number of experiments have demonstrated the possibility to realize QDs by etching the graphene flake into the desired shape. In the classical regime electron-electron interaction leads to Coulomb blockade (see chapter 5.3.2) and enabled e.g. time-resolved measurements of electronic transport [117]. As the quantization into quantum mechanical energy levels was achieved, this energy spectrum could be probed and individual spin states were read out [118]. However, the larger the number of charge carriers in the system is, the more complex does its energy spectrum get. It is hence desirable to reach the few electron or hole limit. Due to the continuous transition from electron to holes in single layer graphene, the location of the charge neutrality point is difficult [107].

Bilayer graphene, on the other hand, may offer an appropriate solution to this limitations since an energy gap, much like in a conventional semiconductor, should separate the last hole from the first electron. In the following we will first present tight-binding calculations and later compare those to experiments on a top gated bilayer graphene QD.

7.1 Predictions for an ideal quantum dot

Numerical tight-binding calculations were carried out on a quadratic bilayer graphene island of edge length 60 nm by F. Libisch [private communication]. For the

simulations, up to the third nearest neighbor was considered within the sheet and in the second layer the nearest neighbor was taken into account. The two layers were AB-stacked and the potential variations at the dot boundaries were slow compared to the lattice constant. Setting this boundary condition, a smooth edge is modeled. Similar simulations were performed in Ref. 119 and more details on the simulation method can be found there.

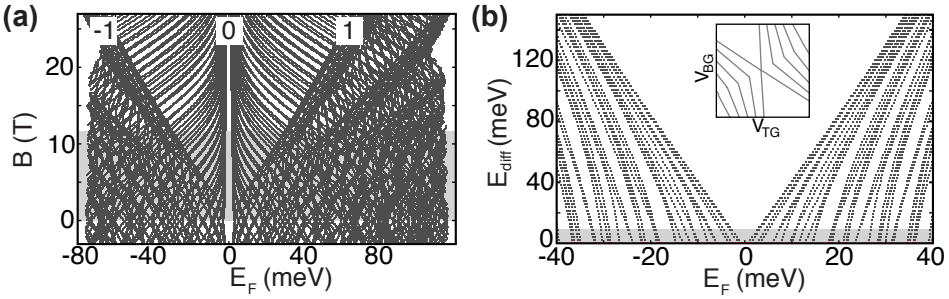

Figure 7.1: Numerical tight-binding calculations of the eigenenergies of a bilayer graphene quantum dot (a) Magnetic field dependence assuming a band gap of E_{gap} = 4 meV. (b) Dependence on the potential difference E_{diff} between the two layers (B = 0 T). The inset shows the energy level spectrum as it is oriented in the gate-gate plane used for the experiments. The grey colored areas mark the expected experimentally accessible range.

A quantum dot exhibits quantized energy levels due to confinement at zero magnetic field. The spacing between those energy levels is determined by the underlying density of states. For bilayer graphene, the DOS is constant in energy due to its parabolic dispersion relation. As a consequence, the energy levels will be equally spaced. The orbital electronic states are influence by a finite magnetic field applied perpendicular to the graphene plane. At high fields, the density of states condenses into discrete Landau levels. Their position in energy reflects the carrier characteristics and is a distinctive fingerprint for bilayer graphene.

Figure 7.1 (a) shows the evolution of the energy levels in a magnetic field as obtained from numerical calculations. The gap in the spectrum around $E_{\mathrm{F}} = 0$ represents an assumed band gap of $E_{\mathrm{gap}} = 4$ meV due to a potential difference between the two layers imposed in the calculation. This value is compatible with the gap size determined from transport measurements on bulk double gated graphene bilayer devices as presented in chapter 3.3.2. At low fields, a complex pattern of peaks wiggling in B-field is observed, which eventually move towards one of the LLs indicated by the respective number in Fig. 7.1 (a).

The range available in the experiments presented in the following is marked by the grey box in the graph. Although the simulation does not include the charging energy separating each state from its neighbor, the main features are pronounced enough to be observable in transport measurements. Namely these are the bending

of peaks with $E_F < 25$ meV towards the $n = 0$ LL for high magnetic fields and the chaotic peak evolution for the remaining part of the spectrum.

Tuning the potential difference E_{diff} between the two layers to a finite value causes a splitting of the electronic bands at $E_F = 0$ and hence the electronic states need to move to higher absolute values of E_F. Panel (b) of Fig. 7.1 displays the simulation for an applied perpendicular E-field where this trend is clearly visible.

Again the grey colored area indicates the parameter range which can be covered. Here, the maximum achievable potential difference E_{diff} is assumed to be the same as for bulk devices. This assumption remains to be scrutinized in the following. Characteristics of the spectrum in the experimental range are the different slopes of adjacent peaks. Whereas the energetically high lying states exhibit almost no energy dependence as E_{diff} is increased, a significant energy gain or loss is observed for the low lying states. As a result, the peak-to-peak spacing is expected to vary as a function of E_F, which should be detectable in experiments besides the change of peak slopes.

The numerical calculations presented here provide a number of signatures to be looked for in experiments. Since the simulations considered the graphene to be perfectly clean, doubts may arise about the relevance of those predictions. It should be noted, however, that the data obtained on a single layer dot in Ref. 107 could successfully be explained by a model assuming zero disorder potential.

7.2 Sample fabrication

Applying the processing steps introduced in chapter 5.2 the QD device was fabricated from a bilayer graphene flake deposited onto SiO_2 substrate. Two micrographs in Fig. 7.2 display the device layout. The resulting island had a size of 85×50 nm^2 and the constrictions that constitute the tunneling barriers were measured to be 20 nm wide. A nearby charge detector had a width of 40 nm. Measurements on the latter will however not be discussed here.

The top gate dielectric used for this device is commercially available under the name Cytop^{TM} and is a fluoropolymer used mainly for coatings and in organic thin film field effect transistors [120, 121]. It has a relative permittivity of $\epsilon \approx 2.1$-2.2, withstands high electric fields and has been proven to be highly electrically stable. After spin coating the chip with the polymer (see Appendix E for parameters), a local top gate was defined by e-beam lithography followed by metal evaporation (2 nm Ti/ 40 nm Au) and lift-off. Since Cytop^{TM} is highly water repellant, a 5 nm thick Cr-layer was evaporated prior to the application of the e-beam resist and removed in an etching step after patterning the top gate. In Fig. 7.2 (b) the location of the TG electrode is depicted by the red dashed contour. It covers not only the island itself but also the constrictions and the charge detector.

A first set of data was recorded in a dilution refrigerator at base temperature of $T = 120$ mK to characterize the sample before adding a top gate (TG). Although

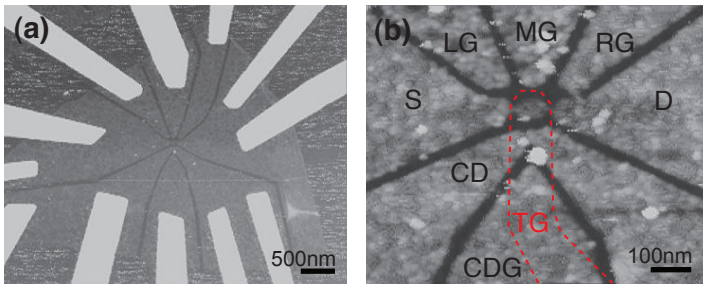

Figure 7.2: AFM images showing the sample before the top gate was processed (a) Micrograph of the complete flake where the white parts are the metallic contacts, the light grey part is the graphene flake and the dark lines show the region where trenches were etched into the graphene. (b) Zoom into (a) where the island is located in the middle of the image and is connected to source (S) and drain (D). A number of gates (left gate (LG), middle gate (MG), right gate (RG) and charge detector gate (CDG)) is located around the quantum dot and a charge detector (CD) is lying nearby. The area marked by the red dashed line was in a second step covered by a top gate electrode (TG).

no explicit presentation of these data is provided in this chapter, a comparison of important parameters will be done.

7.3 Sample characterization

Cytop^{TM} has previously been used as a dielectric at room temperature only [120, 121]. Experiments at 4 K were therefore carried out in a dip stick setup to test the material stability at cryogenic temperatures.

The recorded back gate dependence is presented in Fig. 7.3 (a). Within the measured gate range the current is mostly suppressed and only few spots exhibiting higher transmission are present within the transport gap. This behavior is qualitatively similar to what was observed in measurements taken on the same device before the TG was added, as shown by the blue trace in the same figure. We can therefore remark that the size of the transport gap in back gate direction overcomes the values for nanoribbons determined in chapter 5.3.5 by far.

Since transport is mainly dominated by the constrictions, as they are the narrowest points in the structure, two points can be mentioned to provide an explanation for these large values. Firstly, the ribbons used here were only half as wide as the narrowest ones investigated in chapter 5.3.5. Extrapolating the width dependence found there, a transport gap $\Delta V_{BG} > 30$ V is to be expected. Secondly, the two constrictions constituting the tunneling barriers for the island are not necessarily doped by the same amount and hence their transport gaps may be shifted with respect to

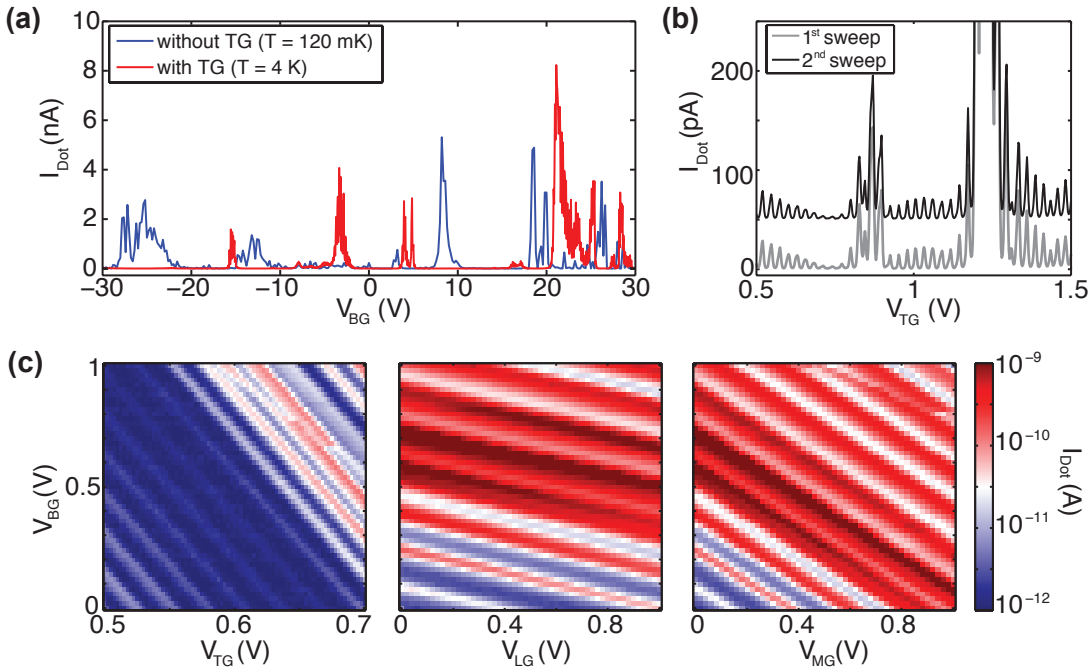

Figure 7.3: (a) Back gate characteristics before (blue trace) and after (red trace) the top gate was patterned. Both curves were recorded with a bias of $V_{\mathrm{bias}} = 5$ mV at 120 mK and 4 K, respectively. (b) Top gate dependence for $V_{\mathrm{BG}} = 0$. The two sweeps were recorded at 4 K one after the other with $V_{\mathrm{bias}} = 5$ mV. Black curve is shifted by + 50 pA for clarity. (c) Two-dimensional maps for left: BG vs. TG ($V_{\mathrm{LG}} = V_{\mathrm{MG}} = 0$) , middle: BG vs. LG ($V_{\mathrm{TG}} = 0.7$ V, $V_{\mathrm{MG}} = 0$) and right: BG vs. MG ($V_{\mathrm{TG}} = 0.7$ V, $V_{\mathrm{LG}} = 0$). All measurements were taken at 4 K with $V_{\mathrm{bias}} = 5$ mV.

each other in gate voltage. Since the transmission is dominated by the constriction, which is pinched-off the most, the gap in back gate space gets effectively larger. At the gate voltage values that show higher over-all current (e.g. around $V_{\mathrm{TG}} = 0.8$ V and 1.25 V), the coupling to the leads is rather good and hence more charge carriers can pass through the structure.

Zooming into the gapped region but now sweeping the voltage applied to the top gate electrode while keeping $V_{\mathrm{BG}} = 0$, illustrates the remarkable stability of the device. The two traces in Fig. 7.3 (b), taken one after the other, fall perfectly on top of each other. They reveal a number of Coulomb blockade resonances that are mostly equally spaced as commonly observed for single quantum dots. For a brief introduction to the transport mechanisms in the regime of Coulomb blockade we refer to chapter 5.3.2.

From the size of the corresponding Coulomb blockade diamonds (not shown here) a charging energy of $E_{\mathrm{c}} \approx 8$ meV was extracted. Representative measurements are

displayed in Fig. 7.5 (b) and 7.7 (a) where diamonds in different gate regimes were recorded. In chapter 5.3.6 the correlation between the charging energy and the size of the quantum dot was discussed. The data point extracted from this device would be located well below the data for single layer QDs represented in Fig. 5.9, meaning that its capacitance is sufficiently larger. This increased shielding can be explained by the additional metallic reservoir induced by the top gate electrode. Indeed the maximum size of Coulomb blockade diamonds measured before adding the TG was E_c ≈15 meV. This value is comparable to similar data obtained with single layer quantum dots.

Next we discuss the tunability of the carrier number on the island. Four gates could be used to shift the energy levels inside the QD. To determine the relative lever arms of these gates, the current through the device was recorded as a function of two gates at a time. Fig. 7.3 (c) displays the resulting two-dimensional plots where the BG was tuned with respect to the TG, the left gate (LG) and the middle gate (MG), respectively. In all plots a number of resonances running parallel to each other are visible. As mentioned before, the peak amplitude is modulated in all three cases as the tunneling barriers are more or less transparent.

	without TG at 120 mK	with TG at 4 K	with TG at 120 mK
$\alpha_{LG/BG}$	0.8*	0.25	0.31
$\alpha_{MG/BG}$		0.67	0.66
$\alpha_{TG/BG}$	-	6	8.7

Table 7.1: List of relative lever arms for the different gates with respect to the back gate. Compared are the values before and after the TG was added.
* Since the left gate and the middle gate were short-circuited in the first measurements (without TG), only one value exists for both.

Besides these similarities the apparent difference between the graphs is the slope of the resonances or, in other words, the relative lever arm of the respective gate. A direct comparison of the lever arms is given in Tab. 7.1. Since the TG is located directly above the islands with a distance of only ≈25 nm, it provides the strongest tunability on the island. In contrast to this vertical arrangement, the side gates exert an electric field only laterally on the island. Hence, more voltage needs to be applied to change the number of charge carriers on the QD. Additionally, the gap between the middle gate and the island is >30 nm and the left gate is even >50 nm away. The obtained hierarchy of the relative lever arms can therefore well be explained by the sample design.

Furthermore, the previously discussed decrease of the charging energy E_c after adding the TG as compared to the device without, is resembled in the change of the relative leverarms. The influence of the middle gate on the dot levels was considerably larger before the additional electrode was fabricated, making the enhanced

shielding due to the metallic finger gate apparent.

7.4 Electric field dependence

As discussed in the introduction of this chapter, opening a band gap in a bilayer graphene quantum dot would allow for the unambiguous separation of holes and electrons. According to the tight-binding calculation for a bilayer graphene quantum dot in a perpendicular electric field (see Fig. 7.1 (b)), the electronic eigenstates drift to higher absolute energies values as the layer symmetry is broken. Therefore, in this section, the evolution of the QD energy levels in a perpendicular electric field will be discussed.

All measurements were taken in a dilution refrigerator at the base temperature of 120 mK. However, the electron temperature extracted from fits to Coulomb blockade resonances assuming multilevel transport, resulted in $T_{\mathrm{el}} \approx$ 1-2 K. Similarly high values were obtained also for the measurements before the TG was added, meaning that the large discrepancy between base temperature and electronic temperature does not originate from the additional material. Depending on the regime it either stems from a small tunneling coupling to the leads, which prevents cooling of the island via thermal equilibration to the reservoirs, or from a large tunneling coupling, which causes the peaks to be coupling-broadened.

To get a feeling for the location of the charge neutrality point in gate space, both BG- and TG-characteristics were recorded at room temperature where the transport gap is not developed and the structure is transparent for charge carriers. Leaving the respective other gate grounded, the obtained values were $V_{\mathrm{D,BG}} \approx +8$ V and $V_{\mathrm{D,TG}} \approx +1$ V. Using the relative leverarm given in Tab. 7.1, these two values can be converted into each other as it is expected from two gates both tuning the very region, which is dominating transport through the structure. Throughout the low-temperature measurements, we focus on a gate range for BG and TG around the determined charge neutrality point.

For the E-field dependence, we split the investigated TG-range (1.4 V $< V_{\mathrm{TG}} <$ 6.1 V) into intervals of 1.5 V. By sweeping through such an interval and then stepping the BG-voltage from -30 V to +30 V, we cover all accessible electric field values. Within each TG section a number of Coulomb resonances is visible. In order to track the same resonances through the whole BG-range, we compensate for the shift of the peaks induced by the BG according to $V_{\mathrm{TG,eff}} = V_{\mathrm{TG}} - 0.11 \cdot (V_{\mathrm{BG}} + 30V)$. Further, to avoid misinterpretation due to drift in time, we step the BG both up and down. Except for unavoidable charge rearrangements, the peak evolution was found to be reproducible.

A representative segment, measured as described, is shown in Fig. 7.4 (a). The evolution of the approximately 30 Coulomb blockade peaks can be followed over large ranges in BG direction. A number of horizontal lines within the graph indicates the occurrence of charge rearrangements as the back gate voltage is stepped. It should

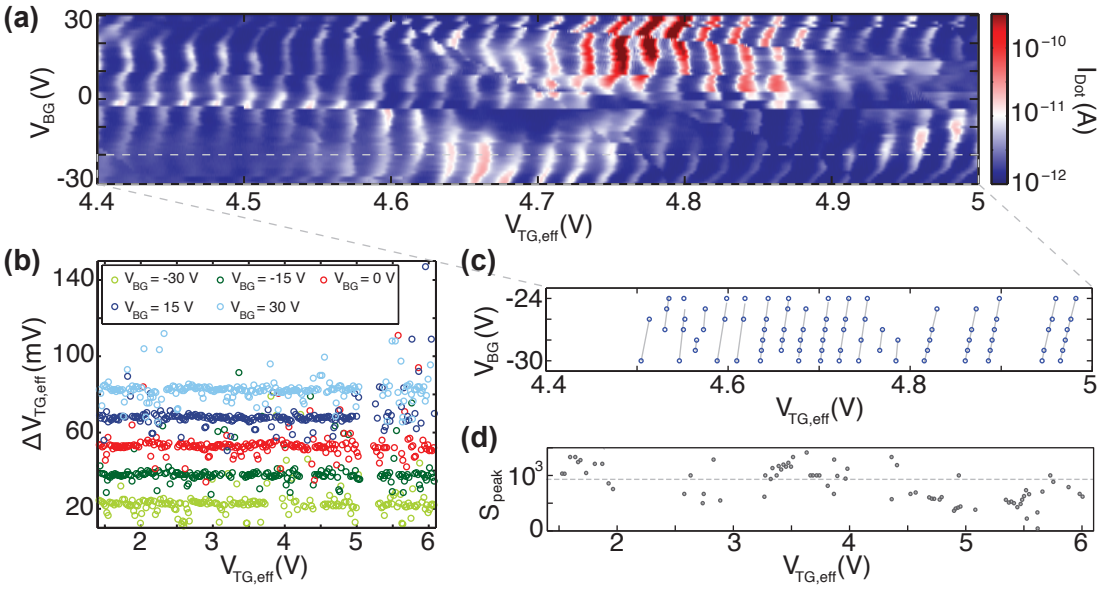

Figure 7.4: (a) Representative segment of Coulomb blockade peaks as a function of applied V_{BG} and $V_{\mathrm{TG,eff}}$ (see text for the definition of the latter). The bias voltage between source and drain was $V_{\mathrm{bias}} = 3$ mV. (b) Extracted peak-to-peak spacing for cuts at constant V_{BG} in measurements like in (a) but for a larger range of $V_{\mathrm{TG,eff}}$. (c) Determined maxima (circles) and fitted slopes (grey lines) for the Coulomb resonances outlined by the dashed box in (a). For each peak in the $V_{\mathrm{TG,eff}}$ interval, the respective slope value obtained from the fit is plotted in (d). The dashed line indicates the mean value of S_{peak}.

be noted however, that the small number of such charging events is another evidence for the striking electronic stability of the sample. Another set of lines with finite slopes is observed (e.g. in the range 10 V $< V_{\mathrm{BG}} <$ 30 V and 4.6 V $< V_{\mathrm{TG,eff}} <$ 5 V) causing abrupt jumps in the peak spectrum. These can be attributed to localized states that are less strongly tuned by the TG than the QD resonances but still influence the transport.

Moreover, within the large BG voltage range examined here, the transmission amplitude of a single resonance can change by up to two orders of magnitude. This observation illustrates convincingly that the transmission sensitively depends on the specific gate configuration. Depending on the specific level spectrum within the constrictions and the dot, the coupling will be weaker or stronger.

To analyze the data, two approaches were chosen which we will present now. In the first case, we extract the peak-to-peak spacing of neighboring Coulomb blockade resonances at different values of V_{BG}. For an energy gap to be opened, the positive electronic eigenstates of the graphene quantum dot need to diverge from the negative ones and hence an increase (at the charge neutrality point) or a squeezing (for higher

charge carrier numbers) of the peak to peak spacing should be detectable in a perfect QD. The variations in peak-to-peak spacing originate from the spectrum of the single particle level spacing Δ_s. Hence, Δ_s needs to be sufficiently large compared to the charging energy to allow for the fluctuations to be visible in such an analysis. As will be discussed later, $\Delta_s = 1.2$ meV in the present devices, which is 15% of E_c and hence adequate to be detected.

In Figure 7.4 (b) the data obtained for the complete TG-range is plotted (each trace being vertically offset by 15 mV). Cross-sections at V_{BG} = -30 V, -15 V, 0 V, 15 V and 30 V were analyzed wherever the visibility was sufficient to locate peak maxima. Since the signal to noise ratio between $V_{TG,eff} \approx 5$ V and 5.3 V was too low for this experiment, the analyzed spectrum is gapped here. In previous measurements, carried out with higher voltage bias, it was verified, however, that the peak spectrum is continuous also in this interval and not gapped.

It gets apparent that the analysis results in a constant value of $\Delta V_{TG} \approx 25$ mV for most peak-to-peak spacings within the investigated $V_{TG,eff}$ range. This value corresponds to an energy of 10 meV applying the absolute lever arm $\alpha_{TG} \approx 0.4$ determined from Coulomb diamonds measurements. Since the shifts of the energy levels expected from the tight binding calculations presented in Fig. 7.1 (b) are on the order of few meV even for very low E_{diff}, they should hence be observable.

Before discussing possible explanations, we introduce a second way of inspecting the data. As the energy levels drift apart as a function of applied E-field for gapped bilayer graphene, they exhibit different slopes according to their energy value with respect to $E_F = 0$. Therefore, comparing the slopes of neighboring peaks in a specific interval for E_{diff} is expected to provide an indication for the location of the charge neutrality point. At this position, the slopes of energy levels emerging at positive or negative side would diverge at the vertical asymptote constituted by $E_F = 0$. Since we investigate the peak evolution in a gate-gate plot and not for E_{diff} as a function of E_F (see inset of Fig. 7.1 (b) for a visualization), the slopes are not expected to change sign but their magnitude.

Figure 7.4 (c) illustrates the method applied for the analysis with the help of the $V_{TG,eff}$ interval shown in panel (a) of the same figure. Within the back gate window -30V $< V_{BG} <$ -25 V, the extracted maxima belonging to one Coulomb blockade resonance were fitted with a first order polynomial in order to determine the slope S_{peak} of the respective peak. As the number of extracted maxima along a resonance is not always sufficient to allow for a reliable fit, the analysis was not carried out for all peaks in the spectrum.

Plotting the gained values for S_{peak} as a function of the effective TG voltage yields the distribution plotted in Fig. 7.4 (d). A rather large scattering of the data points is observed although care was taken to limit the analysis to well pronounced peaks. This shows that the movement in E-field of Coulomb blockade peaks indeed varies significantly. The grey dashed line marks the mean value of the peak slopes and serves as a guide to the eye to distinguish a change in magnitude of S_{peak}. For values of $V_{TG,eff} > 4.5$ V a tendency of decreasing slope can be observed, which

may be interpreted as a signature for the opening of a gap in the level spectrum. Due to the imposed restriction for the data included in the analysis, a meaningful evaluation was not possible for the opposite polarization of the electric field. Such data could have possibly supported the trend seen in Fig. 7.4 (d) and allow for a stronger statement.

Next, we give arguments for the discrepancy between the theory and the experiment. The fact that no distinct deviation from the constant peak-to-peak value is detected in the first analysis and the change in peak slopes is only weakly pronounced, indicates that the opening of a band gap and the accompanying evolution of the eigenstates is not the dominant process in the performed experiment. As mentioned in chapter 2, the energy gap obtained in transport measurements in bilayer graphene bulk samples deposited on SiO_2 is on the order of $E_{\mathrm{gap}} = 2{-}5$ meV [42, 43]. In a size confined structure like the QD presented here, the edge to bulk ratio increases significantly and any edge disorder may lead to an even decreased E_{gap}. Hence the effect on the eigenstate spectrum would get negligible. The large value for the transport gap ΔV_{BG} is an additional indication for a large density fluctuation amplitude in the system. However, this parameter does not allow to specify, whether the disorder is originating from the edges or the bulk.

7.5 Magnetic field dependence

To further shine light on the character of the states probed in the quantum dot, we place the device in a perpendicular magnetic field and examine the dispersion of the Coulomb blockade resonances as the magnetic field is tuned. As was done for the experiment investigating transport in an electric field, the B-field dependence was recorded in segments for the TG-voltage. Since the back gate voltage was kept at its maximum value V_{BG} = -30 V, the device is exposed to a displacement field of -0.22 V/nm $< D_{\mathrm{dis}} <$ -0.27 V/nm, additionally.

Characteristic data is displayed in Fig. 7.5 (a) where the TG window was again chosen to be located around the position of the charge neutrality point determined at room temperature. The horizontal lines at which the resonances experience a sudden shift (e.g. at 5 T for 5 V $< V_{\mathrm{TG}} <$ 6.1 V) in gate direction are again due to charge rearrangements. No data could be recorded for the upper right corner of the map since we encountered problems with the magnet stability in the measurement setup.

One of the main features in this graph is that the Coulomb blockade resonances run almost parallel to each other and hardly move along the gate axis as the magnetic field is stepped. Qualitatively similar data was recorded in other bilayer graphene quantum dots both with and without top gate electrodes as well. This observation is in strong contrast to the behavior of a single layer graphene quantum dot in a perpendicular magnetic field. As was shown experimentally and theoretically [107], the electronic eigenstates exhibit a linear dispersion in energy at low B but tend

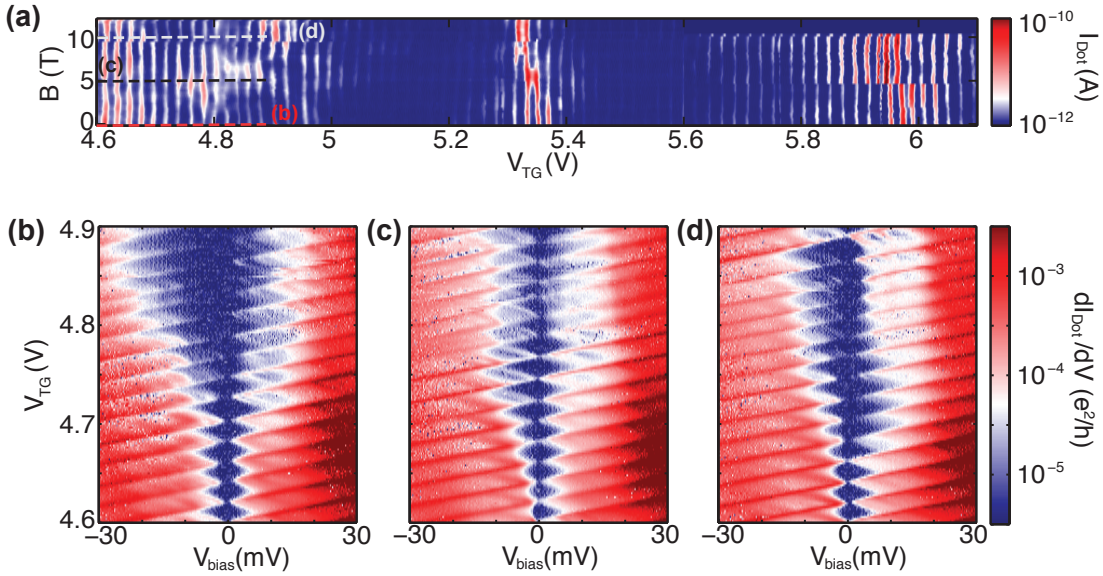

Figure 7.5: (a) Current through the QD as a function of B-field and TG-voltage taken at 120 mK. The back gate was set to -30 V and the applied bias voltage was $V_{\mathrm{bias}} = 3$ mV. The dashed lines mark the cross-sections at which the Coulomb diamonds shown in (b)-(d) were taken.

to merge into Landau levels at high fields. For the 0th LL this implies that single particle states lying lower in energy need to bend towards higher values to reach $E_{\mathrm{F}} = 0$ whereas states having higher energies tend to move to lower values. The therefore required moving of Coulomb resonances in gate direction was well visible in Ref. 107 and on the order of several 10 meV.

The tight-binding calculations carried out for a bilayer quantum dot using the same model as for the single layer graphene quantum dot in Ref. 107, were discussed earlier in this chapter. However, the properties featured by the calculation within the accessible measurement range are not resembled by the measured data. Whereas the simulation presented here assumed perfect edges and no bulk disorder, it is instructive to discuss a study conducted on single layer QDs exhibiting different types of disorder [119]. It is found that at defects breaking the A-B sublattice symmetry, states get localized. This is the case for rough edges as well as for certain types of adsorbates and thus a reasonable scenario for our sample. Since the size of such states is commonly smaller than the magnetic length l_{B}, they are not influenced by the external magnetic field.

Although these findings may explain the weak B-field dependence of the investigated bilayer graphene quantum dots, the microscopic picture is not fully understood. If indeed all probed states are localized, hopping transport would be expected leading to stochastic Coulomb blockade. This is however not observed here.

Another possible scenario is related to the fact that transport happens through multiple levels for almost all gate configurations. Averaging of several single particle levels could smear out the expected fluctuations and lead to the observed straight peak evolution.

Some peaks experience an amplitude modulation along the B-field axis. The characteristic length scales in magnetic field for the present quantum dot are given by its size. As the magnetic length $l_B = \sqrt{\hbar/eB}$ gets comparable to the system size, transport gets sensitive to the applied magnetic field. For the dot with a diameter of 60 nm, the critical magnetic field is $B = 1.8$ T. Since we assume that the transmission is dominated by the constrictions, the critical field at which the transmission starts depending on B should be estimated from the constriction width resulting in $B(20\text{ nm}) = 16.5$ T. Both values do not correspond to the field values at which the structure gets more transparent, showing that the amplitude modulation is not (only) correlated with the magnetic length.

If, on the other hand, we picture the QD as a quantum interference device, an amplitude modulation would be expected with a characteristic B-field period $\Delta B = (h/e)/A$ with A being the area threaded by the magnetic field. For the quantum dot a period of ≈ 1.5 T should hence be obtained. Since the amplitude modulations observed e.g. around V_{TG} take place on a magnetic field scale on the order of $\approx$ 5 T, the here suggested simple models for transport cannot provide a sufficient explanation for the finding. Most likely, an interplay of the two effects, combining processes in the constrictions and on the island causes the observed features.

This last statement is further supported when investigating Coulomb diamond measurements taken at different magnetic fields, namely $B = 0$ T, 5 T and 10 T. Figures 7.5 (b)-(d) present the differential conductance dI/dV_{TG} measured in the corresponding finite-bias spectra. As anticipated for a single quantum dot, the Coulomb blockade diamonds do not overlap. Furthermore, the size of the diamonds shaped areas stays constant in gate direction for all three cases. However, the extent of the regions of suppressed current in bias direction varies strongly. At $B = 0$ T, the diamonds exhibit well defined edges and a charging energy of $E_c = 8$ meV in the lower gate regime. For larger gate voltage on the other hand the boundaries of the diamonds are smeared out more and more.

Since the boundaries of the Coulomb diamonds are given by the condition, that a dot level becomes resonant with the electrochemical potential in one of the leads, the sharpness of the edge is an indication for the coupling strength between the dot and the respective lead. For the zero field data, for negative bias voltages the smearing happens at the lower edge, whereas for positive bias this is the case at the upper diamond edge. Hence, we can conclude, that the coupling strength to the source lead is strongly affected by the TG configuration. To explain this finding we reason with a slightly asymmetric alignment of the top gate electrode leading to a stronger tuning of the left reservoir.

It should be noticed, that the single particle spectrum was observed only in small gate regimes and a systematic study could therefore not be accomplished.

The limited visibility of excited states is most probably related to the high electron temperature T_{el} but also to the coupling conditions leading to multilevel transport in most gate regimes.

Recording the conductance within the same regime as for Fig. 7.5 (a) but at 5 T and 10 T results in less extended regions of suppressed transport. Although an asymmetry in the coupling is still observed, it is less pronounced for these measurements, indicating that the finite magnetic field increases the coupling. Recapitulating the discussion of chapter 6.2, where the behavior of graphene constrictions placed in a magnetic field was shown, a better coupling due to higher transparency of the tunneling barrier is indeed likely beyond a critical field. Since the quantum dot is pictured as being defined by narrow constrictions acting as tunneling barriers, we can explain our observations consistently.

7.6 High frequency gate manipulation

The experiments so far presented in this chapter all relied on a specific property of graphene nanoribbons, namely the presence of a transport gap. Although this feature is commonly utilized in graphene nanostructures as tunneling barrier, measurements of the tunneling coupling could so far not be accomplished for a single quantum dot connected to two leads. Additionally, the time evolution of quantum dot states e.g. the relaxation rates of excited states into the ground state have so far not been explored. Extracting the T_1-time is an important step to figure out whether spin manipulation experiments are feasible in graphene. For both parameters to be determined, time resolved measurements are required.

As proposed and realized in Ref. 122, the time dependence of the electronic states in a quantum dot can be investigated in transient current spectroscopy. In this technique, high frequency voltage pulses are applied to one gate, by this changing the dot configuration on a short time-scale. Simultaneously, the DC-transport across the structure is measured as a function of the pulse length. The resulting signal contains the time-averaged current and hence provides information about the population of energy levels.

7.6.1 Estimates on expected parameters

Before adapting this method to graphene devices, an open issues needs to be addressed. The highly doped Si back gate may induce a capacitive current between the pulsed gate and the substrate and hence attenuates the pulse signal. We can estimate the magnitude of this damping from the capacitance C_{gate} of a typical gate electrode since the reactance of this capacitance leads to a voltage division. The main contribution is given by the bond pad, which has an area of 100 $\mu\mathrm{m}^2$. The capacitance is therefore estimated by $C_{\mathrm{gate}} = \epsilon_0\epsilon \cdot (100 \times 100)\mu\mathrm{m}^2/d \approx 1.2$ pF with $d = 285$ nm being the SiO_2 thickness. Further, the reactance is determined by the

rise time τ_{rise} of the pulse generator. In the measurement setup used here, this value was $\tau_{\text{rise}} \approx 1$ ns resulting in $|X_{\text{gate}}| = 1/(2\pi f_{\text{max}} \cdot C_{\text{gate}}) \approx 130\ \Omega$. Assuming a low pass filter to be formed by the gate capacitance and any series resistance in the HF line, results in a cut-off frequency f_{c}. In order to have no damping of the signal amplitude, this series resistance has to be well below 1 kΩ (see Appendix B). The stainless steel coaxial cables used in the setup fulfill this requirement with an impedance of $R_{\text{cable}} = 50\ \Omega$. On the sample itself, resistances can occur if e.g. an in-plane gate is pulsed. Here, a contact resistance of $R_{\text{contact}} \approx 1$ kΩ should be taken into account.

Consequently, the high frequency manipulation of graphene samples having a back gate, should be feasible. Moreover, an increased bandwidth can be achieved by avoiding the use of side gates for pulsing and by minimizing the area of the bond bad. Here, experiments in which the TG electrode was used as the pulsed gate were carried out and will be discussed in the following.

7.6.2 High frequency setup

The challenge for high frequency measurements at low temperatures are manifold. Firstly, losses due to capacitive and inductive coupling of the signal to system components arise for fast signal modulation only. Secondly, the dissipated energy of these losses may couple as heat into the system preventing low electron temperatures. Moreover, electrical noise from the signal source may degrade the signal quality.

In the setup used in this work, the first two issues are addressed by the application of stainless steel coaxial cables. The well shielded inner conductor minimizes the signal dissipation due to its high electric conductivity. Since this latter property is beneficial for the heat transfer to the sample as well, a -20 dB attenuator acting as a cooling stage at the 1K pot is built in. Additional cooling is provided by the bias-tee (Anritsu K251) used to admix the AC-signal to a well thermalized DC-line. This component is located at the mixing chamber and due to the capacitive coupling of the AC voltage to the sample, any direct noise transfer is prohibited. An additional attenuation can be inserted at the top of the cryostat to block noise from the pulse generator. The setup was implemented within the course of the project carried out in Ref. 123 and a detailed description of the components can be found therein.

Standard lock-in techniques were applied to measure DC-transport through the quantum dot at constant voltage bias between source and drain reservoir. The modulated voltage signal was applied to the top gate (for the data shown here) and to the middle gate (being qualitatively similar to the TG data). Whereas a Yokogawa voltage source was used for the DC-part, the square shaped voltage pulses were generated by an arbitrary waveform generator (Tektronix AWG520) allowing for pulse lengths as short as 1 ns.

7.6.3 Proof of concept for experiments on graphene

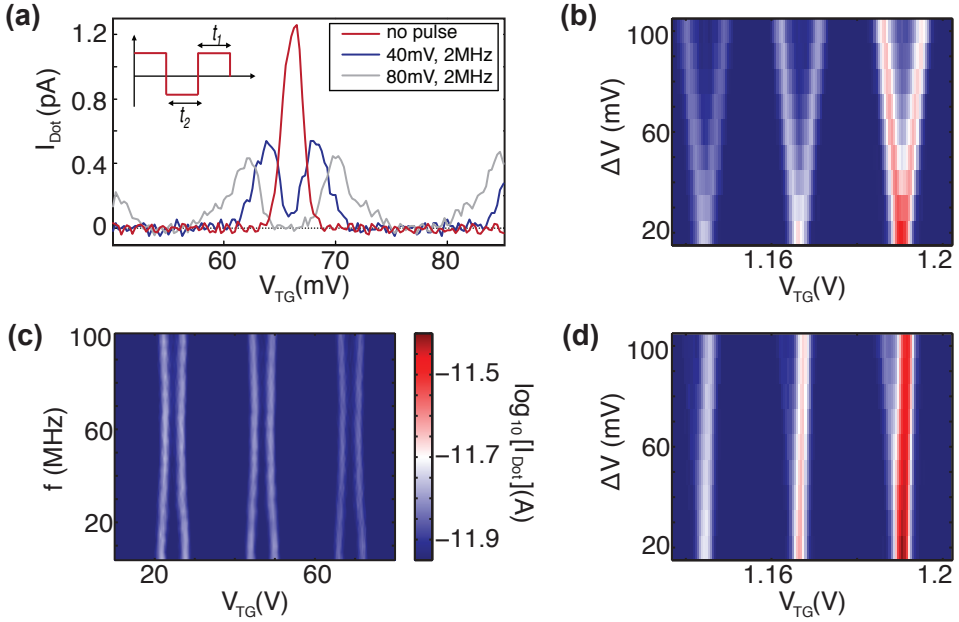

Figure 7.6: (a) Coulomb resonance for different amplitudes of the square pulse applied to the top gate. The inset shows the pulse shape and introduces the definition for the dwell times for two levels. (b) and (d) Evolution of three Coulomb resonances with increasing pulse amplitude for $t_1 = 5$ and 1 ns, respectively. (c) Frequency dependence of the peak spacing for $\Delta V = 40$ mV applied pulse amplitude. For all measurements a voltage bias of $V_{\text{bias}} = 1$ mV was applied. The colorbar is valid for all 2D-maps shown.

The red trace in Fig. 7.6 (a) exhibits a current peak at the gate voltage at which the resonance condition for transport through the quantum dot is fulfilled. As a symmetric square shaped AC-signal (see inset for a sketch of the pulse shape) is superimposed to the DC top gate voltage, this Coulomb resonance splits into two peaks, since the QD level comes into resonance two times as the TG is tuned towards more positive voltages - first for the upper pulse level and then for the lower. For the blue and the grey trace, the system spends an equal amount of time in the respective voltage level and hence the newly arising peaks exhibit approximately half the height of the original resonance. A slight asymmetry can be observed for the two peaks emerging at $\Delta V = 80$ mV. We attribute this to a smeared out pulse shape due to the damping of higher harmonics. The distance between the peak maxima increases linearly with the amplitude of the applied voltage pulse. This is seen even more clearly in Fig. 7.6 (b) where the splitting of three consecutive Coulomb resonances was followed as the pulse amplitude was increased. The splitting can

be used to extract the conversion factor between the signal amplitude ΔV at the AWG-output and Δ_{peaks} present at the structure. Here, the 100 mV provided at the top of the cryostat correspond to $\Delta_{\text{peaks}} \approx 8.5$ mV, which is compatible with a -20 dB attenuation at the 1 K-pot and an attenuation of approximately -3 dB due to the cables and the bias-tee. This is an indication that even though the AC-modulation was carried out with a repetition rate of $f = 100$ MHz in this measurement, the square pulse signal arrives almost unperturbed at the sample.

The latter finding is compatible with the prediction made earlier about the negligible influence of series impedances R_{setup} in the system. As an upper boundary for R_{setup} we therefore find a value of $\approx 200\ \Omega$ (see Appendix B) for the present device.

Another characterization measurement for the setup is shown in Fig. 7.6 (c) were the frequency response of the peak spacing Δ_{peaks} is probed. The applied square pulse was symmetric and had an amplitude of $\Delta V = 40$ mV. The peak spacing varies between 6 mV and 4 mV as the excitation frequency is increased from $f = 5$ MHz to 100 MHz. Such a modulation is most likely related to standing waves forming inside the cryostat along the coaxial cables connecting the contacts on top of the cryostats with the sample holder. As a frequency of 100 MHz corresponds to a wavelength of $\lambda = c/f = 3$ m, this explanation is well conceivable.

In order to probe the time evolution of electronic states on the nanosecond time scale it is conducive to change the pulse shape. In Fig. 7.6 (d) the system spent nominally only $t_1 = 1$ ns in the lower lying energy level and $t_2 = 9$ ns in the upper. As expected, the peak amplitude resembles the contribution to transport each level makes and is therefore strongly reduced for the shorter populated level.

A closer look at the peak amplitude as a function of dwell time is instructive and provided in Fig. 7.7. For the analysis, the peak pair displayed in Fig. 7.7 (a) was examined. It is well visible that one resonance grows at the expense of the other as a function of t_1. The peak for the respective shortest dwell time (marked by black arrows) is shifted towards the center of the gap. We will discuss this finding shortly and for now take the amplitude values at the two relative maxima of each trace. Two peak pairs were evaluated in this way and shown in Fig. 7.7 (b) - one at -0.5 mV and another at 0.5 mV. The current amplitude depends almost linearly on t_1 in this regime indicating constant current flow. For the lowest dwell times, however, the current values seem to level off and an extrapolation to 0 and 10 ns would still yield a finite current. Such a behavior is unphysical and indicates a constraint given by the setup.

To investigate this fact further we go back to the pulse amplitude dependence in Fig. 7.6 (d). In comparison to the symmetric case, it gets apparent that the peaks do not drift apart as much as expected. Namely, the spacing is reduced by a factor of two. An analysis of the peak spacing as a function of the parameter t_1 (characterizing the pulse shape) is shown in Fig. 7.7 (c). The distance between three peak pairs were investigated for this graph all being excited by a 100 mV pulse amplitude. Between $t_1 = 2$ ns and 8 ns the desired splitting $\Delta_{\text{peaks}} \approx 7.1$ mV

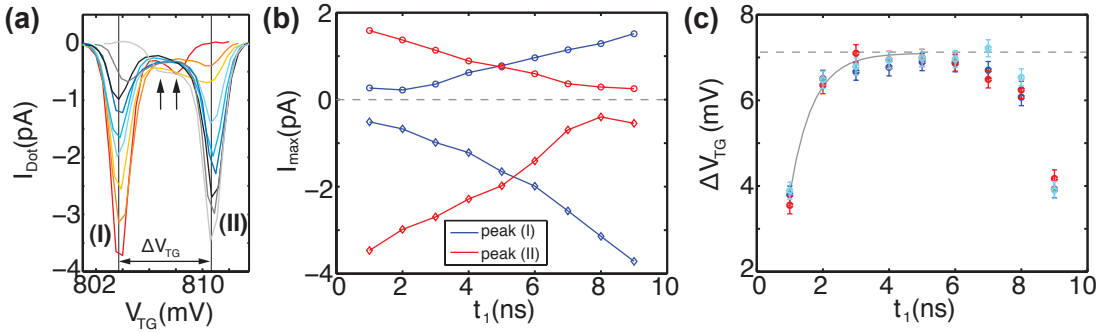

Figure 7.7: (a) Coulomb resonance split by a ΔV = 100 mV voltage pulse with modulation frequency was f = 100 MHz. The dwell time t_1 was tuned from 1 to 9 ns for the grey to the red trace. The black arrows mark the peak position for the lower peak for t_1 = 1 and 9 ns. (b) Peak amplitudes for peak (I) and (II) marked in (a) extracted for V_{bias} = -0.5 mV (diamonds) and V_{bias} = 0.5 mV (circles). (c) Determined peak spacing as a function of pulse shape for the Coulomb resonances in (a) at V_{bias} = -1 mV (dark blue), -0.5 mV (red) and 0.5 mV (light blue). The grey dashed line indicates the ideally achieved Δ_{peaks} due to 13 dB attenuation at the sample. A fit to the data assuming a single exponential function is shown as the grey solid line.

(marked by the grey dashed line) is achieved satisfactorily. As the dwell time for one voltage level is less than 2 ns, however, the amplitude breaks down indicating the deteriorated pulse quality. Fitting the saturation curve to an exponential function of the form $(\Delta_{\mathrm{peaks,ideal}} - \alpha \cdot \exp(-t_1/t_{\mathrm{rise}}))$, with the free parameters α and t_{rise}, enables us to determine the rise time of the system to be $t_{\mathrm{rise}} \approx 0.7$ ns. Since the rise time specified for the AWG is < 1.5 ns, the value found here can well be explained by this instrument limitation and has to be considered for future experiments. Due to the reduced peak separation, an overlap is likely which may contribute to the previously observed current saturation for low dwell times.

Measurements summarizing the above observations are shown in Fig. 7.8 (a)-(d). The finite-bias spectroscopy was carried out without AC-modulation of the top gate as well as with voltage pulses of different shapes applied to the gate. For the measurements in which the gate is pulsed a doubling of the Coulomb diamonds is observed. In Fig. 7.8 (a)-(d), the two newly arising peaks are visible at the touching points of the small and the big diamonds. For asymmetric pulse shapes like in Fig. 7.8 (c) and (d) the small pinched off region in the center merges once either with the lower or the upper diamond (see black arrows), which represents the amplitude dependence discussed in Fig. 7.7 (b).

Although the pinched off region is not well pronounced for the smaller diamond, a number of resonances emerge for negative bias indicating the single particle spec-

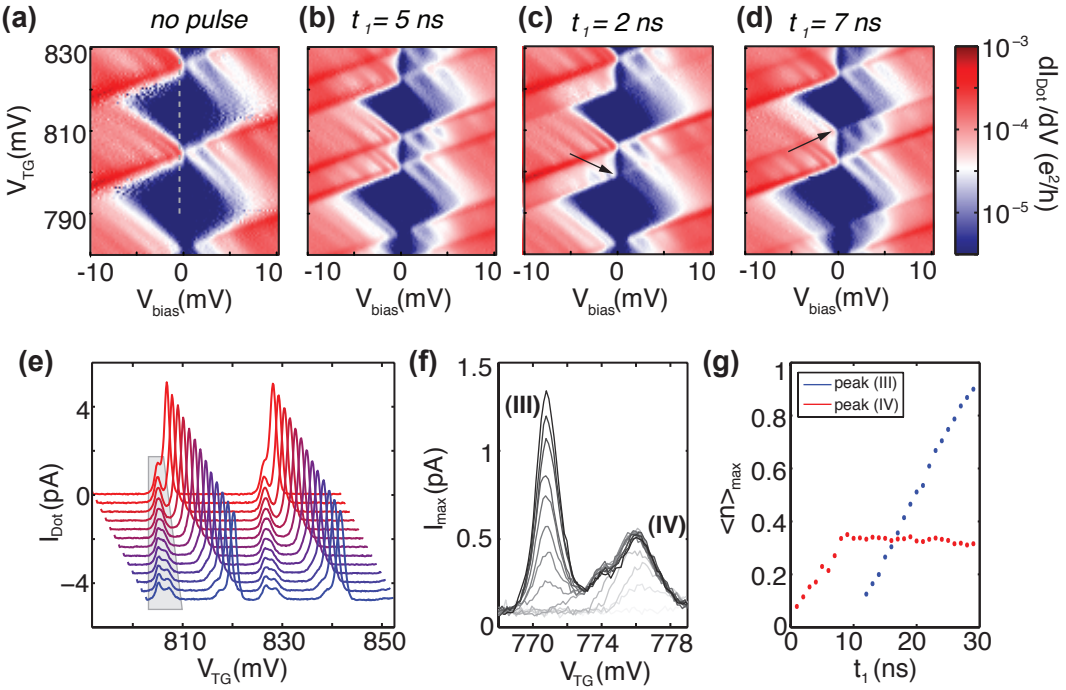

Figure 7.8: (a)-(d) Finite bias spectroscopy with (a) only DC-voltage at top gate and (b)-(c) AC-modulation with square pulses of ΔV = 100 mV amplitude and f = 100 MHz frequency. The dwell times t_1 are changed to achieve a symmetric (5 ns) or asymmetric (2 ns and 7 ns) pulse shape. (e) Increasing ΔV from 20 mV (uppermost trace) to 140 mV (lowermost trace) for a cut at V_{bias} = -0.55 mV (grey dashed line in (a)). The modulation frequency is 10 MHz and t_1 = 20 ns. The curves are vertically and horizontally offset for clarity. (f) Detailed measurement of peak pair marked in (e) as a function of dwell time. Light to dark curve correspond to t_1 = 1 ns to 28 ns. Constant parameters were f = 10 MHz and ΔV = 325 mV. (g) Average number of charge carriers per cycle <n> as a function of t_1 extracted from peak maxima for peak pair in (f).

trum. The single particle level spacing is Δ_{s} = 1.2 meV for the first observed state. This value fits well to the one expected for bilayer graphene being $\Delta_{\mathrm{s}} = \hbar^2/(m^* \cdot r^2) \approx$ 1 meV assuming an effective mass of m^* = 0.03 m_{e} [124] and a radius r = 50 nm for the QD. The second excited state that is detected in the experiment is separated by Δ_{s}' = 2.6 meV from the next lower lying one. The doubled energy spacing likely originates from a weak coupling to the second excited state and thus a good visibility only for the first and third level of the single particle spectrum.

In order to get these states into the the investigated voltage window, we choose a constant bias voltage $\Delta_{\mathrm{s}} > V_{\mathrm{bias}}$ = -0.55 mV and increase the pulse amplitude

ΔV stepwise at a fixed frequency $f = 10$ MHz, $t_1 = 20$ ns (see Fig. 7.8 (e)). As the peaks split, indeed a new peak evolves at slightly higher energies than the lower split-off resonance as is visible for the peak pair marked by the grey box in Fig. 7.8 (e). Striking is however, that the distance between the main resonance and the sub-peak is linearly dependent on the pulse amplitude. Since there is no obvious reason for the single particle spectrum to be influenced by the pulse height or shape, we cannot attribute the additional peak to an excited state with certainty.

Further information about this new state is obtained by analyzing the transmission amplitude as a function of dwell time as it was done for Fig. 7.7 (b). To increase the visibility of the two peaks, a pulse height of $\Delta V = 325$ mV was applied at $f = 10$ MHz. The duty cycle was stepped from 1 to 99% after each recorded top gate trace. In contrast to the earlier observation for the amplitude evolution of two main resonances, here, both sub-peaks gain in height (Fig. 7.8 (f)) as t_1 is increased. Such a behavior is expected for energy levels belonging to the same ground state. The number of electrons <n> transported through the structure per pulse cycle is shown in Fig. 7.8 (g). Whereas a monotonous increase is observed for the main resonance (peak (III)), the current through the additional resonance saturates at $t_1 \approx 10$ ns. For larger dwell times up to 99 ns, a constant current of 0.4 electrons per cycle is transferred from source to drain. The threshold at which a kink is observed, sets an upper boundary for the decay time of the higher state into the lower one and hence a decay rate $\Gamma_\mathrm{d} \approx 100$ MHz. This value is high compared to the maximum tunneling rate $\Gamma_\mathrm{tot} \approx 40$ MHz through the dot observed for the lower resonance.

Although the overall behavior may indicate that transient current through an excited state is probed for low dwell times, a number of features speak against this hypothesis. Firstly, the increasing peak separation is not expected for quantum states as mentioned above. Furthermore, the saturation stemming from a transient current can be described by an exponential function of the form $(1-\exp(-t_1/\tau_0))$, which is in contrast to the sharp kink exhibited in Fig. 7.8 (g). Another observation is the fact that the stable current given by peak (III) sets in only at the point at which the second current trace is saturated. The arguments brought forward point towards a somewhat distorted square pulse imposed on the gate. Reflections in the system are likely to induce such a double peak spectrum. With the recorded data it is, at that point, delicate to distinguish between measurement artifacts and features originating from the device.

7.7 Conclusion

We have shown measurement of an etched bilayer graphene quantum dot. A top gate finger, located above the island enabled us to tune the dot levels. We found the dielectric material Cytop$^{\mathrm{TM}}$ to be remarkably stable also at cryogenic temperatures.

The evolution of Coulomb peaks was recorded as a function of an applied elec-

tric field as well as for an external magnetic field. Although a potential difference between the graphene layers was introduced by the E-field, no band gap was detected in the spectra. Further, the results obtained from the measurements in a magnetic field were found to be qualitatively different from the B-field characteristics exhibited by single layer QDs. Both measurements also showed a deviation from predictions made by numerical simulations. As discussed, potential fluctuations in the bulk or introduced at the edges of the structure are present and may cause the discrepancy. It remains to be shown whether this limitation is inherent for etched structures due to a dominating edge contribution or whether it can be overcome by decreasing the effect of the substrate on the bulk disorder.

The high frequency measurements presented here demonstrate the possibility of pulsed gate experiments in graphene. One of the future prospect is to use transient current spectroscopy to determine coherence times of electronic states. In order to accomplish this goal, either the probing frequencies need to be increased or the characteristic time scales for the state dynamics need to be lowered. The former request can be fulfilled since the setup is suited for a bandwidth up to several 100 MHz as has been shown in Ref. 123. It remains an open question though, how the capacitively coupled back gate may affect the signal at higher frequencies. To overcome the latter issue, the realization of highly tunable tunneling barriers that allow for the adjustment of the decay rates to source and drain and the internal decay between dot states is desirable.

Chapter 8

Confinement in double gated bilayer graphene

In the quest for fabricating graphene nanostructures with low edge disorder, an obvious step is to exploit the fact that a band gap can be induced in bilayer graphene. In analogy to nanostructures in conventional semiconductor 2DEGs, charge carriers can therefore be depleted locally and conductive regions can be defined electrostatically. In this chapter we present data taken on a double gated bilayer graphene device, which showed signatures of electrostatic charge carrier confinement.

8.1 Sample and measurement setup

We employ split gates to form a narrow conductive channel connecting two reservoirs in a bilayer graphene flake. Contrary to conventional 2DEGs, an additional dielectric layer is needed to separate the graphene from the top gate electrodes. Hexagonal boron nitride has been proven to be an excellent insulator with breakdown fields on the order of $E_{\mathrm{break}} = 0.7$ V/nm [44]. Further, dangling bonds and charge traps are quasi absent in this single crystalline material. Like for graphene, its atoms are arranged in a honeycomb pattern with a lattice constant only 1.7% mismatched to graphene [125]. Also, the energies of surface optical phonons are twice as large as the ones in SiO_2 [31], implying that perturbations due to phonons are suppressed beyond cryogenic temperatures. Indeed it has been demonstrated that the induced disorder is very low for BN as compared to amorphous SiO_2 [31, 63].

The structure investigated here was located on the same flake as the one introduced in chapter 3 and the fabrication details can be found there (chapter 3.1) and in appendix C. In Fig. 8.1 (a) the measured device is depicted in an AFM image. For the constriction (marked with the solid red line), the gates are $L = 0.9$ μm long in transport direction and the opening between them is $W_{\mathrm{ch}} = 80$ nm wide.

With standard techniques we recorded the voltage drop induced by a constant current bias. For this purpose, we connected a large resistance ($R \geq 1$ MΩ) to a lock-in amplifier voltage output by which a current was generated. The voltage drop

was then determined from the signal that was fed back to the lock-in amplifier input. Besides, we measured the change of resistance by modulating the gates with a small AC signal with frequency $f < 100$ Hz superimposed onto the DC bias voltage V_{TG}. With a lock-in amplifier we then detected the transport signal at the same frequency f and obtained the transconductance $\partial R/\partial V_{\mathrm{TG}}$.

If not stated otherwise, the measurements were carried out in a variable temperature insert at the base temperature of $T \approx 1.7$ K.

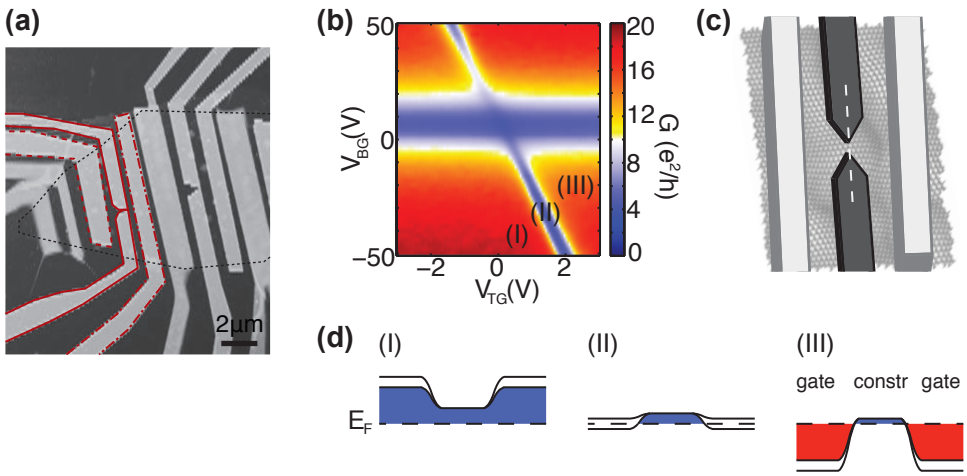

Figure 8.1: (a) AFM image of the bilayer graphene device. The black dotted line outlines the graphene flake, the red solid line indicates the split gate structure considered in this chapter. The other two marked gates are discussed in Sec. 8.4. (b) Conductance map for split gates as a function of applied back gate and top gate voltage recorded in a three point configuration with 1 nA current bias. (c) Sketch of split gate configuration (d) Energy band alignment for three cases marked in (b) along the cut indicated in (c) with the white dashed line.

8.2 Sample characterization

A two-dimensional conductance map of the complete gate range is shown in Fig. 8.1 (b). Two lines of lowered G divide the plane into four sections, which possess different doping levels in adjacent device areas. Tuning the back gate voltage from negative to positive values results in the cross-over from hole to electron transport in the region of the device that is not covered by a top gate. This gate dependence manifests itself as the horizontal bar of reduced conductance in Fig. 8.1 (b). Therefore, we attribute the lower part of the graph to a p-doped ungated region and the upper part to n-doping. Similarly, the diagonal line of low G indicates the position of charge neutrality in the double gated regions.

It is instructive to sketch the band alignment for some gate configurations as is done in Fig. 8.1 (d). We look at real-space cuts along the dashed line indicated in Fig. 8.1 (c) at the positions in gate voltage space marked in panel (b) of the same figure with roman numbers. In the channel, the Fermi energy E_F is located in the valence band for all three cases, since it is influenced only weakly by the applied top gate voltage. In contrast, the outer sections of the band diagrams are tuned strongly by top and back gates and change their doping polarization between (I) and (III) from p-type to n-type. In case (I) the doping arrangement is p-p'-p, meaning that only holes contribute to transport and no lateral confinement is expected. As the graphene underneath the TG is depleted in case (II), charge carriers are forced to be transmitted through the channel. Case (III) enables transport in the gated region again, although current is carried by electrons in this configuration and a bipolar n-p'-n junction is formed. Before looking more closely into the transport data at the transition from the p-p'-p to n-p'-n alignment, we compare the data of Fig. 8.1 (b) to a simple model that helps to understand the constituent features of this plot.

8.3 Simulation with resistor network

In a simple picture the device can be described as a network of resistors that determines the transmission from source to drain contact. As depicted in Fig. 8.2 (a), we identify three contributions to the total resistance. The parallel arrangement of the resistance R_gate of the areas underneath the TGs and the resistance of the channel, R_constr, is connected in series to the resistance R_bulk of the ungated regions. We choose to express the transmission in terms of the total conductance G_tot

$$G_\mathrm{tot} = \left(\frac{1}{G_\mathrm{bulk}} + (G_\mathrm{gate} + G_\mathrm{constr})^{-1} \right)^{-1}. \tag{8.1}$$

In the following, we determine each of these conductance contributions and combine them in the last step to obtain G_tot. The values used for this simulation are listed in Tab. 8.1. We model the bulk conductance with the help of Drude's theory and the parallel plate capacitor assumption. As we have found in chapter 3, this transport model breaks down for densities below a threshold value n_sat. We include this saturation value into the total charge carrier density n_tot and obtain [126]

$$n_\mathrm{tot} = \sqrt{n_\mathrm{C}^2 + n_\mathrm{sat}^2} = \sqrt{\left(\frac{\epsilon_0 \epsilon_{\mathrm{SiO_2}}}{e d_{\mathrm{SiO_2}}} \cdot \Delta V_\mathrm{BG} \right)^2 + n_\mathrm{sat}^2}, \tag{8.2}$$

where n_C is the density induced by the field effect from the back gate (see chapter 3 for more details). The bulk conductance is then given by

$$G_\mathrm{bulk} = \left(R_\mathrm{contact} + \left(n_\mathrm{tot} \mu e \left(\frac{W}{L} \right)_\mathrm{bulk} \right)^{-1} \right)^{-1}, \tag{8.3}$$

with R_{contact} being a constant contact resistance, since three point measurements were carried out, μ being the charge carrier mobility and $(W/L)_{\text{bulk}}$ being the ratio between width and length of the ungated device area. Figure 8.2 (b) shows the resulting conductance map considering only the bulk part of the sample. As expected, the conductance exhibits a minimum at a specific back gate voltage, indicating the electron-hole cross-over. The shift of this minimum value away from zero is introduced to the model to compensate for excess doping recorded in the experimental data.

The conductance underneath the top gates is determined by the Drude conductivity, which gets reduced by the opening of a band gap around the charge neutrality point. We write G_{gate} as follows

$$G_{\text{gate}} = G_0 \cdot \exp\left(-\frac{E_{\text{gap}}}{2k_{\text{B}}T}\right) = \left(n_{\text{tot,gate}}\,\mu\,e\left(\frac{W}{L}\right)_{\text{gate}}\right) \cdot \exp\left(-\frac{E_{\text{gap}}}{2k_{\text{B}}T}\right), \tag{8.4}$$

where the first term on the right hand side expresses the transport due to the charge carrier density $n_{\text{tot,gate}} = \sqrt{n_{\text{C,gate}}^2 + n_{\text{sat}}^2}$. Here, the density $n_{\text{C,gate}}$ is induced by the field effect from both the back gate and the top gate and n_{sat} is the saturation density as introduced in chapter 3. This conductance G_0 is suppressed in the presence of a band gap according to the exponential term in Eq. (8.4) with E_{gap} being the displacement field dependent size of the band gap as determined from tight-binding calculations [15]. As verified in Fig. 8.2 (c), the transmission is more and more reduced around the charge neutrality point as the displacement field is increased. It should be noted that G_{gate} can be mirrored at the CNP as a function of n but is not symmetric along the V_{TG} axis. This effect gets more pronounced for larger E_{gap} values.

As the last contribution, the conductance through the channel is to be modeled. Here, we assume diffusive transport to happen in the short constriction. This assumption is somewhat against the transport mechanism hoped for, which would be via discrete modes. In such a system, quantized conductance would be observed through the channel and the transmission would be suppressed completely for the lowest densities. However, in the present split gate device the confinement to a narrow channel is provided only at a finite displacement field, whose value we do not know. To simplify the model, we therefore take the conductance value given by the Drude model for the complete gate range. For small displacement values, this is a good approximation and we will later comment on the difference of the results obtained at high D-fields for the diffusive and the ballistic case. The equation describing the conductance G_{constr} reads

$$G_{\text{constr}} = n_{\text{tot,constr}}\,\mu\,e\left(\frac{W}{L}\right)_{\text{constr}}, \tag{8.5}$$

where $n_{\text{tot,constr}}$ is defined by Eq. (8.2). The corresponding conductance map is

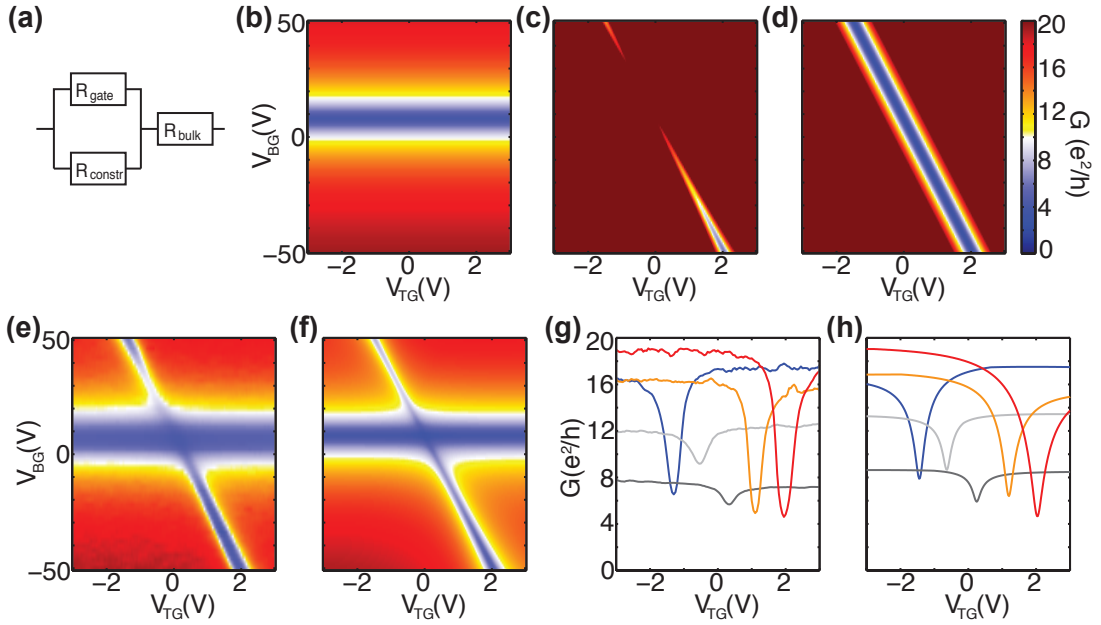

Figure 8.2: (a) Sketch of considered resistor network. Simulated conductance maps for (b) bulk conductance G_{bulk}, (c) conductance underneath top gates G_{gate} and (d) conductance through channel G_{constr}. (e) Measured conductance map (same as Fig. 8.1 (b)). (f) Simulated conductance map according to Eq. (8.1). For details on the model and parameters used, see text. (g) Cuts in (e) at constant V_{BG} = -50 V, -26 V, 0 V, 26 V, 50 V. (h) Cuts in (f) at same V_{BG} values as in (g).

shown in Fig. 8.2 (d) exhibiting conductance values independent of the displacement field, as expected.

We now insert the conductances G_{bulk}, G_{gate} and G_{constr} into Eq. (8.1). With the parameter set used here (see Tab. 8.1), we find, however, a large discrepancy between measurement and simulation. The only quantity not directly provided by the device properties and the measured data, is the value for E_{gap}. And indeed, if we reduce the theoretically expected band gap E_{gap} by a reduction factor S_{red} = 380, the experimental data can be resembled well. In transport measurements on bilayer graphene, the effectively detected size of the band gap has commonly been drastically lower than the one predicted [42, 43] and the introduction of S_{red} is therefore motivated empirically.

The lower row of Fig. 8.2 allows for a direct comparison of measurement ((e) and (g)) and simulation ((f) and (h)). Obviously, the model captures the main features of the data rather well, indicating that the magnitude of the considered parameters was extracted correctly. In the graphs displaying cuts at constant V_{BG} (Fig. 8.2 (g) and (h)), the slight asymmetry of the conductance dips originates from G_{gate}. Combined with the finding, that the conductance decreases as a function of the

parameter	value	parameter	value
$(W/L)_{\text{bulk}}$	1.5	$(W/L)_{\text{gate}}$	8
W_{ch}	80 nm	$\alpha_{\text{TG/BG}}$	28.5
R_{contact}	1.1 kΩ		
μ	4000 cm^2/Vs	n_{sat}	$2{\cdot}10^{11}$ cm^{-2}
$V_{\text{BG,D}}$	8 V	$V_{\text{BG,Dis}}$	30 V
S_{red}	380		

Table 8.1: List of parameters used for simulation. Symbols are introduced in the text except for $V_{\text{BG,D}}$, the offset of the CNP in V_{BG} for the ungated part, and $V_{\text{BG,Dis}}$, the saddle point of the resistance maximum along the displacement axis in V_{BG}.

displacement field, the presence of a (small) band gap is suggested and its value of $E_{\text{gap}} \approx 1$ meV at the maximum displacement field is in good agreement with other experiments (e.g. in chapter 3).

Next, we discuss the influence of the transport mechanism inside the channel. In order to make the simulation converge towards the experimental data, the asymmetry induced by G_{gate} needs to be suppressed. Since the two parallel conductances are competing in Eq. (8.1), for low densities either G_{constr} or G_{gate} will be dominant. At high displacement fields, where a band gap is potentially confining charge carriers to a narrow channel, transport may be ballistic. Under these conditions, the conductance in the channel increases quickly as the density is tuned away from the CNP and transport takes place through the channel. As a consequence, the over-all conductance is raised quickly as well. In the diffusive limit, the conductance is a slowly varying function of the density and the conductance underneath the gates stays relevant up to higher densities as compared to the ballistic case. To suppress the asymmetry, the reduction factor needs to be larger for the diffusive channel. For the ballistic case, we extracted the band gap to be reduced by $S_{\text{red}} = 250$ corresponding to a band gap of $E_{\text{gap}} \approx 1.5$ meV at maximum displacement field. The comparison to the values obtained for the diffusive regime shows that the result of the simulation is rather robust against the choice of transport characteristics inside the channel as long as the band gap is on the order of few meV.

In conclusion, simulating transport through the device with a resistor network enabled us to get an estimate for the size of the band gap, which is opened underneath the split gates. The obtained value is in line with that extracted in previous measurements (see chapter 3) and indicates that transport in the gated areas is never blocked completely. It gets apparent from the comparison of the maximal achievable resistances in the three regions, that they are all of the same order of magnitude. Namely, we extract $R_{\text{bulk,max}} = 8$ kΩ and $R_{\text{gate,max}} = 12$ or 6 kΩ and $R_{\text{channel,max}} = 4$ or 10 kΩ for the ballistic and the diffusive case, respectively. This

finding raises doubts in whether transport can be strongly modified by electrostatics in the present system. Later we will look more closely into the features exhibited by the recorded transport data.

8.4 Comparison of different geometries

The discussion of the foregoing section showed that transport is not strictly confined to the narrow opening between the split gates. However, the transmission below the top gate is significantly reduced at high layer asymmetry and most likely governed by variable range hopping in two dimensions, as we found in chapter 3.3.2. In the following, we present a comparison of different devices that were all located on the same flake. We wish to understand in which way the shape of the gate structure influences the transport properties. For all devices we looked at a zoom into the negative displacement range of a two-dimensional conductance map in the back gate - top gate plane, where we expect the transition from a unipolar (p-p'-p) to a bipolar (n-p'-n) junction.

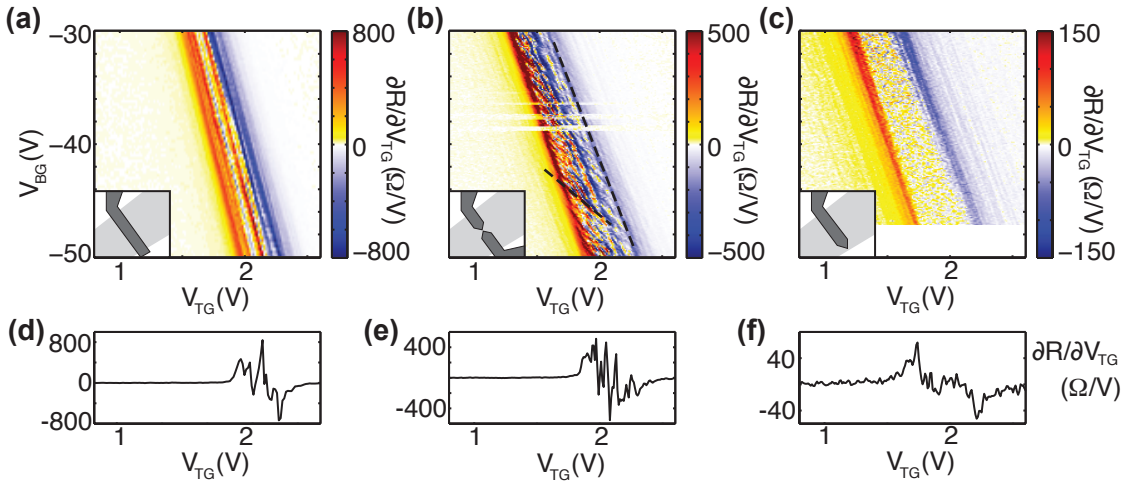

Figure 8.3: Transconductance maps for (a) full barrier (dashed-dotted outline in Fig. 8.1 (a)), (b) split gates (solid outline in Fig. 8.1 (a)), (c) "half" barrier (dashed outline in Fig. 8.1 (a)). Sketches illustrate the respective geometry. (d) and (e) Cuts in the respective graph above at constant V_{BG} = -50 V. (f) Same as (d) but at V_{BG} = -47 V. The dashed lines in (b) are a guide to the eye for the two slopes discussed in the main text. The measurements were carried out in a dilution fridge at $T = 100$ mK. The current bias was 0.5 nA for all experiments and the modulation amplitude for the transconductance was $\Delta V_{AC} = 10$ mV.

First, a gate that completely spans the graphene flake without a gap was considered. In the transconductance plot in Fig. 8.3 (a) the region of suppressed

transmission is recognized by large relative resistance fluctuations. A number of resonances running parallel to the displacement axis is visible. Due to their relative lever arm in gate space, we can attribute these oscillations to features located underneath the top gates.

The transport characteristics are different in the sample where a narrow opening (W_{ch} = 80 nm) is present in the gate, as shown in Fig. 8.3 (b). Again, the transconductance signal shows oscillations resulting in lines running parallel to the displacement axis. The indicate that localized states in the gated areas contribute to transport. Additionally, plenty of resonances appear, which exhibit a considerably lower relative lever arm $\alpha_{\mathrm{TG/BG}}$ and are hence less strongly tuned by the top gates. Both slopes are marked in Fig. 8.3 (b) with dashed lines. The appearance of these features was observed in more than five split gate devices in total and is therefore believed to originate from the narrow opening. As the displacement field is lowered, first the newly observed resonances fade away at $D \approx$ -0.73 V/nm (not shown here), whereas those induced by localized states underneath the TGs remain down to $D \approx$ -0.4 V/nm. This finding indicates, that the charge carriers are more and more forced to pass through the channel as D is increased even though the confinement is imperfect.

Last, we show the transconductance signal of a gate that did not span the whole width of the flake but instead left a W_{ch} >150 nm wide ungated channel between the TG and the flake edge (see Fig. 8.3 (c)). In contrast to the previous two cases, no resonances are visible and the relative resistance changes $\Delta R/R$ are comparably small. This observation can be explained by the properties of nanoribbons studied in chapters 5 and 6. Unless transport is ballistic in such a wide ribbon, commonly, no difference to a bulk device is observed. The device discussed here does not fulfill the requirements for truly ballistic transport and hence, even if charge carriers were confined to the channel, the transmission would appear similar as for bulk. Further, in the region of lowered conductance, no resonances are observed parallel to the displacement axis, since transport takes place through the channel in all gate configurations, where localized states do not hamper the transmission.

From the presented comparison we can conclude that the gate structure does affect the transmission and that charge carriers are weakly confined to a narrow channel by top gates in the presence of a perpendicular electric field. The accuracy of this supposition was further investigated by modulating the two split gates individually, which will be presented in the following section.

8.5 Transport through the channel

8.5.1 Correlations between the transconductance of individual gates

To understand the contribution to transport made by each one of the two top gates, we measured their transconductances individually. For this purpose we superimposed the modulation voltage $\Delta V_{\mathrm{AC}} = 10$ mV to each of the gates at a different frequency ($f_{\mathrm{up}} = 71.0$ Hz and $f_{\mathrm{low}} = 13.3$ Hz) and detected the transconductance signal at the respective frequency. The results are shown in Fig. 8.4, where the upper row displays the data obtained for the upper TG and the lower one corresponds to the data recorded for the lower TG.

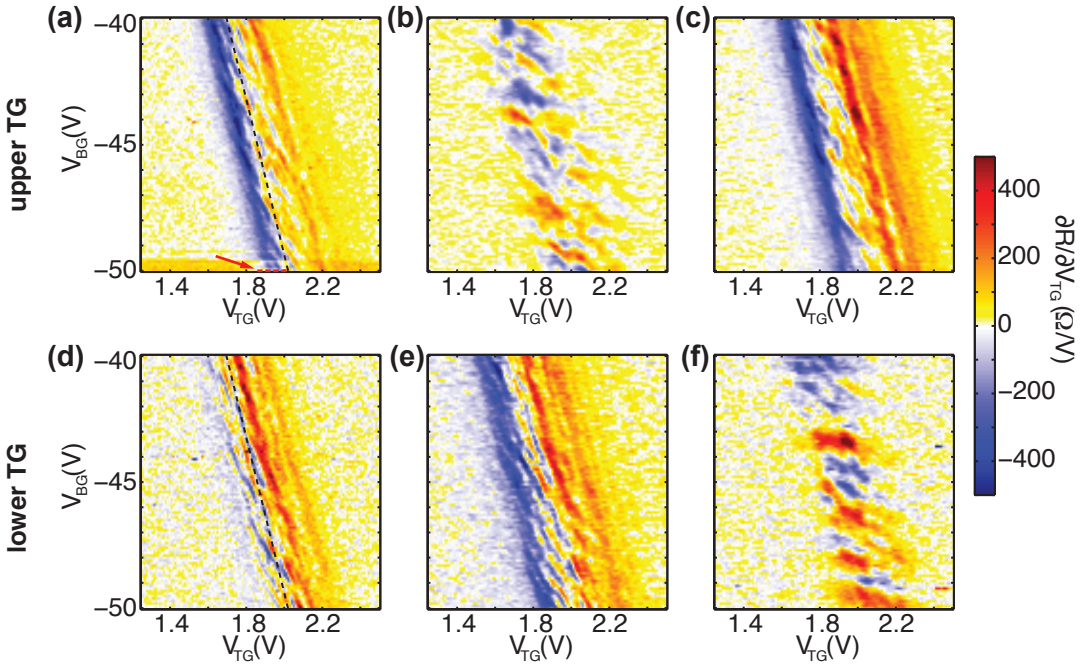

Figure 8.4: Transconductance maps for the individual TGs. Upper (lower) row is displaying the signal obtained by modulating the upper (lower) TG. (a) and (d): The DC voltage on both gates is swept simultaneously. The arrow in (a) indicates the position of the conductance traces of Fig. 8.6 and the black dashed lines in (a) and (d) show the line along which the TG is tuned for the measurements displayed in the 2$^{\mathrm{nd}}$ and 3$^{\mathrm{rd}}$ column. (b) and (e): DC voltage for upper TG kept at charge neutrality ($n = 0$), DC voltage for lower TG swept. (c) and (f) Same as second column but vice versa. The current bias was 0.5 nA for all experiments and the modulation amplitude for the transconductance was $\Delta V_{\mathrm{AC}} = 10$ mV.

In the measurements leading to the first column of Fig. 8.4, the DC voltage ap-

plied to the gates were swept simultaneously between 1.2 V and 2.5 V. The transconductance maps show similar features to the one observed in Fig. 8.3 (b), namely two sets of resonances - one with a steep slope and another one less strongly tuned by the TG. The fact that these latter oscillations appear for both gates, indicate that the corresponding physical origin is present in the vicinity of both gates. Since the relative lever arms are the same for the upper and the lower gate, we conclude that the coupling is equally strong.

For the data displayed in the second and third column of Fig. 8.4, only one of the top gate voltages was swept. The DC voltage for the other one was kept at the value, which, for the respective V_{BG}, corresponded to the position of the CNP (see dashed lines in Fig. 8.4 (a) and (d)). This means that its DC voltage was stepped along the displacement axis. As seen in Fig. 8.4 (c) and (e), for the gate below which the density is tuned, the transconductance resembles the same characteristic resonances as the data in the first column. Hence, as long as the transmission is limited below the upper (lower) gate, transport underneath the lower (upper) gate is governed by the same physics as in the case where both gates are tuned.

Although the DC voltage value applied to the upper and lower TG in Fig. 8.4 (b) and (f) is not changed along cuts at constant V_{BG}, a modulation of the transconductance signal is observed. For some gate ranges these modulations possibly possess the same lever arm as the resonances with the flat slope in Fig. 8.4 (a) and (d). This finding would clearly indicate, that the cause of these oscillations is located in-between the gates. However, due to the data quality, a strong statement is not possible at this point. Interestingly, the transconductance in Fig. 8.4 (b) and (f) is modulated along the V_{BG} axis. We assume that, depending on the gate configuration, the coupling from the bulk to transport channels under the TG is stronger or weaker, leading to fluctuations in $\partial R/\partial V_{\mathrm{TG}}$.

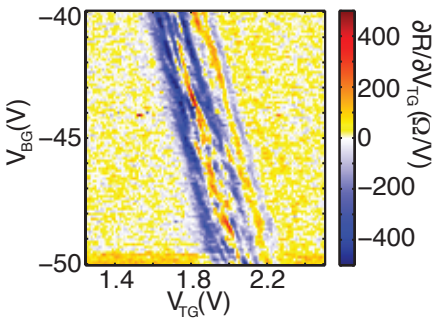

Figure 8.5: Interdependence between Fig. 8.4 (a) and (d) by subtracting one from the other to identify the origin of the observed oscillatory features in the transconductance signal.

Since the data of Fig. 8.4 (a) and (d) does not enable us to exclude a situation, where localized states are distributed along the edges of the gates, we show their interdependence in Fig. 8.5. By subtracting the two signals from each other, the oscillations running parallel to the displacement axis are maintained, whereas the other set cannot be distinguished well anymore. This correlation suggests that the probed physical origin is indeed the same for both split gates.

8.5.2 Possible transport mechanisms

We now focus on the set of oscillations, which we suspect to stem from the opening between the split gates. A number of mechanisms are conceivable to cause the observed transport features. Although transport through discrete modes leading to quantized conductance may play a role here, we will consider alternative explanations. Namely, resonant tunneling or Coulomb blockade through states inside the channel and universal conductance fluctuations in the leads would induce an oscillatory behavior as well.

Ballistic transport via transverse modes

Supposably, the resonances are caused by discrete modes in the channel. In an ideal ballistic graphene system, the conductance is given by $G_{\mathrm{constr}} = (4e^2/h) \cdot \frac{2W_{\mathrm{ch}}}{\lambda_{\mathrm{F}}}$, where λ_{F} is the Fermi wavelength and W_{ch} is the width of the channel. If indeed a quantum point contact with quantized conductance was formed, the observed oscillations in the transconductance data would indicate the position of the steps in G_{constr}. Furthermore, the integrated signal (integrated along the direction of the modulated gate to get the conductance) should show steps by the expected values. This is not the case for the recorded data.

Additionally, the present device exhibits a mean free path of $l_{\mathrm{mfp}} \lesssim 100$ nm in the density range where the resonances appear, meaning that the system is not fully ballistic. We can therefore exclude that these features are due to transport via discrete modes in the channel. The fact, that we do not observe any clear signature for quantized conductance in the measured DC data (see e.g. Fig. 8.6 (c)), further supports this conclusion. We therefore need to present alternative explanation for the experimental data.

Tunneling processes

Resonant tunneling: Potentially, the oscillations are the result of resonant tunneling through localized states in the constriction. In order to observe tunneling processes, the resistance of the tunneling barriers is required to exceed the resistance quantum $R_{\mathrm{T}} = h/e^2$. As apparent in the conductance trace displayed in Fig. 8.6 (c), the conductance never falls below $2e^2/h$. This finding allows for the exclusion of resonant tunneling as the transport mechanism as well

Coulomb blockade: If transport happens through localized sites that are only weakly coupled to the environment, Coulomb blockade can be recorded in the presence of electron-electron interactions. Since the requirement of tunneling barriers with large resistance ($R_{\mathrm{T}} > h/e^2$) is not fulfilled in the present device, we can apply the same argument as above and Coulomb blockade becomes an unlikely explanation for the observed features.

This is further supported by finite-bias spectroscopy which was carried out inside the region of suppressed conductance (see dashed line in Fig. 8.4 (a)). The conduc-

tance data was recorded at V_{BG} = -50 V as a function of V_{TG} and is shown in Fig. 8.6 (a) and (c). Although regions of lowered conductance are visible along the gate axis, Coulomb diamonds cannot be clearly distinguished and we can presumably exclude this mechanism.

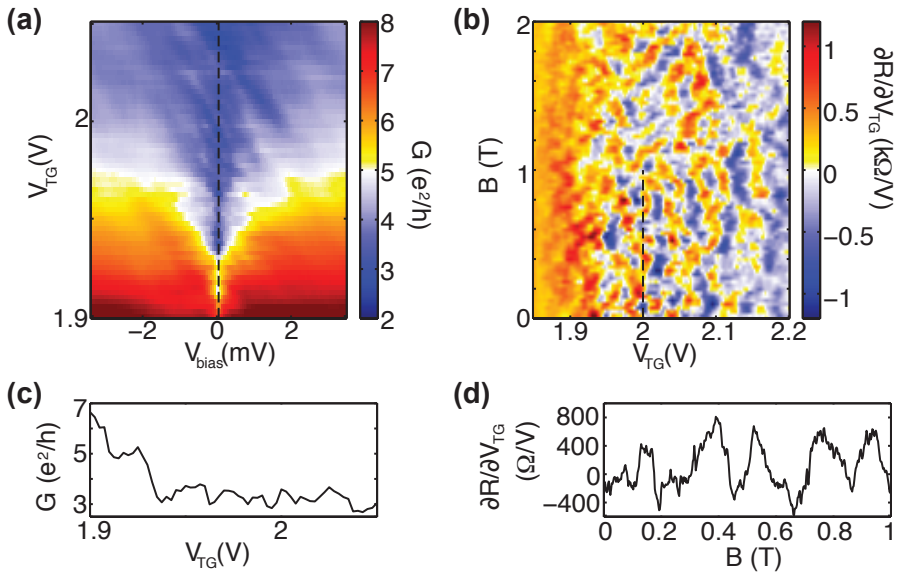

Figure 8.6: (a) Finite-bias spectroscopy as a function of V_{TG} taken at V_{BG} = -50 V. (c) Cut at $V_{\mathrm{bias}} = 0$ in (a). The conductance measurement was taken at T = 100 mK with standard lock-in techniques using an AC modulation voltage of 50 μV. (b) Transconductance map showing the B-field dependence of a TG trace taken at V_{BG} = -50 V. (d) Cut in (b) at the position indicated by the dashed line. The measurements were performed at T = 100 mK with a current bias of 0.5 nA and the modulation amplitude for the transconductance was ΔV_{AC} = 10 mV.

Universal conductance fluctuations

The fourth explanation we put forward, is the appearance of universal conductance fluctuations (UCF), which occur in open diffusive systems with conductances larger than the conductance quantum [127]. These originate from quantum interference of elastically scattered carriers moving along different paths, leading to a certain reflection amplitude. As the arrangement of scattering impurities in the system is changed, the total reflection changes and is found to induce a modulation of the detected conductance by $\Delta G = e^2/h$ [128]. Experimentally, uncorrelated impurity configurations can be achieved by a change in Fermi energy. UCF may hence be the cause of the oscillations we observe in the data of Fig. 8.3 (b) and Fig. 8.4.

Since interference effects are altered by an external perpendicular magnetic field, a correlation field can be identified from measurements of the conductance as a

function of B [129]. Figure 8.6 (b) shows the magnetic field dependence of the transconductance measured along the same gate configuration as Fig. 8.6 (a). The oscillations exhibit a quasiperiodic pattern typical for conductance fluctuations as a function of magnetic field (see Fig. 8.6 (d)). In cuts at constant V_{TG} (see Fig. 8.7 (d)), however, a characteristic quasi-period is observed. From its value, $\Delta B \approx 200$ mT, we can estimate the area covered by interfering paths to be $A = \left(\frac{h}{e}\right)/\Delta B \approx 150$ nm^2. Again, we find this length scale being comparable to the system size. It should be noted, that this is a lower bound for the covered area, since the correlation field is expected to be lower than the here determined ΔB. The amplitude of the conductance oscillation is $\Delta G \approx e^2/h$, which further implies the presence of universal conductance fluctuations in the system.

In conclusion, we find that the system is not in the Coulomb blockade regime. Further, the transmission via discrete modes and via resonant tunneling can be excluded with high confidence by the measurement data. It is however most likely that we probe universal conductance fluctuations of an area around the opening between the gates. Since the mean free path is on the order of the system size, the characteristics of the present device are located at the cross-over from ballistic to diffusive transport. Additionally, we cross over from an unconfined to a confined system as the band gap is opened. We may therefore even see signatures of more than one phenomenon in the recorded data.

8.6 Transport in a perpendicular magnetic field

Last, the influence of high magnetic fields is discussed based on Fig. 8.7. For this color plot, the transconductance for the same gate voltage range as discussed in the previous sections was recorded at $B = 0$ T (Fig. 8.7 (a)) and at B 13 T (Fig. 8.7 (b)). An obvious difference between the two cases is, that the gate range for which transconductance features are observed, is strongly confined to a diagonal line for $B = 0$ T. At finite magnetic field, the plot exhibits structure in the transconductance signal across the whole gate range. The over-all contrast is weaker for $B = 13$ T, indicating that the resistance changes are smoothened as compared to $B = 0$ T.

We first compare the set of oscillations exhibiting the steeper slope for zero and finite magnetic field. At $B = 0$ T, the transconductance oscillations show large amplitudes for low densities, which fade away as the density is increased. At high magnetic field, the oscillations are not discernable close to the charge neutrality point. In contrast, a number of lines running parallel to the displacement axis evolve for more negative V_{TG}. This regime corresponds to the case, where both the transport underneath the TGs and in the uncovered regions is governed by holes. Due to their appearance only at finite magnetic fields, we attribute these transconductance features to Shubnikov-de Haas oscillations tuned strongly by the TG. Strikingly, the oscillations are absent for the bipolar doping regime (right hand

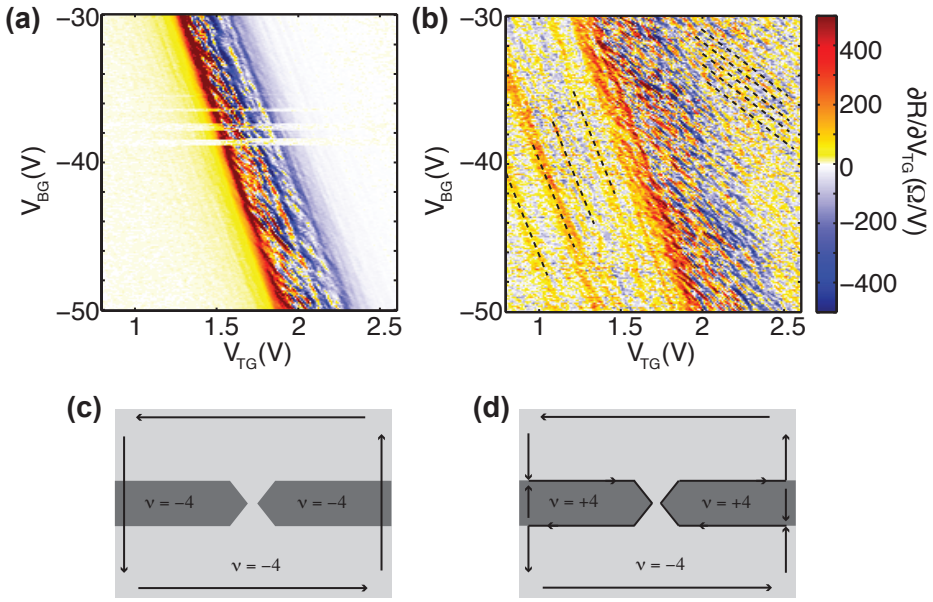

Figure 8.7: Transconductance maps at $B = 0$ T (a) and $B = 13$ T (b) with the measurement conditions as described in Fig. 8.3. (c) and (d) Sketch of edge channel configuration for the two regimes identified in (b). (c) For p-p'-p alignment and (d) for p-n'-p alignment between the ungated and the gated regions.

side of Fig. 8.7 (b)).

Looking at the second set of oscillations in this finite magnetic field measurement, we observe the contrary behavior. For the gate range in which a p-p'-p junction is formed, no signature of the channel between the split gates is visible. As the system exhibits a bipolar p-n'-p junction between the top-gated and the uncovered areas, oscillations are visible even away from the CNP. At such large density values the Fermi energy underneath the gates is tuned much above the band gap and hence transport is in principle not hindered in these areas. From this observation we can conclude, that the contribution of the features weakly tuned by the TGs is maintained at large carrier densities, if the doping exhibits opposite polarization in adjacent areas.

In the following, we suggest an explanation for the observed data based on the picture of quantum Hall edge channels following Ref. 130. In a sufficiently high externally applied magnetic field the density of states is concentrated in discrete Landau levels and transport is expected to happen along edge channels. In the present sample, the filling factor in the ungated region differs from the one underneath the TGs for certain gate configurations. As a consequence, the number of edge channels as well as their propagation direction may vary. Two explicit cases are depicted in Fig. 8.7 (c) and (d), for filling factor $\nu_{\mathrm{bulk}} = 4$ in the ungated regions and $\nu_{\mathrm{gate}} = \pm 4$

below the gates. In the case that the filling factors are the same in all regions (see Fig. 8.7 (c)), the edge states propagate along the boundaries of the graphene flake. Since it penetrates underneath the TG, the transconductance signal is sensitive to this part of the sample. In contrary, charge carriers travel along the edges of the top gates, if a p-n'-p junction is formed between the bulk and the gated area. As sketched in Fig. 8.7 (d), current flows through the narrow opening between the split gates. Consequently, the constriction influences the transconductance signal in this configuration.

It should be noted that this simple model breaks down for more than one edge channel. Since magnetoresistance measurements in the bulk part of the sample did not reveal filling factors higher than ± 4 clearly, we conclude that these are not fully developed in the present device. Under this assumption, the observation of two distinct regimes is conceivable.

8.7 Conclusion

In the presented measurements, we saw signatures for electrostatic confinement in a double gated bilayer graphene sheet. The limited tunability of the resistance underneath the top gates prevented, however, to fully pinch-off the current below the split gates. As a result, the recorded transport characteristics consist of contributions from the gates and the channel likewise. For finite magnetic fields, we find that the data can be explain well by the formation of bipolar p-n junctions at the interface between gated and ungated regions of the device.

Recent experiments on double gated suspended bilayer graphene devices demonstrated, that phenomena like Coulomb blockade and quantized conductance are observable in electrostatically defined structures [14]. These free standing devices exhibit typically excellent transport quality, implying a smooth potential landscape. Therefore, the induced band gap is less likely overcome by potential fluctuations and gated areas are depleted effectively.

Chapter 9

Conclusions and Outlook

In the course of this work, graphene was investigated with respect to its electronic properties. The performed experiments join a large number of studies conducted since graphene's discovery in 2004. Starting with the finger print of chiral particles, the first experiments verified this peculiar property by quantum Hall measurements [50, 131]. The present work started out at this point as well (see chapter 3) and then focused on the characteristic density of states in single layer graphene (see chapter 4). Contrary to theoretical predictions of a vanishing density of states at the charge neutrality point, the experimental results possessed a finite value for the DOS indicating the presence of disorder fluctuations in the system.

Strikingly, disorder induced localized states commonly played a dominant role in experiments probing electronic transport in graphene nanostructures. The absence of an energy gap in the dispersion relation of graphene poses a challenge for the patterning of electronic devices. Whereas conductive areas can be completely isolated from each other by etched trenches, tunneling barriers cannot be created that way. Since localized states lead to the formation of a transport gap in spatially confined systems, tunneling barriers were defined by narrow constrictions [12, 105, 132, 133]. A detailed discussion of the transport properties of such nanoribbons was presented in chapter 5 and 6. Besides extracting a scaling law for the number of charged islands in the system, nearest neighbor hopping was identified as the microscopic mechanism behind transport. Further, disorder induced at the edges as well as in the bulk were found to contribute to the formation of localized states.

Whereas single layer graphene attracted large interest during the first years of graphene research, lately, focus was brought more and more to bilayer graphene. Although the quasiparticles are no longer described by the Dirac equation for massless fermions in this material, most of the exceptional physical properties are maintained (e.g. the chirality and the large charge carrier mobility). The main advantage of bilayer graphene is the fact that an energy gap can be opened and tuned in the band structure by an electric field gradient perpendicular to the two sheets. Experiments on a top-gated bilayer graphene quantum dot were performed in quest of determining the location of the electron-hole cross-over in the energy spectrum unambiguously

(see chapter 7). The recorded data revealed, however, that the effective band gap in the system was small compared to the level spacing of the quantum dot and could hence not be used as an indicator for the charge neutrality point.

As the boundaries of graphene nanostructures are commonly suspected to induce a considerable amount of disorder, in chapter 8 we presented an approach to eliminate the edges and instead confine charge carriers in bilayer graphene electrostatically. The measurements showed, that carriers can indeed be directed to gate defined transport channels. Hence, the split gate technology is certainly promising for the patterning of bilayer graphene structures.

Most studies carried out in this thesis found a significant amplitude of density fluctuations in the graphene sheets. For the next experiments, it is desirable to reduce the limitations imposed to the sample quality due to this disorder in the system. Large improvements of the bulk transport properties were achieved recently by the removal or the replacement of the SiO_2 substrate material [31, 134]. Combining the application of single crystalline boron nitride as a substrate and the electrostatic confinement by split gates, should allow for the fabrication of devices with low disorder.

If such structures are in the ballistic transport regime, phenomena like conductance quantization and resonant tunneling can be investigated. Additionally, the controlled tunability of the barrier width of tunneling barriers would facilitate a large number of experiments that are challenging to be performed at present. Among these are time resolved measurements of the charge carrier transmission through quantum dots and pulsed gate experiments to determine relaxation times. Opening a band gap in bilayer graphene would facilitate the identification of the few electron regime and ease the understanding of the single particle level spectrum in quantum dots. With the implementation of this new generation of graphene devices, many of the questions that are left open at this point, can presumably be answered and extend the knowledge of the electronic properties of graphene.

Appendices

A 2D Mott variable range hopping

The theory developed by Mott [46] describes transport of charge carriers via discrete energy levels being randomly located in energy and space. It may be favorable for a charge carrier to cover a large distance in space (larger than to the nearest neighbor) if the energy expense required to reach it is small. From the optimized hopping rate between two localized sites, the conductivity through the sample is found to be

$$\sigma = \sigma_0 \exp\left[-\left(\frac{\Delta_0}{k_\mathrm{B}T}\right)^{1/3}\right],$$

where the characteristic energy Δ_0 is defined as

$$\Delta_0 = \frac{27}{\pi \mathcal{D}(E_\mathrm{F})\xi^2}.$$

Here, the density of states $\mathcal{D}(E_\mathrm{F})$ of bilayer graphene and the localization length ξ enter. For the density of states, the interlayer hopping energy γ_1 and the Fermi velocity v_F need to be known to get a value for

$$\mathcal{D}(E_\mathrm{F}) = \frac{\gamma_1}{\pi(\hbar v_\mathrm{F})^2}.$$

We take them to be $\gamma_1 = 0.39$ eV [23] and $v_\mathrm{F} = 10^6$ m/s [4] and find for the localization length

$$\xi = \sqrt{\frac{27}{\gamma_1 \Delta_0}} \cdot \hbar v_\mathrm{F}.$$

The optimum hopping distance is defined as

$$d_\mathrm{opt} = \left(\frac{\xi}{\pi \cdot \mathcal{D}(E_\mathrm{F}) \cdot k_\mathrm{B}T}\right)^{1/3}$$

and should be much smaller then the system dimension to make the model of variable range hopping conceivable as a transport mechanism.

B High frequency limitations

Large damping in high frequency setups is caused by capacitances that may short circuit the high frequency line to a reservoir. Together with the resistance of the line, the capacitance then forms an RC-filter, which dampens the applied signal. Here, we estimate the expected frequency response of such a filter supposably forming in the device presented in chapter 7 and determine some limits.

The capacitor is constituted by the metal electrode of the gate (including the bond pad) and the back gate. The size of its capacitance is therefore determined by the thickness of the SiO_2 separating the two plates, $d = 285$ nm, the dielectric constant of the oxide and the area A of the gate electrode.

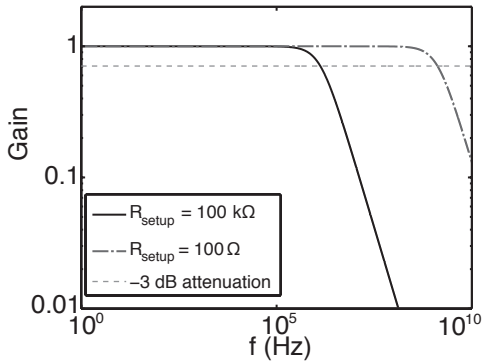

Figure B.1: Simulation of the frequency response of an RC-filter with parameters expected for the device discussed in chapter 7.

Since the RC-filter acts as a voltage divider, the output voltage V_{out} can be defined by the reactance X_{c} of the capacitor and the resistance R to be

$$V_{\text{out}} = V_{\text{in}} \cdot \frac{X_{\text{c}}}{\sqrt{R^2 + X_{\text{c}}^2}}.$$

The frequency dependence of the gain $V_{\text{out}}/V_{\text{in}}$ is plotted in Fig. B.1 for two different series resistances R_{setup} in the line assuming the area of the capacitor to be given by the bond pad, $A = (100 \times 100)\ \mu\text{m}^2$. The resistance is assumed to be $R_{\text{setup}} = 100\ \text{k}\Omega$ (solid line) and $R_{\text{setup}} = 100\ \Omega$ (dashed line).

The dotted line in Fig. B.1 indicates the value at which the input signal is attenuated by 3 dB. Where the gain curve intersects this threshold value, the cut-off frequency f_{c} of an RC-filter is defined. In the cases presented here, the values are $f_{\text{c}} \approx 1.4$ MHz for the high series resistance and $f_{\text{c}} \approx 1.4$ GHz for the small one, where the latter is compatible with the order of magnitude observed in chapter 7,. Assuming that $R_{\text{setup}} = 200\ \Omega$, the gain falls below the threshold at ≈ 750 MHz. For the case presented in chapter 7, the signal is still unperturbed for these frequencies and we can therefore infer that the resistance exhibited by the system has to be smaller than this critical value.

C Mechanical transfer process

In this work, hexagonal boron nitride (BN) was used as a dielectric for top-gated bilayer graphene devices. For this purpose, bilayer graphene was mechanically exfoliated, flakes were characterized and electrically contacted as described in chapter 3.1. A representative flake is shown in Fig. C.2 (e) and (f) before and after being contacted, respectively. For the positioning of a BN flake on top of this structure, we employ a transfer process, which has been developed by Dean et al. [31].

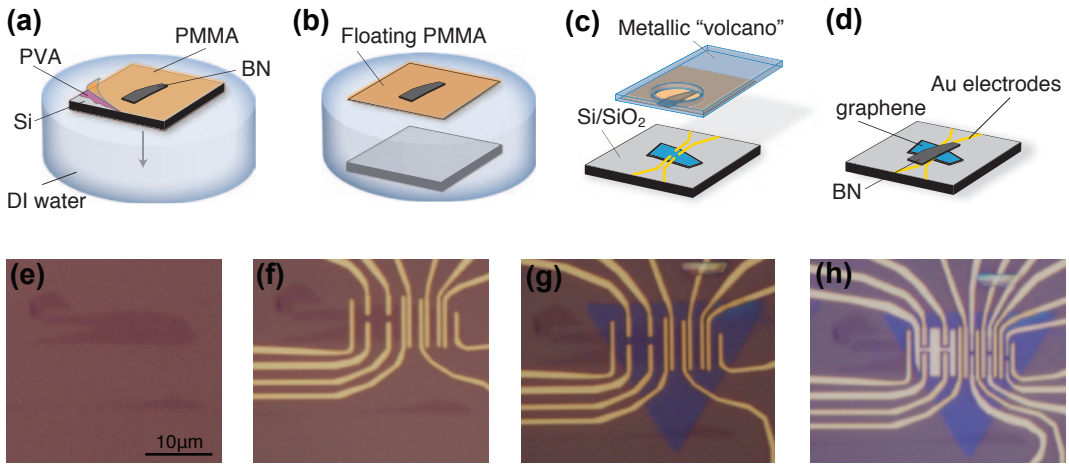

Figure C.2: Schematic of the transfer process. (a) Si chip covered with a stack of PVA and PMMA. Characterized BN flake lies on surface. (b) After PVA is etched away, Si chip sinks and PMMA remains floating on surface. (c) PMMA film is deposited on transfer slide, aligned with graphene structure and (d) brought in contact. (e) Optical image of a bare graphene flake on SiO_2 substrate. (f) After ohmic contacts were added. (g) After BN was deposited. (h) Final device with TG electrodes. (Figure (a) to (d) adapted from Ref. 31)

Transfer chips are prepared onto which BN is mechanically exfoliated. The substrate is Si (approx. 500 μm thick), which is spin coated with a layer of poly vinyl alcohol (PVA) solution (PVA 9000, 4.7% mass in DI water). After soft-baking at 100°C, a layer of PMMA (PMMA 950K 4:1 in chlorobenzene (CB)) is spun on top of this and soft-baked as well. The thickness of the complete polymer stack is tuned to be $\approx$ 300 nm, to which the PVA contributes with $\approx$ 100 nm. Since the dielectric constants of the polymers are comparable to that of SiO_2, the visibility of graphene and BN in an optical microscope is maintained.

Boron nitride flakes are characterized by their contrast in the optical microscope and AFM measurements. Flakes suitable for the application as TG dielectric should be 7−15 nm thick and exhibit a low surface roughness. Ideally the value measured in the AFM falls to the resolution limit of 0.1 nm.

For the transfer, the position of the BN flake chosen is indicated on the transfer chip with the help of small blue tape pointers and the polymer is scratched away along the edges of the transfer chip. By this, the etching of the PVA in the next process step is facilitated. For the PMMA release, a beaker is filled with DI water (ca. 5 mm high) and the transfer chip is placed on the water surface. As the water penetrates at the edges of the chip, it dissolves the PVA layer (see Fig. C.2 (a)) and finally separates the Si from the PMMA. Whereas the former sinks to the bottom of the beaker, the latter remains floating at the water surface as is shown in Fig. C.2 (b). Subsequently, the beaker is carefully filled with DI water up to the rim.

The device used to handle the PMMA film during the transfer is a metallic slide, which has a cone-shaped attachment on one side. A hole of $\approx$ 2 mm diameter is positioned in the center of this cone, penetrating through the metal slide as well. Due to its shape, this device was termed "volcano".

As the next step in the transfer, the PMMA film is adhered to this volcano and the position of the BN flake is verified to be in the center of the hole by means of optical microscope. To dry the back side of the polymer film, the slide is then placed on a hot plate ($T = 70°C$) for 10−15 min until all water droplets are evaporated.

Consequently, the volcano is mounted on the arm of a micro manipulator, which is combined with an optical microscope (Olympus BX-FLA). The target Si/SiO_2 chip is placed below on a heatable table. To avoid the formation of a water layer on the target structure, this table is heated to 100−120°C during the alignment process. With the help of the optical microscope, the BN flake on the PMMA film is positioned above the graphene flake and brought in contact by simply lowering the film to the SiO_2 surface. After adhesion is established, the micro manipulator arm is left in its position for 5−10 min and the elevated temperature of the target chip helps to relax folds in the PMMA.

Finally, the chip is unmounted and the PMMA is removed in warm acetone. The BN is strongly attached to the surface and stays in place as it is shown in Fig. C.2 (g). As the achieved lateral accuracy of this positioning method is ± 5 μm, sufficiently large BN flakes are required. After the transfer, TG electrodes can be fabricated by means of standard EBL and metal deposition. In Fig. C.2 (h) a final device is displayed, which features a number of top gates.

D Local oxidation of graphene

One of the main results of chapters 5, 6 and 7 was, that a number of localized states are forming in etched nanostructures that affect transport considerably. A possible origin of these states is the presence of rough edges as a result of the etching process. Hence, an alternative method to structure graphene would be desirable that imposes a smooth confinement potential on charge carriers. The local modification of the graphene lattice might allow to pattern graphene flakes on the nanoscale.

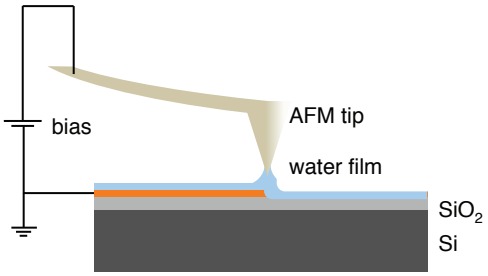

Figure D.3: Working principle of AFM lithography sketched using the example of a graphene device. An applied voltage bias between tip and graphene sheet (orange region) initiates an oxidation process of the latter.

The principle

A well established method to structure GaAs heterostructures is the so called AFM lithography. The working principle is depicted in Fig. D.3. In ambient conditions, the surface of the chip to be patterned is covered with a thin layer of water. A conductive AFM tip is brought close to the surface and a bias voltage is applied between the tip and the sample. The energy provided thereby is sufficient to initiate a local oxidation of the sample surface below the tip, which makes the underlying 2DEG insulating.

The particular advantage of AFM lithography over EBL with regard to graphene is, that no resist layer is needed for the pattering. Thereby, additional contamination of the graphene surface is avoided during the fabrication process. Further, the structure can be investigated by means of microscopy and in-situ measurements immediately after the patterning and possibly corrected for imperfections.

Here, we investigate the feasibility to adapt this technique to graphene. Since the 2DES is lying on the surface, a direct modification of the graphene is permitted. A well conceivable chain of chemical reactions taking place, is [135]

$$\begin{aligned} C + H_2O &\rightarrow C(H_2O), \\ C(H_2O) &\rightarrow H_2 + C(O), \\ C(O) &\rightarrow CO. \end{aligned}$$

In the first step a water molecule is physisorbed on a carbon atom to form $C(H_2O)$. Next, a hydrogen molecule is released as gas and the oxygen is chemisorbed on a carbon atom C(O). In the last step, the final reaction product carbon monoxide is obtained [135], leaving a vacancy in the graphene lattice behind.

Experiments on graphite

All experiments discussed here were carried out with a commercial AFM (Veeco Dimension V). Since a number of parameters can be tuned to reach optimal performance, first tests were performed on highly ordered pyrolytic graphite (HOPG). This stack of graphene layers is conductive and no additional grounding of the sample is necessary.

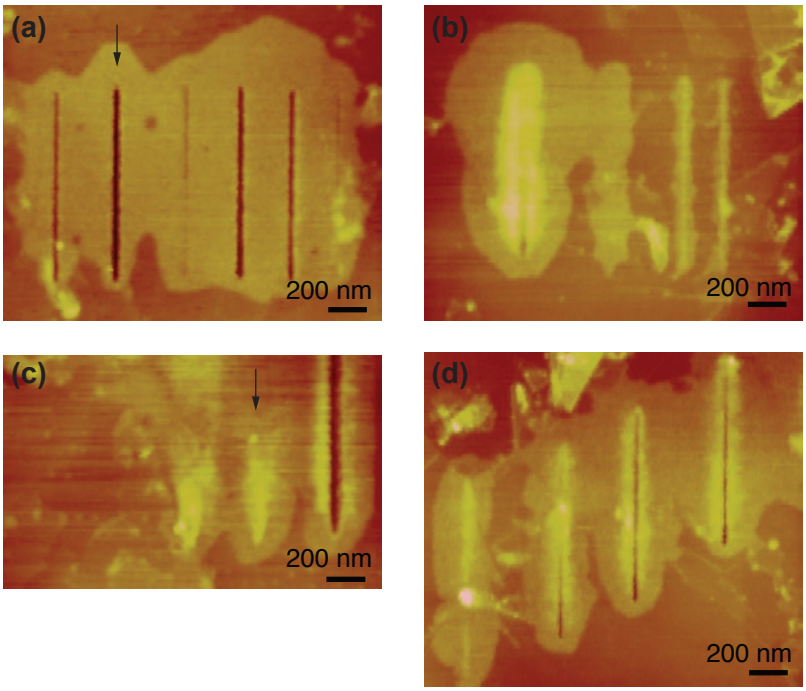

Figure D.4: Local oxidation on HOPG with tapping mode under the variation of different parameters. (a) Applied DC voltage varied (from left to right: -26 V, -28 V, -25 V, -28 V, -27 V, -25 V). The oxidation set point was 2.6% of the free driving amplitude for the three lines on the left side and 3% for the ones on the right. (b) Write rate varied (from left to right: 0.02 μm/s, 0.1 μm/s, 0.5 μm/s, 1 μm/s). (c) Oxidation set point varied (from left to right: 1.9%, 2.1%, 1.7%). (d) Relative humidity varied (from left to right: 26%, 38%, 40%,43%).

The AFM is operated in tapping mode with a free driving amplitude of $\approx$ 350 mV and the amplitude feedback is kept on during the writing process. We apply a DC voltage V_{ox} to the highly doped Si tip and lower the amplitude set point during the writing process to increase the tip surface interaction. The AFM images in Fig. D.4 illustrate the effect of the applied tip voltage, the write rate (WR), the oxidation set point (SP) and the relative humidity in the sample environment on the resulting modification.

We first look at the influence of the tip voltage with constant SP = 2.6 − 3% and WR = 100 nm/s. In Fig. D.4 (a) trenches of ≈ 50 nm width and up to 10 nm depth are etched into the graphite. A larger oxidation voltage V_{ox} is correlated with deeper trenches, meaning that the anticipated oxidation reaction is taking place more efficiently. Along with the local tip-induced modification comes a change in the topography of the graphite on a larger scale (bright cloud-shaped area around the trenches). This height increase may either be due to the lifting of the uppermost graphite layer(s) or due a partial execution of the reaction chain mentioned before, leaving C(O) behind.

Next, we vary the write rate away from the standard speed of 100 nm/s and keeping V_{ox} = -28 V and SP = 3% constant (see Fig. D.4 (b)). Although no trenches are etched for any of the lines, the area of modified material is strongly increasing as the tip is kept at a certain position for a longer time.

Figure D.4 (c) illustrates that the set point during the oxidation is a crucial parameter. The write rate was 100 nm/s and V_{ox} = -28 V. Only the lowest SP results in etching of the graphite. The difficulty of reproducibility gets apparent when comparing the second to left line in D.4 (a) and the middle one in D.4 (c) (see arrows), which are nominally written under the same conditions expect for the SP value. Even though the set point is lower for the latter line, the graphene is not removed, meaning that the chemical reaction could not be completed.

As the last variable, the relative humidity is changed, whereas it was kept at 48% for the previous graphs. The other parameters were V_{ox} = -28 V, SP = 3% and WR = 100 nm/s. Clearly, the etching is facilitated at higher relative humidities. However, bulging along the edges of the trench appears for all traces and the surrounding graphite material is affected as well.

For GaAs it has been reported [136] that the application of a square shaped AC tip voltage is beneficial. Such a scheme helps to maintain the water meniscus between the surface and the tip and neutralizes surface charges, since the tip polarization is changed in each cycle. This method was however not found to improve the results for the lithography on graphite or graphene in this study.

Experiments on graphene

In order to assure a good connection to ground, the graphene flakes were contacted, bonded and mounted into a grounded chip socket at the AFM. To remove residual resist, we scanned the flake in contact mode with a DC tip bias of -3 V before starting the lithography.

Both tapping and contact mode AFM were tested for the patterning of single layer graphene and the results were slightly better for the operation in contact mode with an applied DC bias at the tip. As demonstrated before, a higher reactivity was achieved with increased relative humidity. We therefore humidified the air to 60% for the modification process. Since the AFM tip is touching the surface at all times in contact mode operation, the set point was not changed during the lithography. Also

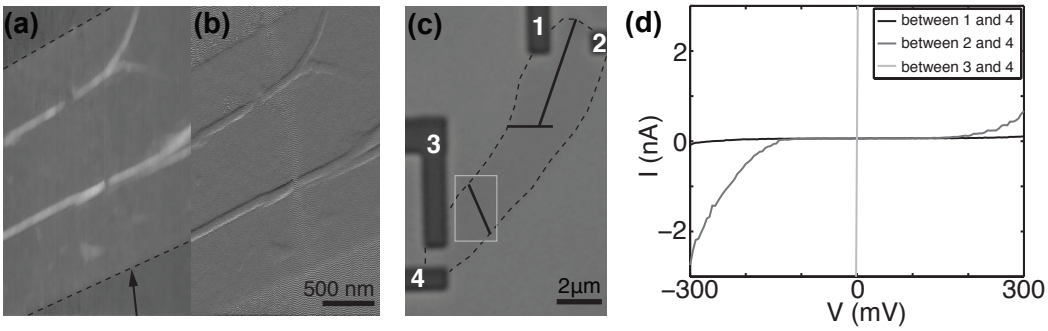

Figure D.5: (a) Height image obtained with contact mode just after writing. Arrow indicates direction of lithography trace. (b) Deflection error image corresponding to (a). (c) Optical microscope image of complete flake. Zoom shown in (a) and (b) was done in the area marked by the grey box. Contacts are numbered and the lines along which the graphene was modified are marked (black lines). (d) Current-voltage characteristics measured between different contacts (see legend). Data was recorded at $T = 4$ K and the contact resistances were all on the order of few kΩ (tested before the structuring).

due to the fact that a contact is established between the probe and the graphene, V_{ox} = -6 V is enough to initiate a chemical reaction. Care has to be taken, that the mechanical force is low enough to not cause ripping of the graphene layer when working in this operation mode.

Figure D.5 (a) and (b) show AFM micrographs taken immediately after the writing of a vertical line (indicated by the arrow) across the flake. Although a change is hardly visible in the height image, the tip experiences a fast varying change in deflection along this cut. Subsequently, another section of the flake was processed in the same way (see Fig. D.5 (c) for the position of the lithographic traces).

Since the graphene flake was connected to four electrodes, measurements of the insulating properties across the modified lines were performed in a He dewar setup at 4 K. The recorded IV-characteristics are shown in Fig. D.5 (d) measured for different contact configurations. For the contact pair located in the lower part of the flake (3 and 4), a very low resistance was measured, indicating that the graphene is conducting well. If the two contacts are separated by a lithography trace (2 and 4), the current is suppressed up to a threshold voltage of $V \approx 120$ mV. This value is increased to $V \approx 300$ mV, if a second line is located in-between the two electrodes (1 and 4).

The fact that lithographic traces are insulating for low voltage bias values combined with the observation that the graphene is not removed in the modified areas, supports the statement made earlier about the uncompleted chemical reaction. The

chemisorbed oxygen forming C(O), reduces the conductivity of graphene considerably, but does not break all bonds between neighboring carbon atoms across the flake. Hence, conductive paths remain and we observe a finite current.

Conclusions

It could be shown that AFM lithography can be used to modify both graphite and graphene. Throughout the experiments, the reproducibility was however found to be rather poor. A reason is likely the lack of control of the relative humidity on the sample surface, which is one of the crucial parameters for the reaction to take place. Further, discharges and non-local modification of the graphene happened numerous times, possibly related to charged impurities on the surface. Other groups that reported structures fabricated by local oxidation with an AFM, mentioned similar issues [137–139].

With the advent of ultra clean graphene on BN, the request for a lower impurity density on the surface is supposably met. If high relative humidities can be provided at the reaction interface, local oxidation may be an alternative to the commonly used dry etching technique.

E Processing of graphene samples in FIRST

Process	Description of process steps	Remarks
Defining markers on Si or Si/SiO_2 wafer	*Optional HMDS coating*: 2-5 droplets of HMDS on wafer, spinner parameters: 3000 rpm, acc 2, 40 s	For better adhesion of the photoresist
	Resist coating: cover 1/3 of wafer with resist ma-N 1405, spinner parameters: 3000 rpm, acc 2, 40 s	
	Baking: 60 s at 100°C	
	Exposure: MA6 mask aligner, constant power (CP) mode, lamp test with 365 nm sensor, Exposure ca. 40 s	
	Developing: ma-D 533s, 60 s, stir slightly, rinse in water for 120 s	
	Cleaning before deposition: small oxygen plasma asher, 30 s at 200 W, 0.7 Torr	Important to remove residues of photo lithography below bond pads
	Metal evaporation: 5 nm Ti/ 40-50 nm Au	
	Lift-off: > 10 min in 50°C acetone until gold starts to lift, blow Au away with pipette and use US	
	Cleaning: 2 min in acetone, US power 9; 2 min in isopropanol, US power 9, dry with N_2	
Cutting wafer into individual chips	Spinning: Shipley 1805, 60 s at 5000 rpm	Protection layer during sawing
	Baking: 2 min at 115°C	
	Contact Hansjakob Rusterholz for sawing into 7.1×7.1 mm^2 chips or 1.2×1.2 mm^2 if intended for transfer chips	
Preparing chips for transfer process	Clean samples: 2 min in acetone, US power 5; 2 min in isoprop., US power 5, dry with N_2	
	Spinning: PVA 9000 in DI water (4.7 mass %), 60 s at 4000 rpm	
	Baking: 2 min at 100°C	
	Spinning: PMMA 950K 4:1 in CB, 60 s at 4000 rpm	
	Baking: 2 min at 120°C	Compare color to Si/SiO_2 substrate to assure visibility of graphene with the optical microscope
Mechanical exfoliation of graphene or boron nitride	Clean samples: 2 min in acetone, US power 5; 2 min in isoprop., US power 5, dry with N_2	
	Plasma ashing: 2 min at 200 W, 0.7 Torr	Optional 10 min ozone cleaning in UVOCS
	Press graphite nugget or BN crystal on blue tape once, fold 6-10 times to distribute	To be done in the grey room next to wafer saw
	Put Si chips upside-down onto tape, press gently	
	Clean chips in warm acetone (short US pulse in warm acetone)	To make sure the flakes used for processing stick well
	Rinse 2 min in isoprop., no more US power, dry with N_2	
	Identify flakes with means of optical microscope, AFM and Raman spectroscopy (only for graphene)	
Transfer of graphene or boron nitride on other substrate	Mark position of flake on transfer chip with small pieces of blue tape	Facilitates positioning later
	Scratch away the resist along the edges of the transfer chip	To allow penetration of water to the PVA layer
	Fill DI water into beaker (5 mm), place chip onto water surface and dip edges and corners of transfer chip into water gently	
	Wait until PMMA film is separated from Si and floating on the water surface	
	Fill beaker with water to the rim and fish the film with the "volcano"	
	Pat dry the bottom of the volcano and heat on hot plate at 70°C until no water is left anymore	
	Place target substrate on heater in micro manipulator set to 15 V (ca. 110°C)	To remove water from the target surface
	Mount volcano to micro manipulator and align graphene flake with substrate	
	Leave after contact has been established for 5−10 min at 110°C	
	Remove chip from volcano	
	Rinse in DI water to remove PVA residues and do lift-off in warm acetone to remove PMMA (ca. 5 min)	
	Clean samples: 2 min in isoprop., no US power, dry with N_2	

Process	Description of process steps	Remarks
Fabrication of metal contacts or gate electrodes	Spinning: PMMA 50K in CB, 1000 rpm for 1 s, 5000 rpm for 45 s	
	Baking: 3 min at 180°C	
	Spinning: PMMA 950K 1:1, 1000 rpm for 1 s, 5000 rpm for 45 s	
	Bake: 3 min at 180°C	
	EBL exposure	
	Developing: MIBK:IPA 1:3, 60 s, no stirring	
	Rinsing: isopropanol, 60 s, dry with N_2	
	Metal evaporation: 0.5 nm Cr, 40 nm Au	Evaporate 5 nm Ti with closed shutter before to achieve lower pressure in chamber
	Lift-off: ≈5-10 min in acetone at 50°C, stir or blow with pipette to remove gold	
	Clean samples: 2 min in isoprop., no US power, dry with N_2	
Dry etching	Spinning (for normal size structures): PMMA 50K in CB, 1000 rpm for 1 s, 5000 rpm for 45 s	
	Spinning (for small structures): PMMA 950K 2:5, 1000 rpm for 1 s, 6000 rpm for 45 s	For single-pixel lines, resist thickness: ≈ 45 nm
	Baking: 3 min at 180°C	
	EBL exposure	
	Developing: MIBK:IPA 1:3, 60 s, no stirring	
	Rinsing: isopropanol, 60 s, dry with N_2	
	Etching in RIE (for normal size structures): clean chamber (recipe Graphene O2 clean), load sample, etch (recipe Graphene C-etch gentle (13−40s)	Depending on thickness of flakes that should be etched
	Etching in RIE (for thin resist): clean chamber (recipe Graphene O2 clean), load sample, etch (recipe Graphene C-etch gentle (10-15s))	
	Remove resist: prepare two glasses of acetone at 50°C, hold sample upside-down, immerse in first glass of acetone while moving slightly for ≈ 5s, immerse into second glass of acetone for 2 min, rinse in isopropanol for 2 min, dry with N_2	Sometimes the upper resist layer is deposits on top of the sample, then it can only be removed in oxygen plasma
Glueing sample into chip carrier	Prepare conductive silver paste: H20E A,B, approx 30g of each on a glass plate, mix with toothpick	
	Optional: use dummy chip as spacer	Samples for scanning gate or AM lithography
	Glue sample to chip carrier, contact back gate by droplet of glue from the side	
	Baking: in vacuum in graphene annealing oven, 20 min at 150 °C	
Processing top gates with Cytop^{TM} dielectric	Spinning: Cytop^{TM} CTL-809M diluted 1:10 in CT-Solv.180, 500 rpm for 10 s, 2000 rpm for 20 s	
	Baking (I): 30 min at 50°C; Baking (II): 30 min at 80°C	
	Metal evaporation: 5 nm Cr	PMMA does not stick on the hydrophobic Cytop^{TM} surface
	Process contacts as described above	
	Cr-etching: Cr-etch (ammonium nitrate & acidic acid & water), 30s	
	Rinsing: 2 min in DI water	

Publications

Transport through graphene double dots
F. Molitor, S. Dröscher, J. Güttinger, A. Jacobsen, C. Stampfer, T. Ihn, and K. Ensslin
Appl. Phys. Lett. **94**, 222107 (2009)

Graphene single-electron transistors
T. Ihn, J. Güttinger, F. Molitor, S. Schnez, E. Schurtenberger, A. Jacobsen, S. Hellmüller, T. Frey, S. Dröscher, C. Stampfer, and K. Ensslin
Materials Today **13**, 44 (2010)

Observation of excited states in a graphene double quantum dot
F. Molitor, H. Knowles, S. Dröscher, U. Gasser, T. Choi, P. Roulleau, J. Güttinger, A. Jacobsen, C. Stampfer, K. Ensslin and T. Ihn
Europhys. Lett. **89**, 67005 (2010)

Quantum capacitance and density of states of graphene
S. Dröscher, P. Roulleau, F. Molitor, P. Studerus, C. Stampfer, K. Ensslin, and T. Ihn
Appl. Phys. Lett. **96**, 152104 (2010)

Highly tunable hybrid quantum dots with charge detection
C. Rössler, B. Küng, S. Dröscher, T. Choi, T. Ihn, K. Ensslin, and M. Beck
Appl. Phys. Lett. **97**, 152109 (2010)

Coherent electron-phonon coupling in tailored quantum systems
P. Roulleau, S. Baer, T. Choi, F. Molitor, J. Güttinger, T. Müller, S. Dröscher, K. Ensslin, and T. Ihn
Nature Com. **2**, 239 (2011)

Raman spectroscopy on etched graphene nanoribbons
D. Bischoff, J. Güttinger, S. Dröscher, T. Ihn, K. Ensslin, and C. Stampfer
J. Appl. Phys. **109**, 073710 (2011)

Electronic properties of graphene nanostructures
F. Molitor, J. Güttinger, C. Stampfer, S. Dröscher, A. Jacobsen, T. Ihn and K. Ensslin
Topical Review, J. Phys. C **23**, 243201 (2011)

Coulomb gap in graphene nanoribbons
S. Dröscher, H. Knowles, Y. Meir, K. Ensslin, and T. Ihn
Phys. Rev. B **84**, 073405 (2011)

Transport in Graphene Nanostructures
C. Stampfer, S. Fringes, J. Güttinger, F. Molitor, C. Volk, B. Terrés, J. Dauber, S. Engels, S. Schnez, A. Jacobsen, S. Dröscher, T. Ihn, K. Ensslin
Frontiers of Physics **6**, 271 (2011)

Quantum capacitance and density of states of graphene
S. Dröscher, P. Roulleau, F. Molitor, P. Studerus, C. Stampfer, K. Ensslin, and T. Ihn
Phys. Scr. T **146**, 014069 (2012)

Electronic transport in graphene nanostructures on SiO_2
T. Ihn, S. Dröscher, S. Schnez, H. Knowles, J. Güttinger, M. Hüfner, C. Stampfer, Y. Meir, and K. Ensslin
Solid St. Comm. **online** (2012)

Graphene constrictions
S. Dröscher, F. Molitor, T. Ihn, and K. Ensslin
to be published in book "Physics of Graphene"

High-frequency gate manipulation of a bilayer graphene quantum dot
S. Dröscher, J. Güttinger, T. Mathis, B. Batlogg, T. Ihn, and K. Ensslin
in preparation

Electrostatic confinement in double gated bilayer graphene
S. Dröscher, C. Barraud, T. Ihn, and K. Ensslin
in preparation

Bibliography

[1] H. P. Boehm, R. Setton, and E. Stumpp, Carbon **24**, 241 (1986).

[2] A. K. Geim, Physica Scripta **2012**, 014003 (2012).

[3] H. P. Boehm, A. Clauss, G. O. Fischer, and U. Hofmann, Zeitschrift für anorganische und allgemeine Chemie **316**, 119 (1962).

[4] P. R. Wallace, Physical Review **71**, 622 (1947).

[5] K. S. Novoselov, A. K. Geim, S. V. Morozov, D. Jiang, Y. Zhang, S. V. Dubonos, I. V. Grigorieva, and A. A. Firsov, Science **306**, 666 (2004).

[6] C. Lee, X. Wei, J. W. Kysar, and J. Hone, Science **321**, 385 (2008).

[7] X. Wang, Y. Ouyang, X. Li, H. Wang, J. Guo, and H. Dai, Physical Review Letters **100**, 206803 (2008).

[8] T. Ihn, J. Güttinger, F. Molitor, S. Schnez, E. Schurtenberger, A. Jacobsen, S. Hellmüller, T. Frey, S. Dröscher, C. Stampfer, et al., Materials Today **13**, 44 (2010).

[9] T. Ando, A. B. Fowler, and F. Stern, Reviews of Modern Physics **54**, 437 (1982).

[10] K. S. Novoselov, E. McCann, S. V. Morozov, V. I. Fal'ko, M. I. Katsnelson, U. Zeitler, D. Jiang, F. Schedin, and A. K. Geim, Nature Physics **2**, 177 (2006).

[11] J. Güttinger, C. Stampfer, S. Hellmuller, F. Molitor, T. Ihn, and K. Ensslin, Applied Physics Letters **93**, 212102 (2008).

[12] F. Molitor, S. Dröscher, J. Güttinger, A. Jacobsen, C. Stampfer, T. Ihn, and K. Ensslin, Applied Physics Letters **94**, 222107 (2009).

[13] M. Hüfner, F. Molitor, A. Jacobsen, A. Pioda, C. Stampfer, K. Ensslin, and T. Ihn, Physica Status Solidi B **246**, 2756 (2009).

[14] M. T. Allen, J. Martin, and A. Yacoby, arXiv:1202.0820v1 (2012).

[15] E. McCann, D. S. Abergel, and V. I. Fal'ko, The European Physical Journal - Special Topics **148**, 91 (2007).

[16] A. H. C. Neto, F. Guinea, N. M. R. Peres, K. S. Novoselov, and A. K. Geim, Reviews of Modern Physics **81**, 109 (2009).

[17] A. F. Young and P. Kim, Nature Physics **5**, 222 (2009).

[18] J.-H. Chen, C. Jang, S. Xiao, M. Ishigami, and M. S. Fuhrer, Nature Nanotechnology **3**, 206 (2008).

[19] K. Yoshizawa, T. Kato, and T. Yamabe, The Journal of Chemical Physics **105**, 2099 (1996).

[20] F. Guinea, A. H. Castro Neto, and N. M. R. Peres, Physical Review B **73**, 245426 (2006).

[21] E. McCann, Physical Review B **74**, 161403 (2006).

[22] E. McCann and V. I. Fal'ko, Physical Review Letters **96**, 086805 (2006).

[23] M. S. Dresselhaus and G. Dresselhaus, Advances in Physics **51**, 1 (2002).

[24] A. Matulis and F. M. Peeters, Physical Review B **77**, 115423 (2008).

[25] K. v. Klitzing, G. Dorda, and M. Pepper, Physical Review Letters **45**, 494 (1980).

[26] F. D. M. Haldane, Physical Review Letters **61**, 2015 (1988).

[27] E. V. Castro, K. S. Novoselov, S. V. Morozov, N. M. R. Peres, J. M. B. L. dos Santos, J. Nilsson, F. Guinea, A. K. Geim, and A. H. C. Neto, Physical Review Letters **99**, 216802 (2007).

[28] P. Blake, E. W. Hill, A. H. C. Neto, K. S. Novoselov, D. Jiang, R. Yang, T. J. Booth, and A. K. Geim, Applied Physics Letters **91**, 063124 (2007).

[29] A. C. Ferrari, J. C. Meyer, V. Scardaci, C. Casiraghi, M. Lazzeri, F. Mauri, S. Piscanec, D. Jiang, K. S. Novoselov, S. Roth, et al., Physical Review Letters **97**, 187401 (2006).

[30] D. Graf, F. Molitor, T. Ihn, and K. Ensslin, Physical Review B **75**, 245429 (2007).

[31] C. R. Dean, A. F. Young, I. Meric, C. Lee, L. Wang, S. Sorgenfrei, K. Watanabe, T. Taniguchi, P. Kim, K. L. Shepard, et al., Nature Nanotechnology **5**, 722 (2010).

[32] A. K. Geim and K. S. Novoselov, Nature Materials **6**, 183 (2007).

[33] J. H. Bardarson, J. Tworzydło, P. W. Brouwer, and C. W. J. Beenakker, Physical Review Letters **99**, 106801 (2007).

[34] V. V. Cheianov, V. I. Fal'ko, B. L. Altshuler, and I. L. Aleiner, Physical Review Letters **99**, 176801 (2007).

[35] E. H. Hwang, S. Adam, and S. Das Sarma, Physical Review Letters **98**, 186806 (2007).

[36] P. M. Ostrovsky, I. V. Gornyi, and A. D. Mirlin, Physical Review B **74**, 235443 (2006).

[37] M. I. Katsnelson, The European Physical Journal B - Condensed Matter and Complex Systems **51**, 157 (2006).

[38] K. I. Bolotin, K. J. Sikes, J. Hone, H. L. Stormer, and P. Kim, Physical Review Letters **101**, 096802 (2008).

[39] X. Du, I. Skachko, A. Barker, and E. Y. Andrei, Nat Nano **3**, 491 (2008).

[40] Y. W. Tan, Y. Zhang, K. Bolotin, Y. Zhao, S. Adam, E. H. Hwang, S. Das Sarma, H. L. Stormer, and P. Kim, Physical Review Letters **99**, 246803 (2007).

[41] J. Martin, N. Akerman, G. Ulbricht, T. Lohmann, J. H. Smet, K. von Klitzing, and A. Yacoby, Nature Physics **4**, 144 (2008).

[42] J. B. Oostinga, H. B. Heersche, X. Liu, A. F. Morpurgo, and L. M. K. Vandersypen, Nat Mater **7**, 151 (2008).

[43] S. Russo, M. F. Craciun, M. Yamamoto, S. Tarucha, and A. F. Morpurgo, New Journal of Physics **11**, 095018 (2009).

[44] A. F. Young, C. R. Dean, I. Meric, S. Sorgenfrei, H. Ren, K. Watanabe, T. Taniguchi, J. Hone, K. L. Shepard, and P. Kim, arXiv:1004.5556v2 (2010).

[45] E. M. Hamilton, Philosophical Magazine **26**, 1043 (1972).

[46] N. F. Mott, *Conduction in Non-Crystalline Materials* (Oxford University Press, New York, 1987).

[47] T. P. Smith, B. B. Goldberg, P. J. Stiles, and M. Heiblum, Physical Review B **32**, 2696 (1985).

[48] F. Stern, Applied Physics Letters **43**, 974 (1983).

[49] S. Ilani, L. A. K. Donev, M. Kindermann, and P. L. McEuen, Nat Phys **2**, 687 (2006).

[50] K. S. Novoselov, A. K. Geim, S. V. Morozov, D. Jiang, M. I. Katsnelson, I. V. Grigorieva, S. V. Dubonos, and A. A. Firsov, Nature **438**, 197 (2005).

[51] T. Fang, A. Konar, H. Xing, and D. Jena, Applied Physics Letters **91**, 092109 (2007).

[52] A. A. Shylau, J. W. Klstrokos, and I. V. Zozoulenko, Physical Review B **80**, 205402 (2009).

[53] J. Xia, F. Chen, J. Li, and N. Tao, Nat Nano **4**, 505 (2009).

[54] S. Dröscher, P. Roulleau, F. Molitor, P. Studerus, C. Stampfer, K. Ensslin, and T. Ihn, Applied Physics Letters **96**, 152104 (2010).

[55] S. Luryi, Applied Physics Letters **52**, 501 (1988).

[56] J. H. Davies, *The physics of low dimensional semiconductors* (Cambridge University Press, 1998).

[57] T. Ihn, *Semiconductor Nanostructures* (Oxford university press, 2010).

[58] C. Stampfer, J. Güttinger, S. Hellmüller, F. Molitor, K. Ensslin, and T. Ihn, Physical Review Letters **102**, 056403 (2009).

[59] F. Molitor, A. Jacobsen, C. Stampfer, J. Güttinger, T. Ihn, and K. Ensslin, Physical Review B **79**, 075426 (2009).

[60] K. Todd, H.-T. Chou, S. Amasha, and D. Goldhaber-Gordon, Nano Letters **9**, 416 (2009).

[61] X. Liu, J. B. Oostinga, A. F. Morpurgo, and L. M. K. Vandersypen, Physical Review B **80**, 121407(R) (2009).

[62] M. Y. Han, J. C. Brant, and P. Kim, Physical Review Letters **104**, 056801 (2010).

[63] J. Xue, J. Sanchez-Yamagishi, D. Bulmash, P. Jacquod, A. Deshpande, K. Watanabe, T. Taniguchi, P. Jarillo-Herrero, and B. J. LeRoy, Nat Mater **10**, 282 (2011).

[64] L. A. Ponomarenko, R. Yang, R. V. Gorbachev, P. Blake, A. S. Mayorov, K. S. Novoselov, M. I. Katsnelson, and A. K. Geim, Physical Review Letters **105** (2010).

[65] E. A. Henriksen and J. P. Eisenstein, Physical Review B **82** (2010).

[66] K. Nakada, M. Fujita, G. Dresselhaus, and M. S. Dresselhaus, Physical Review B **54**, 17954 (1996).

[67] N. M. R. Peres, A. H. Castro Neto, and F. Guinea, Physical Review B **73**, 195411 (2006).

[68] D. Gunlycke, D. A. Areshkin, and C. T. White, Applied Physics Letters **90**, 142104 (2007).

[69] M. Zarea and N. Sandler, Physical Review Letters **99**, 256804 (2007).

[70] M. Y. Han, B. Ozyilmaz, Y. Zhang, and P. Kim, Physical Review Letters **98**, 206805 (2007).

[71] Z. Chen, Y.-M. Lin, M. J. Rooks, and P. Avouris, Physica E **40**, 228 (2007).

[72] P. Gallagher, K. Todd, and D. Goldhaber-Gordon, Physical Review B **81**, 115409 (2010).

[73] J. B. Oostinga, B. Sacepe, M. F. Craciun, and A. F. Morpurgo, Physical Review B **81**, 193408 (2010).

[74] B. Terres, J. Dauber, C. Volk, S. Trellenkamp, U. Wichmann, and C. Stampfer, Applied Physics Letters **98**, 032109 (2011).

[75] N. Tombros, A. Veligura, J. Junesch, M. H. D. Guimaraes, I. J. Vera-Marun, H. T. Jonkman, and B. J. van Wees, Nat Phys **advance online publication**, (2011).

[76] D. A. Areshkin, D. Gunlycke, and C. T. White, Nano Letters **7**, 204 (2006).

[77] F. Sols, F. Guinea, and A. H. C. Neto, Physical Review Letters **99**, 166803 (2007).

[78] D. Querlioz, Y. Apertet, A. Valentin, K. Huet, A. Bournel, S. Galdin-Retailleau, and P. Dollfus, Applied Physics Letters **92**, 042108 (2008).

[79] A. Lherbier, B. Biel, Y.-M. Niquet, and S. Roche, Physical Review Letters **100**, 036803 (2008).

[80] S. Adam, S. Cho, M. S. Fuhrer, and S. D. Sarma, Physical Review Letters **101**, 046404 (2008).

[81] M. Evaldsson, I. V. Zozoulenko, H. Xu, and T. Heinzel, Physical Review B **78**, 161407 (2008).

[82] E. R. Mucciolo, A. H. C. Neto, and C. H. Lewenkopf, Physical Review B **79**, 075407 (2009).

[83] G. Schubert, J. Schleede, and H. Fehske, Physical Review B **79**, 235116 (2009).

[84] I. Martin and Y. M. Blanter, Physical Review B **79**, 235132 (2009).

[85] S. Ihnatsenka and G. Kirczenow, Physical Review B **80**, 201407 (2009).

[86] J. W. Klos, A. A. Shylau, I. V. Zozoulenko, H. Xu, and T. Heinzel, Physical Review B **80**, 245432 (2009).

[87] F. Libisch, S. Rotter, and J. Burgdörfer, arXiv:1102.3848v1 (2011).

[88] B. J. van Wees, H. van Houten, C. W. J. Beenakker, J. G. Williamson, L. P. Kouwenhoven, D. van der Marel, and C. T. Foxon, Physical Review Letters **60**, 848 (1988).

[89] D. A. Wharam, T. J. Thornton, R. Newbury, M. Pepper, H. Ahmed, J. E. F. Frost, D. G. Hasko, D. C. Peacock, D. A. Ritchie, and G. A. C. Jones, Journal of Physics C: Solid State Physics **21**, 209 (1988).

[90] H. van Houten and C. Beenakker, Physics Today **49**, 22 (1996).

[91] M. Fujita, K. Wakabayashi, K. Nakada, and K. Kusakabe, Journal of the Physical Society of Japan **65**, 1920 (1996).

[92] K. Wakabayashi, Physical Review B **64**, 125428 (2001).

[93] C. T. White, J. Li, D. Gunlycke, and J. W. Mintmire, Nano Letters **7**, 825 (2007).

[94] L. Brey and H. A. Fertig, Physical Review B **73**, 235411 (2006).

[95] F. Muñoz Rojas, D. Jacob, J. Fernández-Rossier, and J. J. Palacios, Physical Review B **74**, 195417 (2006).

[96] Y.-W. Son, M. L. Cohen, and S. G. Louie, Physical Review Letters **97**, 216803 (2006).

[97] D. Graf, F. Molitor, K. Ensslin, C. Stampfer, A. Jungen, C. Hierold, and L. Wirtz, Nano Letters **7**, 238 (2007).

[98] D. J. Thouless, Physics Reports **13**, 93 (1974).

[99] A. B. Fowler, A. Hartstein, and R. A. Webb, Physical Review Letters **48**, 196 (1982).

[100] M. Kemerink and L. W. Molenkamp, Applied Physics Letters **65**, 1012 (1994).

[101] J. Bai, R. Cheng, F. Xiu, L. Liao, M. Wang, A. Shailos, K. L. Wang, Y. Huang, and X. Duan, Nat Nano **5**, 655 (2010).

[102] S. Dröscher, H. Knowles, Y. Meir, K. Ensslin, and T. Ihn, Physical Review B **84**, 73405 (2011).

[103] F. Molitor, C. Stampfer, J. Güttinger, A. Jacobsen, T. Ihn, and K. Ensslin, Semiconductor Science and Technology **25**, 034002 (2010).

[104] E. V. Castro, N. M. R. Peres, J. M. B. Lopes dos Santos, A. H. C. Neto, and F. Guinea, Physical Review Letters **100**, 026802 (2008).

[105] C. Stampfer, E. Schurtenberger, F. Molitor, J. Güttinger, T. Ihn, and K. Ensslin, Nano Letters **8**, 2378 (2008).

[106] S. Schnez, F. Molitor, C. Stampfer, J. Güttinger, I. Shorubalko, T. Ihn, and K. Ensslin, Applied Physics Letters **94**, 012107 (2009).

[107] J. Güttinger, C. Stampfer, F. Libisch, T. Frey, J. Burgdörfer, T. Ihn, and K. Ensslin, Physical Review Letters **103**, 046810 (2009).

[108] S. Schnez, J. Güttinger, M. Hüfner, C. Stampfer, K. Ensslin, and T. Ihn, Physical Review B **82**, 165445 (2010).

[109] Y. Meir, N. S. Wingreen, and P. A. Lee, Physical Review Letters **66**, 3048 (1991).

[110] D. V. Averin and Y. V. Nazarov, Physical Review Letters **65**, 2446 (1990).

[111] Y. C. Huang, C. P. Chang, and M. F. Lin, Nanotechnology **18**, 495401 (2007).

[112] J. Liu, A. R. Wright, C. Zhang, and Z. Ma, Applied Physics Letters **93**, 041106 (2008).

[113] C. Ritter, S. S. Makler, and A. Latgé, Physical Review B **77**, 195443 (2008).

[114] B. I. Shklovskii and A. L. Efros, *Electronic properties of doped semiconductors* (Springer, Heidelberg, Germany, 1984).

[115] M. E. Gershenson, Y. B. Khavin, A. G. Mikhalchuk, H. M. Bozler, and A. L. Bogdanov, Physical Review Letters **79**, 725 (1997).

[116] J. Cai, P. Ruffieux, R. Jaafar, M. Bieri, T. Braun, S. Blankenburg, M. Muoth, A. P. Seitsonen, M. Saleh, X. Feng, et al., Nature **466**, 470 (2010).

[117] J. Güttinger, J. Seif, C. Stampfer, A. Capelli, K. Ensslin, and T. Ihn, Physical Review B **83**, 165445 (2011).

[118] J. Güttinger, T. Frey, C. Stampfer, T. Ihn, and K. Ensslin, Physical Review Letters **105**, 116801 (2010).

[119] F. Libisch, S. Rotter, J. Güttinger, C. Stampfer, and J. Burgdörfer, Physical Review B **81**, 245411 (2010).

[120] W. L. Kalb, T. Mathis, S. Haas, A. F. Stassen, and B. Batlogg, Applied Physics Letters **90**, 092104 (2007).

[121] M. P. Walser, W. L. Kalb, T. Mathis, T. J. Brenner, and B. Batlogg, Applied Physics Letters **94**, 053303 (2009).

[122] T. Fujisawa, Y. Tokura, and Y. Hirayama, Physical Review B **63**, 081304 (2001).

[123] A. Pfund, Ph.D. thesis, ETH Zurich (2008).

[124] K. Zou, X. Hong, and J. Zhu, Physical Review B **84**, 085408 (2011).

[125] G. Giovannetti, P. A. Khomyakov, G. Brocks, P. J. Kelly, and J. van den Brink, Physical Review B **76**, 073103 (2007).

[126] S. Kim, J. Nah, I. Jo, D. Shahrjerdi, L. Colombo, Z. Yao, E. Tutuc, and S. K. Banerjee, Applied Physics Letters **94**, 062107 (2009).

[127] C. W. J. Beenakker and H. van Houten, *Quantum transport in semiconductor nanostructures*, vol. 44 of *Solid State Physics* (Academic Press, Inc., 1991).

[128] P. A. Lee and T. V. Ramakrishnan, Reviews of Modern Physics **57**, 287 (1985).

[129] P. A. Lee, A. D. Stone, and H. Fukuyama, Physical Review B **35**, 1039 (1987).

[130] S. Nakaharai, J. R. Williams, and C. M. Marcus, Physical Review Letters **107**, 036602 (2011).

[131] Y. Zhang, Y.-W. Tan, H. L. Stormer, and P. Kim, Nature **438**, 201 (2005).

[132] L. A. Ponomarenko, F. Schedin, M. I. Katsnelson, R. Yang, E. W. Hill, K. S. Novoselov, and A. K. Geim, Science **320**, 356 (2008).

[133] S. Moriyama, D. Tsuya, E. Watanabe, S. Uji, M. Shimizu, T. Mori, T. Yamaguchi, and K. Ishibashi, Nano Letters **9**, 2891 (2009).

[134] X. Du, I. Skachko, F. Duerr, A. Luican, and E. Y. Andrei, Nature **462**, 192 (2009).

[135] H. Hiura, Applied Surface Science **222**, 374 (2004).

[136] D. Graf, M. Frommenwiler, P. Studerus, T. Ihn, K. Ensslin, D. C. Driscoll, and A. C. Gossard, Journal of Applied Physics **99**, 053707 (2006).

[137] A. J. M. Giesbers, U. Zeitler, S. Neubeck, F. Freitag, K. S. Novoselov, and J. C. Maan, Solid State Communications **147**, 366 (2008).

[138] S. Masubuchi, M. Ono, K. Yoshida, K. Hirakawa, and T. Machida, Applied Physics Letters **94**, 082107 (2009).

[139] L. Weng, L. Zhang, Y. P. Chen, and L. P. Rokhinson, Applied Physics Letters **93**, 093107 (2008).

Acknowledgements

Completing a PhD is clearly not only the achievement of a single person, but the result of numerous people contributing to it in different ways.
In Klaus Ensslin I found an adviser who trusts in his students and provides support whenever it is needed. During the last years I benefited a lot from your encouraging enthusiasm, discussions about physics and other interesting topics and the good atmosphere you create in the group. Thank you for giving me the opportunity to work in such an environment!
Thomas Ihn always had an open door and time did not seem to matter when we pored over measurements. Oftentimes, you saw a little bit more in the data than I did and each time I left your office I had learned something new. I appreciate your excellent teaching skills and your patience.
I also want to thank Adrian Bachtold for agreeing to co-examine this thesis and coming to Zurich.
Whenever there was an issue with the lab equipment Paul Studerus and Cecil Barengo had a solution to it. With your expertise you made certain measurements possible in the first place and your help was invaluable. Even if liquid He was short sometimes, Isabelle Altorfer would always find some spare liters to keep the fridge running. In Claudia Vinzens' office I felt warmly welcomed anytime and she was a great support in the administration. Thank you all for your efforts!
On the fabrication side, the FIRST staff deserves a big thanks for keeping the lab running so smoothly and providing ideas for process development. Here, I would also like to thank the other FIRST users for being helpful and making the time in the clean room oftentimes really pleasant.
When I arrived in the group, I was introduced to the secrets of graphene processing and measuring by the already experienced members of the graphene team, for which I am most grateful to Françoise Molitor, Johannes Güttinger and Christoph Stampfer. Later, Arnhild Jacobsen, Dominik Bischoff, Clément Barraud, Pauline Simonet and Anastasia Varlet joined the team and I am convinced that you will keep the spirit and discover ever new things. Bruno Schuler, Martin Paesold, Helena Knowles and Tobias Krähenmann supported me as talented students and I appreciated their work very much.
For immediate advice in the lab I could always rely on Theo Choi, Sarah Hellmüller, Yashar Komijani, Bruno Küng, Thomas Müller, Stephan Schnez and the rest of the Nanophysics group. This atmosphere of supporting each other was truly motivating.

Besides doing physics, I enjoyed the many activities with colleagues and friends from paragliding to cruises. With Tobias Frey I ran countless laps in the forrest talking about everything under the sun. I really liked our Tuesday morning runs! Also, the climbing sessions with the Spacemonkeys helped to clear my head - and instead fill it with plans for weekend trips and other. The many discussions and events with the members of [project 21] made me realize that there is more than physics. At home, I shared ups and downs with my flat mate Dora Pinotsi. I am grateful to all of you for helping me keep the balance between work and personal life.
Representative for all people that I cannot mention here, I would like to name Sabine Ott, who contributed to this thesis by providing the honeycombs shown on the front cover.
Finally, I want to thank the people that lived through these last years with me most intensely, distracted me when I needed it and helped me recover my optimism - my family and Andrés. Danke euch für alles!